

Application of renewable fuels in ternary blends for the reduction of emissions in diesel engines



Adriaan Smuts van Niekerk

Faculty of Environment and Technology
University of the West of England

A thesis submitted in partial fulfilment of the requirements of the
University of the West of England, Bristol for the degree of
Doctor of Philosophy

March 2020

Abstract

The increasing use of biofuels to replace fossil fuels as well as more stringent emission regulations for internal combustion engines cause a challenge for the engine manufacturers to design engines that can cope with a wide range of fuels, but still offer low exhaust emissions.

In this work a compression ignition engine test bed has been used to measure emissions when using ternary fuel blends between diesel, biodiesel and ethanol as well as implementing Low Temperature Combustion (LTC) techniques. A high fidelity simulation of the engine was also created to enable studies incorporating transient drive cycles to predict engine emissions.

The aim of this project was to determine a fuel blend that achieves a 10% renewable content as well as reduce legislated engine emissions. LTC was also used to further reduce the engine emissions running on the ternary fuel blend. A mixture design of experiment (DoE) was used to optimise toward a fuel blend containing 2% biodiesel and 9% ethanol which results in a reduction of 34% in CO emissions, 10% in NO_x emissions and 21% in CO₂ emissions compared to running the engine on pump diesel fuel.

The optimisation of a Central Composite DoE showed that NO_x emissions can decrease a further 25% when the maximum exhaust gas recirculation is set to 45%, the main injection is retarded by 2 CADs, the pilot injection dwell time is set to 21 CADs and 20% of the fuel is delivered through the pilot injection. CO emissions increase as a result of the increase in EGR percentage.

Opsomming

Die toenemende gebruik van biobrandstowwe om fossielbrandstowwe te vervang, sowel as strenger wetgewing vir die beperking van skadelike voertuiguitlaatgasse, veroorsaak dat vervaardigers enjins moet ontwerp wat 'n wye reeks brandstowwe kan verbrand asook lae konsentrasies skadelike uitlaatgasse vrystel.

Hierdie navorsing bestudeer die uitlaatgasse wat geproduseer word wanneer brandstof in 'n dieselenjin gebruik word wat betsaan uit 'n mengsel van diesel, biodiesel en etanol, sowel as die effek van lae-temperatuur verbrandingstegnieke. Deur gebruik te maak van 'n akkurate simulاسie van die enjin, word die effek van enjinspoed en drywing op die uitlaatgasse van die enjin ondersoek.

Die doel van hierdie navoring was om die samestelling van 'n brandstofmengsel te bepaal wat minstens 10% hernubare inhoud bevat en wat die vrystelling van skadelike uitlaatgasse minimeer. Lae-temperatuur verbrandingstegnieke is ook gebruik om die skadelike uitlaatgasse van die enjin verder te verminder wanneer die enjin aangedryf word deur die 3-komponent brandstofmengsel. Statistiese metodes is gebruik om die samestelling van 'n ge-optimeerde brandstofmengsel te bepaal wat 2% biodiesel en 9% etanol bevat het. Die mengsel het gelei tot 'n vermindering van 34% in CO, 'n 10% afname in NO_x asook 'n vermindering van 21% in CO₂ in die uitlaatgasse teenoor 'n enjin wat net diesel gebruik het.

Die gebruik van lae-temperatuur verbrandingstegnieke het gelei tot 'n verdere vermindering van 25% in NO_x uitlaatgasse wanneer 45% van die uitlaatgasstroom teruggevoer word na die enjin se inlaat, die hoof brandstofinspuiting vertraag word met 2° en die hulp brandstofinspuiting vertraag word met 21° relatief tot die hoof brandstofinspuiting. Verder word 20% van die totale brandstof tydens die hulp brandstofinspuiting in die enjin toegedien. Die konsentrasie CO in die uitlaatgasse neem toe as gevolg van die toename in die persentasie van uitlaatgasse wat hersirkuleer word.

List of publications

- A. S. Van Niekerk, P. J. Kay, B. Drew, and N. Larsen. Development of multi-fidelity powertrain simulation for future legislation. In: *Internal Combustion Engines 2017*, Birmingham, UK, 6-7 December 2017. Available from: <http://eprints.uwe.ac.uk/33589>. (2017).
- A. S. van Niekerk, B. Drew, N. Larsen, and P. J. Kay. Influence of blends of diesel and renewable fuels on compression ignition engine emissions over transient engine conditions. *Applied Energy*. 255 (2019). DOI: 10.1016/j.apenergy.2019.113890.
- A. S. van Niekerk, B. Drew, N. Larsen, and P. J. Kay. Optimisation of Low Temperature Combustion Technology, for Future Drive Cycles, using a Factorial Design of Experiments. *SAE International Journal of Engines*. (2019-01-2171) (2019).
- A. S. van Niekerk, B. Drew, N. Larsen, and P. J. Kay. Data set for influence of blends of diesel and renewable fuels on compression ignition engine emissions. *Data in Brief*. 28 (2019), p. 104836. DOI: 10.1016/j.dib.2019.104836.
- A. S. Van Niekerk and P. J. Kay. A holistic evaluation of the impact of UK renewable strategy on emissions from compression ignition engines. *Fuel* (2019). Revised manuscript submitted.

*Gimel. Die werke van die HERE is groot; Dalet. Nagespeur word hulle deur almal
wat daar 'n welbehae in het.*

Psalm 111:2

Declaration

I hereby declare that except where specific reference is made to the work of others, the contents of this dissertation are original and have not been submitted in whole or in part for consideration for any other degree or qualification in this, or any other university. This dissertation is my own work and contains nothing which is the outcome of work done in collaboration with others, except as specified in the text and Acknowledgements. This dissertation contains fewer than 40,000 words excluding appendices.

Adriaan Smuts van Niekerk

March 2020

Acknowledgements

First of all I would like to thank my supervisory team for their continuous support during this project. Thank you Dr Peter Kay, Mr Neil Larsen and Dr Ben Drew for your supervision over the years.

I would also like to thank Dr Narges Dailami for helping with the statistical models and always being available when I have questions.

I am also grateful for the help of Mr Geoff Rowley, Mr Andrew McGauley and Mr Douglas Nash for their support in any engine test cell related issues.

Thank you to Sharon Turner from Kistler for generously providing a charge amplifier free of charge and also helping with identifying faults on the university's existing equipment.

Further, I want to say thank you to the Engineering Modelling and Simulation Group (EMSG) as well as UWE for investing money into this project and enabling me to carry out this research and supporting me financially over these years.

Last, but certainly not least, I am very grateful to all my friends and family, who supported me over the years. I want to express my gratitude to my wife for her continuous encouragement and support over the last few years as well as my daughter who I can always count on to make me smile!

Table of contents

List of figures	xix
List of tables	xxiii
Nomenclature	xxv
1 Introduction	1
1.1 Opening statements	1
1.2 Biofuels and future legislation: A review	2
1.2.1 Combating climate change	2
1.2.2 The European Union and climate change	4
1.2.3 Tackling air pollution in the UK	6
1.2.4 Biofuel as an alternative fuel	7
1.2.4.1 First generation biofuel	7
1.2.4.2 Second generation biofuel	8
1.2.4.3 Third generation biofuel	9
1.2.5 Biofuel in the transport industry	10
1.2.6 Low Temperature Combustion	15
1.2.6.1 Low Temperature Combustion	15
1.2.6.2 Using biofuel with LTC	18
1.2.7 Modelling engine combustion	19
1.2.7.1 0D/1D single zone models	19
1.2.7.2 Quasi-dimensional models	20
1.2.7.3 Multidimensional models	21
1.2.7.4 Single zone compression ignition engine models	21
1.2.7.5 Emission models	26
1.2.7.6 Simulation software	29
1.2.8 Summary	30
1.3 Aims and Objectives	30
1.3.1 Aims	30

1.3.2	Objectives	31
1.4	Thesis structure	31
2	Experimental Setup	33
2.1	Introduction	34
2.2	Test fuels	35
2.3	Engine test bench	36
2.3.1	Engine and dynamometer control software	38
2.3.2	ECU control software	39
2.3.3	Test bench fuel system	40
2.3.4	Test bench exhaust system	42
2.3.4.1	NOVA gas analyser	43
2.3.4.2	TESTO 350 gas analyser	45
2.3.4.3	Pegasor M-sensor	45
2.3.4.4	Mass airflow sensor	47
2.3.5	Combustion analysis	49
2.4	Closing remarks	51
3	Engine Simulation	53
3.1	Introduction	54
3.2	Ricardo WAVE simulation development	54
3.2.1	Geometric data	56
3.2.2	Engine data	56
3.2.2.1	Valve characteristics	57
3.2.2.2	Exhaust gas recirculation	58
3.2.2.3	Fuel injection	59
3.2.3	Engine operating sub-models	60
3.2.3.1	Combustion sub-model	60
3.2.3.2	Emissions sub-models	63
3.3	Ricardo IGNITE development	65
3.3.1	General set-up	67
3.3.2	Validation of simulation	67
3.4	Co-simulation set-up	73
3.5	Closing remarks	74
4	Optimising emissions reduction using biofuel	75
4.1	Introduction	76
4.2	Experimental set-up	77
4.2.1	Design of experiment set-up	77

4.2.2	Flushing Procedure	78
4.2.3	Mixture stability	79
4.3	Results	80
4.3.1	Evaluation of CO ₂ emissions	80
4.3.2	Evaluation of CO emissions	83
4.3.3	Evaluation of NO _x emissions	85
4.3.4	Evaluation of fuel consumption	87
4.3.5	Mixture optimisation	89
4.3.5.1	Optimising towards a binary blend	89
4.3.5.2	Optimising towards a ternary blend	92
4.4	Closing remarks	95
5	Emissions reduction using low temperature combustion	97
5.1	Introduction	98
5.2	Experimental set-up	98
5.2.1	Experimental design set-up	99
5.2.2	Co-simulation model	103
5.2.2.1	WLTP drive cycle	104
5.2.2.2	Validating Ricardo WAVE combustion model	106
5.2.2.3	Validating Ricardo WAVE emissions model	108
5.3	Results	110
5.3.1	CO emissions	113
5.3.2	CO ₂ emissions	118
5.3.3	NO _x emissions	119
5.3.4	PN/PM emissions	123
5.3.5	Optimising engine parameters	124
5.4	Closing remarks	126
6	Conclusion and future work	129
6.1	Conclusions	129
6.2	Recommendations for future work	132
	References	135
	Appendix A Supplementary information	147

List of figures

1.1	Legislative drive cycles.	5
1.2	Supply of renewable fuels against the RTFO energy targets.	6
1.3	Biofuel manufactured in the UK using waste feedstock.	9
1.4	Comparison of engine operating points as discussed in literature compared to the operating points in the WLTP drive cycle.	14
1.5	EGR set-up	16
1.6	Engine injection strategies.	17
1.7	Schematic of the heat release rate in a direct injection diesel engine.	23
1.8	Visual representation of the double Wiebe equations.	24
2.1	UWE engine test cell set up.	37
2.2	Engine test cell control room.	37
2.3	Engine test cell layout.	38
2.4	Layout of the engine test cell's fuel system.	40
2.5	Change in red spectrum for the fuel samples taken after each fuel system flush.	42
2.6	Gas analysers used for engine exhaust measurement.	43
2.7	Visual representation of the working principle of the Pegasor M-sensor.	46
2.8	Calibration of MAF output signals.	48
2.9	Simulated and measured motored cylinder pressure.	50
2.10	Log p-log V diagram at 75% load at 3000 rpm	51
3.1	Engine simulation in Ricardo WAVE	55
3.2	Discharge coefficient of the inlet valves and outlet valves	58
3.3	Control diagram of EGR used in Ricardo WAVE model.	59
3.4	Illustration of parameters used by Ricardo WAVE.	62
3.5	In-cylinder pressure profile comparison between steady-state experimental data and simulated data.	63
3.6	Illustration of a different simulated injector operating events.	64

3.7	CO engine emissions comparison between steady state experimental data and simulated data for different engine speeds	65
3.8	NO _x engine emissions comparison between steady state experimental data and simulated data for different engine speeds	66
3.9	Vehicle simulation in Ricardo IGNITE	68
3.10	Comparison between Ricardo IGNITE and calculated engine speed for the NEDC.	69
3.11	Illustration of simplifying the complex inertia system of the powertrain.	70
3.12	Coefficients for vehicle tyre rolling resistance calculations.	72
3.13	Comparison between Ricardo IGNITE and calculated engine load for the NEDC.	72
3.14	Wiring connector between Ricardo WAVE and Ricardo IGNITE. . .	73
4.1	Extreme vertices simplex design plot of the mixture DoE.	78
4.2	Qualitative check for blend stability for E20 fuel blend.	79
4.3	Contour plot of the engine response over the WLTP for CO ₂ emissions in grams per kilometer.	82
4.4	Contour plot of the engine response over the WLTP for CO emissions in grams per kilometer.	84
4.5	CO emissions comparison between B3E14 and diesel.	84
4.6	Contour plot of the engine response over the WLTP for NO _x emissions in grams per kilometer.	86
4.7	NO _x emissions comparison between B3E14 and diesel.	87
4.8	Contour plot of the engine response over the WLTP for fuel consumption in grams per kilometer.	88
4.9	Variation of CO ₂ , NO _x and CO with increasing amounts of ethanol in diesel	90
4.10	Variation of CO ₂ , NO _x and CO with increasing amounts of biodiesel in diesel	91
4.11	Optimisation plot for engine emissions for the fuel blend E11. . . .	93
5.1	Central Composite Design.	99
5.2	ECU maps for different EGR percentages used in the RSM.	100
5.3	Baseline ECU map for the main injection SOI.	101
5.4	Total fuel delivered to the engine.	103
5.5	Visual representation of the parameters listed in Table 5.2	103
5.6	Available engine power for each gear ratio.	105
5.7	Fitting of Wiebe combustion model to experimental combustion heat release data.	107

5.8	In-cylinder pressure profile comparison between steady-state experimental data and simulated data for tests with B2E9.	109
5.9	Engine emissions comparison between steady-state experimental data and simulated data for tests with B2E9.	109
5.10	Response plots for the experimental CO emissions when engine operating conditions are varied.	114
5.11	Response plots for simulated CO emissions when engine operating conditions are varied.	115
5.12	CO emissions comparison with θ_{pinj} at 9 CAD and 17 CAD (test 8 & 15).	116
5.13	Response plots for experimental NO _x emissions when engine operating conditions are varied.	120
5.14	Response plots for simulated NO _x emissions when engine operating conditions are varied.	120
5.15	Comparison between experimental NO _x emissions and simulated NO _x emissions for run 1.	121
5.16	NO _x emissions comparison with EGR at 12.5% and 37.5% (test 2 & 8).	122
5.17	Main and Interaction plots for PM/PN emissions when engine operating conditions are varied.	124
5.18	Optimisation plot for the engine emissions RSM.	125

List of tables

1.1	GHG emission reduction targets below 1990 levels.	4
1.2	Euro legislation changes.	5
1.3	Summary of effects of binary blends on harmful emissions.	12
1.4	Summary of effects of ternary blends diesel, biodiesel and ethanol on harmful emissions.	14
1.5	Effect of different LTC strategies on combustion temperature and air-fuel mixture.	18
1.6	1D simulation packages comparison.	29
2.1	Equipment used in experimental runs.	35
2.2	Main fuel properties of neat test fuels.	35
2.3	Engine set up for experimentation.	36
2.4	Method and accuracy of the NOVA 7466K used to measure engine emissions.	44
2.5	Recorded points from gas analyser screen.	45
2.6	Gas analyser linear regression line constants and confidence interval	45
2.7	Method and accuracy of the TESTO 350 used to measure engine emissions.	46
3.1	Characteristics of the engine.	56
3.2	PI gain factors for EGR control.	59
3.3	Statistical analysis of the maximum measured in-cylinder pressure .	60
3.4	User defined values for $AERC_1$ for the NO_x emissions sub-model. .	65
3.5	Ricardo IGNITE input data.	67
3.6	Gear ratios used in Ricardo IGNITE.	67
3.7	PI gain factors for IGNITE driving model.	68
4.1	Physiochemical properties of diesel, biodiesel, ethanol and their blends.	77
4.2	The experimental values of the engine response for the mixture DoE.	81
4.3	P-values of the engine response for the mixture DoE.	81

4.4	Comparison of equivalent carbon dioxide Well-To-Tank emissions for diesel and renewable fuels.	90
4.5	Optimisation lower and upper limits.	93
4.6	Summary of results showing the change in emissions compared to pump diesel	94
5.1	Physiochemical properties of B2E9.	99
5.2	Independent variables and their levels for a central composite design RSM.	100
5.3	Required data for engine gear selection determination.	105
5.4	Constant values for Wiebe parameter regression models	108
5.5	User defined values for $AERC_1$ for the NO_x emissions sub-model for engine tests using B2E9 fuel.	110
5.6	The simulated and experimental values for the engine emissions for the RSM.	111
5.7	P-values for the engine response of the simulated and experimental RSM	112
5.8	Summary of results showing the change in emissions compared to pump diesel	126
A.1	Description of the elements used in Ricardo WAVE.	147
A.2	Description of the elements used in Ricardo IGNITE.	151
A.3	Target fuel pressure	153
A.4	Main fuel pulse width.	154
A.5	Main injection start of injection.	155
A.6	Pilot fuel pulse width.	156
A.7	Pilot injection start of injection.	157
A.8	Exhaust gas recirculation.	158
A.9	Statistical analysis of the maximum measured in-cylinder pressure.	159
A.10	Statistical analysis for the maximum in-cylinder pressure for steady state tests using B2E9.	160
A.11	Statistical analysis of recorded points using the gas analyser.	161

Nomenclature

Roman Symbols

A	Area, m^2
a	Wiebe parameter
$AERC_1$	Exponent multiplier
ARC_1	Pre-exponent multiplier
b	Regression line coefficient
C_d	Coefficient of drag
C_D	Discharge coefficient
c_v	Heat capacity at constant volume, J/K
D	Diameter, m
E_a	Fuel activation energy, J
f_m	Mass factor
F_a	Aerodynamic forces
F_r	Rolling resistance forces
G_f	Final drive ratio
g	Gravimetric acceleration constant, m/s^2
G_t	Current gear ratio selected
h	Enthalpy, J
I	Inertia, kgm^2

K_{c12}	Equilibrium rate constant
K_i	Integral gain factor
K_p	Proportional gain factor
L	Lift, m
\dot{m}	Mass flow, kg/s
m	Mass, kg
n	Engine rotational speed, rpm
P	Power, W
p	Pressure, Pa
PPS	Pegasor sensor signal
\dot{q}	Specific heat, J/kg
Q	Volume flow rate, L/s
q	Heat, J
R^2	Coefficient of determination
R	Radius, m
R	Universal gas constant, J/mol
r	Transmission ratio
T_a	Fuel activation temperature, K
T	Temperature, K
T	Torque, Nm
t	Time, s
U_{dyn}	Dynamic rolling circumference of a wheel
U	Internal energy, J
V	Volume, m ³

v	Speed, m/s
W	Work, J
x_b	Mass fraction of fuel burned

Greek Symbols

α	Rational acceleration, rad/s
β	Ratio between the fuel burned by premixed combustion and the total fuel burned
$\Delta\theta_{comb}$	Combustion duration, CAD
$\Delta\theta_{inj}$	Injection duration, CAD
η_{tf}	Efficiency of the driveline
γ	Heat capacity ratio
ϕ	Equivalence ratio
ρ	Density, kg/m ³
τ	Ignition delay period, s
θ	Crank angle degree, CAD
θ_{comb}	Start of combustion, CAD

Subscripts

0	Inlet
ax	Wheel axle
B	Biodiesel
C	Valve curtain
c	Clutch
D	Diesel
d	Diffusion combustion
dr	Drive shaft

E	Ethanol
e	Engine
f	Differential
f	Fuel
fr	Frontal
g	Gear
max	Maximum
min	Minimum
minj	Main injection
p	Premixed combustion
pinj	Pilot injection
R	Reference
T	Outlet
t	Transmission
v	Valve
v	Vehicle
w	Wheel

Other Symbols

Ar	Argon
CO ₂	Carbon dioxide
CO	Carbon monoxide
H ₂	Hydrogen
H ₂ O	Water
HC	Hydrocarbon

HCN	Hydrogen cyanide
N	Nitrogen
NO ₂	Nitrogen dioxide
NO	Nitrogen monoxide
NO _x	Oxides of Nitrogen
O ₂	Oxygen
OH	Hydroxide
PM	Particulate matter
PN	Particulate number
THC	Total hydrocarbons

Acronyms / Abbreviations

aBDC	After bottom dead center
ANOVA	Analysis of variance
aTDC	After top dead center
bBDC	Before bottom dead center
BEIS	The Department for Business, Energy & Industrial Strategy
BMEP	Brake Mean Effective Pressure
CAD	Crank angle degree
CCD	Central composite design
CFD	Computational Fluid Dynamics
CFPP	Cold flow plugging point
CI	Compression ignition
COP	Convention of the Parties
CR	Compression ratio

DAQ	Data acquisition system
DECC	The Department of Energy & Climate Change
DfT	The Department for Transport
DoE	Design of Experiment
ECU	Engine control unit
EGR	Exhaust Gas Recirculation
EPMA	Early pilot main after
EPM	Early pilot main
EU	The European Union
EVC	Exhaust valve closing
EV	Electric Vehicle
EVO	Exhaust valve opening
FC	Fuel consumption
GHG	Greenhouse gas
HiL	Hardware in the loop
IC	Internal combustion
ID	Ignition delay
IVC	Inlet valve closing
IVO	Inlet valve opening
LHV	Lower heating value
LTC	Low Temperature Combustion
MAF	Mass airflow sensor
MS	Million samples
NDIR	Non-dispersive infra-red

NEDC	New European Driving Cycle
OEM	Original equipment manufacturer
OLEV	The Office for Low Emissions Vehicles
PHEV	Plug-in Hybrid Electric Vehicle
PMA	Pilot main after
PM	Particulate mass
PN	Particulate number
RDE	Real Driving Emissions
RED	Renewable Energy Directive
RME	Rapeseed methyl ester
RSM	Response Surface Method
RTFO	Renewable Transport Fuel Obligations Order
SOC	Start of combustion
SOI	Start of injection
StDev	Standard deviation
TDC	Top dead center
TPS	Throttle position
UK	The United Kingdom
ULEV	Ultra Low Emission Vehicles
UNFCCC	United Nations Framework Convention on Climate Change
USA	United States of America
UWE	University of the West of England
VGT	Variable geometry turbine
VW	Volkswagen

WCC	World Climate Conference
WLTP	World Harmonised Light Vehicle Test Procedure
WTT	Well to tank
WTW	Well to wheel

Chapter 1

Introduction

1.1 Opening statements

It is generally agreed by the scientific community that climate change is a reality and steps need to be taken to prevent irreversible and catastrophic damage [1]. A push from government as well as international bodies such as the European Union to decrease our dependence on fossil fuels for energy has seen the power generated from coal rapidly decreasing. Demand for coal in 2016 fell by almost 59 % when compared to 2015 and coal's contribution to electricity generation fell from 22.1 % in 2015 to 1.0 % in 2019 [2]. This decrease in coal used resulted in carbon dioxide emissions dropping by 7 % between 2015 and 2016 [2]. The UK made headlines in April 2017 when it was reported that for a whole day electricity was generated without the use of any coal. A first since the Industrial revolution in 1882 [3].

In the transport sector, the same trends are evident. New technologies are being developed and purchases of ultra low emissions vehicles (ULEV) are rising due to government grants promoting their use. These vehicles include fully electric vehicles (EVs) and plug in hybrid electric vehicles (PHEV). The UK government hopes to reach its 2020 target of 10 % renewable energy in transport with the promotion of ULEVs as well as increasing its use of renewable fuels (discussed in more detail in Section 1.2). ULEVs make up 2.2 % of all newly registered cars and vans in the UK at the end of 2018 [4].

Focus has recently shifted to non-CO₂ emissions such as NO_x and PM after the VW emissions scandal¹ and Client Earth's case² against the government. Subsequently, diesel driven vehicles were identified as producing the most NO_x and PM emissions and their image as polluting vehicles increased. Major cities such as

¹More info at <http://www.bbc.co.uk/news/business-34324772>

²More info at <https://www.clientearth.org>

Bristol will ban diesel cars from entering certain areas and other countries such as the Netherlands and Norway want to completely ban the use of internal combustion (IC) engines by 2025 [5]. The mayor of London, Sadiq Khan, has launched a toxicity charge of £10 aimed at compression ignition vehicles registered before 2006. The Mayor is also calling for a diesel scrappage fund and has doubled funding to £875 million to tackle air quality in London [6]. The UK also announced in 2018 that it will ban the sale of all new non-electrified internal combustion engine vehicles from 2040 onwards [7] and in 2020 has launched a consultation to see if it is feasible to bring this target forward to 2035.

Even though compression ignition vehicle emissions are given as the reason for the poor air quality in most major cities, compression ignition vehicle purchases still account for 31% of all new vehicles being bought in 2018 [4]. The taxation of older compression ignition vehicles as well as the removal of some compression ignition vehicles from major cities is a short term solution to the air quality problem, but it is not sustainable. A more long term measure needs to be in place to promote the gradual transition to a zero emissions transport environment by 2050.

As such the overarching aim of this research is to identify an alternative fuel blend that can be used in diesel vehicles currently on UK roads to reduce emissions as well as increase the renewable content of the fuel, ultimately assisting in the transition towards net zero emissions in transport. This will be explored further in the following chapters.

1.2 Biofuels and future legislation: A review

1.2.1 Combating climate change

Throughout the past two decades of history, climate policy has evolved and cumulated into the United Nations Framework Convention on Climate Change (UNFCCC) and its Kyoto Protocol which emerged and matured in the 1990s and early 2000s as well as the later Paris Agreement in 2015. It started off with the first World Climate Conference (WCC) in 1979, mostly attended by scientists, that called upon world governments to anticipate and guard against potential man-made changes in the earth's climate that might be adverse to the well-being of humanity. Then followed the UNFCCC which was set up as an intergovernmental treaty developed to address the problem of climate change, formally entering into force in 1994, having being ratified by 50 countries. The first Convention of the Parties (COP) took place in Berlin in 1995. Parties to the UNFCCC continue to meet regularly to take stock of progress in implementing their obligations under the treaty, and to consider further actions

to address the climate change threat. The parties have also negotiated a protocol to the Convention called the Kyoto Protocol that was first agreed in December 1997 in Kyoto, Japan. It obliges industrialised countries prepared to take positive steps to curb emissions of carbon dioxide and other greenhouse gasses (GHGs) from sources within their remit. Countries were required to cut their emissions of greenhouse gases compared with 1990 levels. The Kyoto Protocol only entered into force in 2005 following the ratification by 55 Parties to the UNFCCC that represented at least 55 % of the group's total carbon dioxide emissions for 1990. The first commitment period of the Kyoto Protocol called on countries to reduce their greenhouse gas emissions between 2008 and 2012 based on their 1990 emissions. The second commitment period applies between 2013 and 2020. Countries such as the USA, Canada and New Zealand withdrew from the second commitment period, which resulted in the commitment period only applying to approximately 11 % of the annual global emissions of GHGs. On 4 November 2016, the Paris Agreement entered into force, with 186³ countries that ratified the agreement, covering approximately 89 % of global GHG emissions. The United States (US) recently notified the UN of its intention to withdraw from the Paris Agreement which will take place on 4 November 2020. The US is responsible for approximately 15% of global CO₂ emissions. The Paris Agreement addresses crucial areas that are necessary to combat climate change:

- Reaffirms the long-term climate goal to limit the global temperature increase well below 2 °C.
- To reach global peaking of GHG emissions as soon as possible.
- To prepare nationally determined contributions to GHG reductions.
- To conserve and enhance sinks and reservoirs of GHGs which include forests.
- Enhance climate change education, training and public awareness.
- Ensure a global stock take is possible to assess the collective progress to ensure targets can be updated and enhanced.

Table 1.1 shows targets as set out by the Kyoto Protocol and Paris Agreement for different countries. The target of the EU needs to be met by all member states collectively.

³As of December 2019.

Table 1.1: GHG emission reduction targets below 1990 levels [8].

Country	Kyoto Protocol		Paris Agreement
	2008-2012	2013-2020	present - 2030
EU (combined)	-8 %	-20 %	-40 %
USA	-7 %	N/A	-16 %
Canada	-6 %	N/A	-15 %
Australia	8 %	-5 %	-21 %
Norway	1 %	-30 %	-30 %

1.2.2 The European Union and climate change

The European Union (EU) has set out climate and energy targets for 2020 as part of their commitments to the Kyoto Protocol to combat climate change, increase energy security and strengthen its competitiveness. These targets can be summarised as follows [9]:

- 20 % reduction in EU greenhouse gasses from 1990 levels (Table 1.1).
- 20 % improvements in EU's energy efficiency.
- 20 % of EU energy from renewable energy.

As part of reducing the EU's GHG emissions, focus on decreasing emissions from transport has become important. Transportation is the second largest source of greenhouse gasses at 25% of total greenhouse gas emissions (energy sector is highest at approximately 54% of total emissions). In particular passenger cars account for around 12% of CO₂ emitted in the EU in 2015 [10].

In order to decrease the amount of CO₂ emitted by vehicles in the EU, a legal limit on CO₂ emissions of 130 g/km has been implemented in 2009. However, this will be reduced to 95 g/km by 2020 [11]. The CO₂ limit effectively places a fuel consumption constraint on the vehicles. Manufacturers are fined an 'excess emissions premium' for each car registered that exceeds the target. In addition to regulation of CO₂ additional regulations have been introduced to limit the emission of other harmful gases. The EU has implemented successive emission standards to try and reduce the environmental impact of road transport in the form of the European emission (Euro) standards. The Euro standards state the acceptable limits for harmful gasses in vehicle exhaust such as carbon monoxide (CO), total hydrocarbons (THC), oxides of Nitrogen (NO_x), particulate matter (PM) emissions and particulate number (PN) emissions. The regulation was updated in 2009 (Euro 5) to include the measurement of particulate matter by number as well as by mass for diesel cars [12]. Since

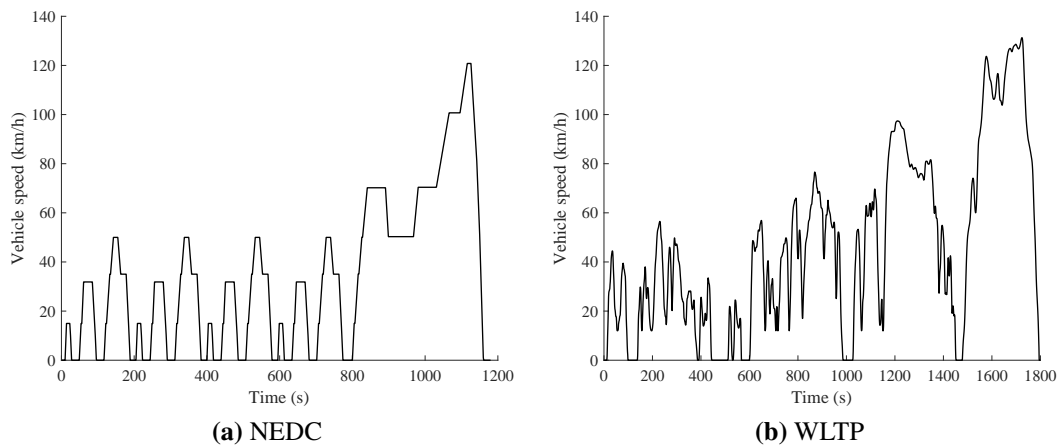


Figure 1.1: Legislative drive cycles.

September 2018, the Euro 6d legislation has been in force [13]. Table 1.2 shows the changes in Euro emissions legislation from 1992 with the Euro 1 limits to the Euro 6d limits. Figure 1.1a shows the vehicle speed trace for the NEDC that is followed

Table 1.2: Euro legislation changes from Euro 1 to Euro 6d for diesel passenger cars.

Emissions	Euro 1	Euro 6d
CO	2.72	0.50
HC	0.97	-
NO _x	-	0.08
PM	0.14	0.005
PN	-	6×10^{11}

when testing a vehicle's emissions. The test cycle was last updated in 1997 and has been criticised for not representing the road-user's everyday driving behaviour. This causes fuel consumption and emission measurements being unrepresentative of everyday driving [14]. The Real Driving Emissions legislative driving cycle (RDE) as well as the WLTP have been developed to ensure a more representative way of determining real world fuel consumption and emissions data. Emissions are currently tested over the World Harmonised Light Vehicle Test procedure to determine if the car complies with the Euro 6 standards. Figure 1.1b shows the speed trace of the WLTP. The RDE uses the road as the test environment, where weather conditions and traffic cannot be controlled and ultimately influences the result.

The third item of the EU's '20-20-20' plan is enforced by giving all the member countries binding targets to raise their share of renewable energy in their energy consumption by 2020. These targets are determined based on the individual country's use of renewable sources and the potential to increase their production. Targets range

from 10 % for Malta to 49 % for Sweden. The UK has a target of 15 %. Ultimately, all the individual targets will ensure the EU meets its target of 20 % by 2020. Included in the individual targets of each country, a 10 % share of renewable energy in the transport sector is required. This can be achieved using a combination of biofuels, hydrogen or *green* electricity [9].

1.2.3 Tackling air pollution in the UK

The UK has committed to deliver 15 % of the country's energy from renewable sources. The UK government has published sub targets for electricity, heat and transport from renewable sources of 30 %, 12 % and 10 %, respectively by 2020. These targets are transposed into UK law through the following directives:

- The Promotion of the Use of Energy from Renewable Sources Regulations.
- The Renewable Transport Fuel Obligations Order (RTFO).

The UK has reached its sub target of 30 % for renewable electricity in 2018 by increasing the use of wind power, solar power and other bio-energy generation capabilities [15, 16]. Wind power contributed to approximately 60 % of all renewable energy generated, followed by solar photovoltaic electricity generation (12 %) and hydro electricity generation (6 %). The 10 % renewable energy target for transport can be seen in Figure 1.2. The RTFO came into effect in 2011 to ensure that a

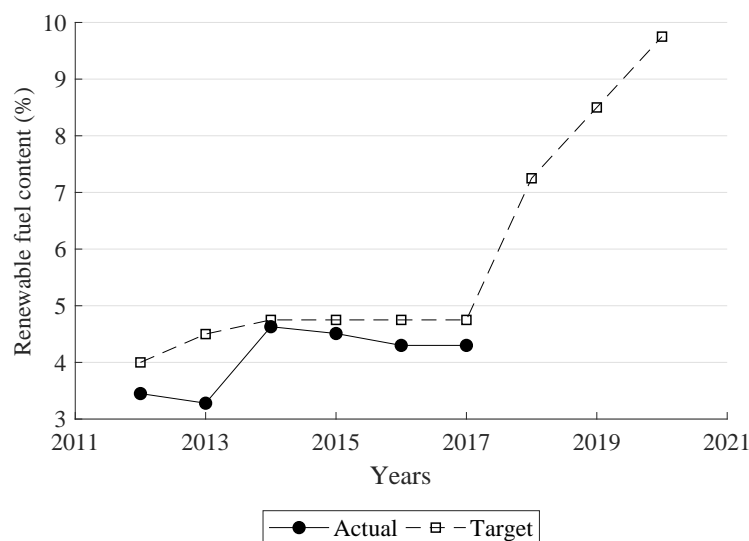


Figure 1.2: Supply of renewable fuels against the RTFO energy targets [17, 18].

proportion of fuel supplied to the general public comes from renewable sources. The renewable fuel must also pass sustainability criteria which include the use of low

impact land to grow the fuel feedstock. This is to ensure food supply is not impaired and forests are not cut down to make way for additional feedstock planting. A cap of 4.75 % renewable fuel has been active as part of the RTFO until April 2018 when new targets were announced that covers a period until 2032. A crop cap was also introduced to limit the production of biofuels from land cultivated crops and promote the use of biofuel using waste sources such as waste cooking oil. Fuels that are still in development are also included in the RTFO from 2019 onwards as well as aviation fuels and hydrogen. The new targets introduced in April effectively aim to almost double the renewable content in transport energy in two years, after a stagnation period between 2014 and 2017. The RTFO's 2020 target will also ensure the UK reaches its obligation of 10 % renewable energy content in the transport sector.

1.2.4 Biofuel as an alternative fuel

Fuels produced from renewable sources have the potential to help minimise fossil fuel burning and CO₂ emissions. The plants or organic waste used to produce biofuel help close the CO₂ emissions loop, as the CO₂ emitted by the biofuels are used to grow new biomass to produce biofuel. Biofuels are categorised into three generations. The first generation biofuel technology is firmly established and the production is at a commercial level. The second generation biofuel technology addresses some concerns that is found with the production of first generation biofuel and the third generation biofuels are mainly referring to the use of algae biomass as fuel feedstock. Each generation is discussed in more detail in the following sections.

1.2.4.1 First generation biofuel

The two main first generation biofuels in the UK are biodiesel (bio-esters) and bioethanol. The production process of first generation biofuel is considered an established technology and large quantities of the biofuel are produced all around the world. The UK has reported at the end of April 2018 that 1,518 million litres of renewable fuel was supplied to the market of which 58 % is biodiesel and 36 % is bioethanol. Biodiesel is produced through transesterification of vegetable oils and fats and can be mixed together with petroleum diesel to be used by diesel vehicles. Transesterification or alcoholysis is the displacement of alcohol from an ester by another in a process similar to hydrolysis, except an alcohol is used instead of water. The reaction is reversible and proceeds essentially by mixing the reactants. However, the presence of a catalyst (a strong acid or base) accelerates the conversion. The most commonly used catalyst for transesterification, is sulphuric acid. It takes approximately 3 hours to complete the conversion at temperatures higher than 100 °C.

The product of the reaction is a mixture of methyl esters, which is the biodiesel, and glycerol, which is a high value co-product used in the food and cosmetic industry. From 2008 until 2011, the main feedstock used to produce biodiesel, was soybean oil. Waste cooking oil is the main feedstock for biodiesel production since 2012 as it is seen as a waste product that does not impact the food industry prices.

Bioethanol is produced through fermentation using sugar or starch feed stocks. Feed stocks that can be used in the fermentation process include:

- Sugar containing crops: sugar cane, wheat, beet root.
- Starch containing crops: wheat, rice, corn.
- Cellulosic biomass: wood waste, agricultural residues.

From 2008 until 2013, the main feedstock used to produce ethanol in the UK was corn, but by April 2018, it has changed to sugar beet.

1.2.4.2 Second generation biofuel

First generation biofuels have the problem of being limited to available feedstock. The increased use of edible feedstock (non-waste) such as vegetable oils, have a negative impact on food prices and food security. The focus shifted to waste feedstocks such as non-edible vegetable oils, plant waste biomass such as agricultural and forest residues and grass and aquatic biomass. The use of waste cooking oil as a feedstock for the transesterification process also counted under second generation biofuel production, as it is using a waste feedstock compared to virgin vegetable oils, which are classified as non-waste. The sourcing of more sustainable feed stocks for producing biofuel has the benefit of achieving a carbon neutral or even carbon negative rating when it comes to CO₂ emissions.

The use of advanced technologies such as hydrotreating and Fisher-Tropisch are methods used to convert the biomass to usable biofuel. The technologies are not yet commercialised and still in demonstration phase. This is evident by the fact that only 0.1 % of the total biofuel supplied in the UK by April 2018, was produced using hydrotreating. The production of second generation biofuel is being realised as seen in Figure 1.3 where waste cooking oil, food waste and category 1 tallow (high risk to human health) are being used as a feedstock for biodiesel. The production of bioethanol in the UK still uses non-waste feedstock such as corn, wheat and sugar cane.

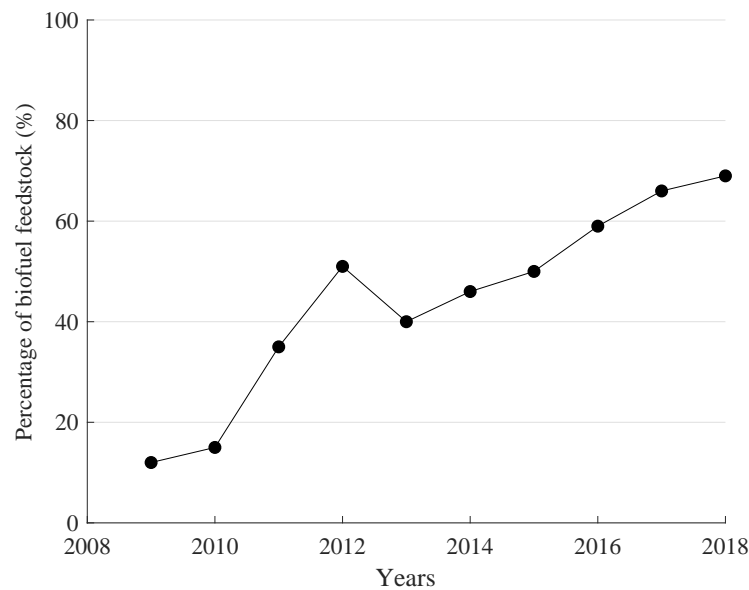


Figure 1.3: Biofuel manufactured in the UK using waste feedstock [17, 18].

1.2.4.3 Third generation biofuel

Third generation biofuel mainly refers to the use of algae as a feedstock when producing biofuels. The list of biofuels that can be produced from algae as a feedstock are:

- Biodiesel
- Ethanol
- Gasoline
- Jet Fuel
- Methane
- Butonal

The diversity of algae feedstock to produce a diversity of fuels are mainly due to the fact that algae produces an oil that can be refined into diesel and gasoline components. Algae can also be manipulated genetically to produce fuel such as ethanol and butanol directly. Butonal is of interest as it is similar to gasoline in energy density with improved emissions characteristics. It is beneficial to use butanol in spark ignition engines compared to ethanol, as butanol does not damage the engine or require engine modification to use high percentages in the fuel content. Algae also has the benefit of high yield levels compared to other first and second generation feedstocks and can be as much as ten times that of second generation biofuel feedstocks. This is

beneficial when land use is considered, as the production of third generation biofuel will not require as much land area to produce the same amount of biofuel compared to second generation feedstocks. The cultivation of algae can be categorised into three groups:

- **Open ponds:** Algae is grown in big ponds. Ponds are simple and have low capital cost. The downside of open ponds is that they are not as efficient, require a lot of water and the algae can be killed by other organisms that contaminate the water.
- **Closed-loop systems:** Similar to open ponds, but they are not exposed to the atmosphere and use carbon dioxide from smoke stacks or other CO₂ producing facilities.
- **Photobioreactors:** Most advanced system to cultivate algae. Photobioreactors require high capital investment, but their yield are the highest of the three systems.

Closed loop systems for the use of algae cultivation have the benefit of using the carbon dioxide emissions from industry to produce fuels. Total CO₂ emissions from installations such as power plants or other high emitting industry processes can be reduced significantly when paired up with an algae producing facility. A downside to the use of algae as a feedstock is the large amounts of water, nitrogen and phosphorus required to grow it. The production of fertilizer that will be used in the cultivation of algae can sometimes offset the CO₂ saved when using algae as a biofuel feedstock [19]. The harvesting of the algae lipids is also energy intensive. Algae derived fat is also highly unsaturated, which can cause fuel derived from algae to degrade quickly, especially in high temperatures. Algae research is still ongoing to make it sustainable, with breakthroughs such as increasing the fat content of algae strains from approximately 20 % to about 40 % [20]. This drastically increases the yield from algae feedstock for the use in biofuel production.

1.2.5 Biofuel in the transport industry

The target content of biofuel used in the transport industry in the UK is 10 % by 2020 (discussed in Section 1.2.3). Until April 2018, biofuel was used as a drop in fuel together with fossil fuels and made up a maximum of approximately 5 % of the fuel available at pump stations. This section focuses on the emission production behaviour of biodiesel and ethanol when used in a compression ignition engine in binary and ternary blends together with petroleum diesel. Studies conducted on

biodiesel and ethanol used blends ranging from pure biodiesel (B100) to binary blends with petroleum diesel (B20, B40, E10, E20) and ternary blends (B20E2, B40E5 etc.). The 'B' denotes the percentage of biodiesel in the blend by volume. Similarly, the 'E' denotes the percentage of ethanol in the fuel blend by volume.

Numerous studies concluded that biodiesel, as a renewable fuel, represents a more sustainable source of energy in the transport industry [21–23]. The use of biodiesel also significantly reduces PM emissions, CO emissions as well as HC emissions due to its high oxygen content and lower aromatic compounds when compared to petroleum diesel [24]. Palash *et al.* [25] reported a 9.86 % and 22.32 % drop in HC emissions for B5 and B10, respectively. Bannister *et al.* [26] concluded that by increasing the blend ratio of biodiesel a reduction of 20-25 % in HC emissions can be achieved. Qi *et al.* [24], Lin *et al.* [27] as well as Xue *et al.* [28] and Lapuerta *et al.* [29] reported a drop in soot and HC emissions and contributed it to the high oxygen content of biodiesel as well as the absence of aromatic content. Bakeas *et al.* [30] investigated the use of high percentage of soybean methyl ester together with diesel and found that PM emissions do not reduce significantly when using high concentrations of biodiesel blends over a cold-start driving cycle. Bakeas *et al.* [30] suggests that the combined effect of the cold-start phase and the lower volatility of biodiesel negatively influenced the formation of PM emissions during the NEDC. This could be a consequence of the poorer combustion due to biodiesel's lower fuel vaporization at low temperatures. Zhu *et al.* [31] contributed the reduction in PM emissions with the use of biodiesel to the higher oxygen content of biodiesel which leads to more complete oxidation. Tsolakis [32] reported that compared with diesel fuel, biodiesel led to a reduction in particulate mass emissions due to advanced combustion, which moved the maximum heat release closer to TDC thus resulting in higher combustion temperatures. Moreover, biodiesel contains less aromatics than that of diesel fuel. The reduction of PM emissions can thus also be due to the dilution of aromatics in the fuel blend, which are soot precursors.

However, NO_x emissions generally rise with the use of biodiesel, one of the reasons being its higher oxygen content which results in higher in cylinder temperatures. Lahane and Subramanian [33] found that for blends of up to B15 NO_x emissions increases marginally and beyond B15, NO_x emissions will increase significantly. Binary blends of biodiesel with conventional diesel, especially B20 [33, 34], is seen as the best option to use in diesel vehicles without the need to modify the engine while still getting a reduction in regulated emissions.

Binary blends of ethanol also have the benefit of reducing regulated emissions. Huang *et al.* [35] found that binary blends of E10 reduced CO emissions by approximately 31 % and NO_x emissions of approximately 6 %. By increasing the percentage

of ethanol in the blend by more than 10 %, CO emissions started to increase and NO_x emissions were reduced further by more than 34 %. Xing-cai *et al.* [36] reported similar trends when increasing the ethanol content in the fuel and contributed the rise in CO emissions due to ethanol's high latent heat of evaporation. By increasing the ethanol content, the cooling effect of ethanol causes incomplete combustion. High percentages of ethanol can also cause an increase in ignition delay due to its low cetane number, which also results in incomplete combustion. The cooling effect of ethanol's high latent heat of evaporation has a positive effect on NO_x emissions. By increasing the ethanol content in the fuel blend, the combustion temperature is reduced and therefore less thermal NO_x is produced during combustion [35]. Rakopoulos *et al.* [37] also found that the addition of ethanol to diesel increases the fuel consumption of the engine due to ethanol's lower calorific value. As the percentage of ethanol increases in the blend, the fuel consumption also increases [38].

Table 1.3 shows a summary of the effects of binary blends of diesel and biodiesel and diesel and ethanol and their effects on harmful emissions. In the table a + represents a minor increase and – represents a minor decrease (a minor change is defined as $\leq 5\%$). The \circ represents an insignificant change ($\leq 1\%$) and double ++ and -- represent a significant change ($\geq 5\%$). The N/A label indicates that for the considered literature, the specific engine emission was not considered. From Table 1.3 it is evident that the benefits of using renewable fuels to reduce harmful emissions are dependent on engine operation. Biodiesel has a significant effect

Table 1.3: Summary of effects of binary blends on harmful emissions [24, 25, 27–29, 35, 37, 39–41].

	Biodiesel		Ethanol	
	Part load	Full load	Part load	Full load
NO _x	-	-	-	-
CO	\circ	--	++	--
HC	-	-	++	-
FC	+	+	++	+
CO ₂	N/A	+	-	-
PM	-	--	--	--

on harmful emissions reduction when the engine is operated at full load, but the reduction is less pronounced for part-load conditions. The same applies for binary blends between diesel and ethanol. The addition of ethanol to reduce harmful emissions is only effective when the engine is operating at high loads. Emissions such as CO and HC are increased at low and medium load conditions when running

with binary blends of diesel and ethanol. The summary shown in Table 1.3 reveals that because the emissions are affected by engine load, then the application of steady state tests to real world transient driving behaviour is limited.

Binary blends of ethanol with diesel have some technical barriers due to the miscibility of ethanol in diesel fuel. The addition of additives (emulsifiers) are required in order to run a compression ignition engine with a blend of ethanol and diesel. Biodiesel acts as an emulsifier for ethanol; the addition of biodiesel improves the miscibility of ethanol in diesel [34]. Studies of binary blends of biodiesel and diesel show that, generally, as the biodiesel is increased then the CO and HC emissions decrease and NO_x increases. Whereas binary blends of ethanol and diesel decrease NO_x and increase CO. Therefore the ternary blends of these fuels result in inconsistent results depending on the blend and the speed and load of the engine.

The ethanol in the ternary blend also improves the atomisation performance of the fuel, because the ethanol blended fuel has a low kinematic viscosity and surface tension [42]. Ethanol's high oxygen content improves combustion which can reduce the PM emissions even further when compared to binary blends of biodiesel and diesel. Randazzo and Sodr  [21] found that using ternary blends of B20E2 and B20E5 decreased CO₂ and NO_x emissions while slightly increasing HC and PM emissions. On the other hand, Zhu *et al.* [31] reported a slight decrease of HC, CO and NO_x emissions when adding small amounts of ethanol of up to 5 % compared to binary blends of biodiesel and diesel. Mofijur *et al.* [43] found that ternary blends significantly decrease the HC, PM and smoke emissions, while NO_x emissions increase slightly. An optimum amount of ethanol was found to be a maximum of E5 as per the results of Shahir *et al.* [38] which reduces soot and HC emissions. The lower heating value of ethanol and biodiesel as well as biodiesel's high density and high viscosity result in an increase in fuel consumption [38].

Table 1.4 shows a summary of the effects of ternary blends on the harmful emissions. The table shows that the chemical interaction effects between biodiesel and ethanol in a ternary blend is complex and also depends on load and/or speed of the engine. With such complex interactions between engine conditions and ternary fuel blends on the emissions, studies based on steady state results cannot be easily translated to the real world, where the engine speed and load is varied based on driver behaviour. To illustrate this, Figure 1.4 compares the variation of engine Brake Mean Effective Pressure (BMEP) with engine speed for the steady state engine points cited in this section in the literature and the current transient drive cycle (WLTP). As can be seen from Figure 1.4 the studies from the literature only cover a small proportion of the driving test cycle. This research aims to address the shortcomings of previous studies by investigating both the variation of engine conditions and ternary fuel

Table 1.4: Summary of effects of ternary blends diesel, biodiesel and ethanol on harmful emissions [41].

	Hulwan and Joshi [34]			Zhu <i>et al.</i> [31]		Khoobakht <i>et al.</i> [44]	Yilmaz <i>et al.</i> [45]	
%Biodiesel	10	10	10	15	15	20	49	43
%Ethanol	20	20	20	15	15	10	3	15
BMEP (MPa)	0.2	0.4	0.6	0.2	0.7	1.15	0.37	0.37
Speed (rpm)	1600	1600	1600	1800	1800	1900	3000	3000
NO _x	○	○	○	-	-	+	-	-
CO	+	○	○	+	○	-	○	+
HC	N/A	N/A	N/A	-	○	-	-	-
FC	+	+	+	++	+	N/A	N/A	N/A
CO ₂	+	+	+	N/A	N/A	+	N/A	N/A
PM	N/A	N/A	N/A	-	-	N/A	N/A	N/A

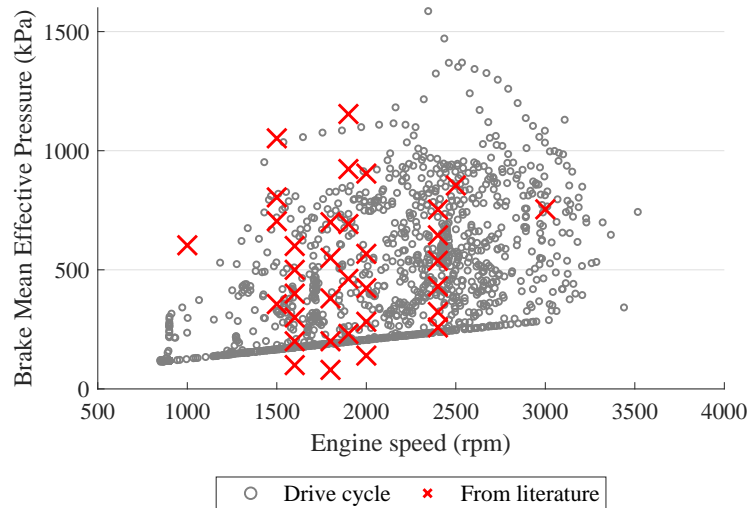


Figure 1.4: Comparison of engine operating points as discussed in literature compared to the operating points in the WLTP drive cycle [25, 28, 41, 43, 45–47].

blends on exhaust emissions.

1.2.6 Low Temperature Combustion

Emission reduction legislation has become tighter through history as shown in Table 1.2. In-engine strategies were used to reduce the engine's emission production, such as higher injection pressures, higher intake charge boosting, improved piston head geometry, adjustment of fuel injection timings and exhaust gas recirculation (EGR). Later Euro emission limits were and are being met with the combined use of after-treatment systems and in-cylinder strategies. Viable after-treatment systems are available to meet the new emission limits, but higher costs, durability issues, fuel economy penalties and ever-increasing space requirements limit the widespread adoption of the devices. The use of after-treatment systems to reduce NO_x emissions in compression ignition vehicles are especially difficult as it requires the use of a consumable. The use of a selective catalytic converter, together with an urea consumable, converts the NO_x into Nitrogen, water and CO₂. As a result, improvements to in-cylinder strategies to further reduce the engine-out emissions to decrease the burden put on after treatment systems and the cost of using consumables, are of great interest. The formation of NO_x occurs primarily in the thermal mechanism and production rates of NO_x increase exponentially with the increase of temperature. Accordingly, research has been focussed on decreasing the temperature of combustion with the use of strategies that can be collectively called Low Temperature Combustion (LTC) strategies.

1.2.6.1 Low Temperature Combustion

The overall goal of Low Temperature Combustion (LTC) is to achieve a reduction in peak combustion temperature. This can be achieved by the dilution of combustion materials in the cylinder by either ensuring the mixture is lean or that there is a moderate level of exhaust gas present. The exhaust gas increases the heat capacity of the combustion mixture, thus reducing the combustion temperature. Exhaust gas recirculation (EGR) is an established method for decreasing NO_x in the exhaust gas [48, 49]. As seen in Figure 1.5, hot exhaust gas (dark grey flow path) is introduced into the intake air (light grey flow path) and controlled with the use of a valve. EGR is measured in percentages and calculated using the following equation:

$$EGR_{fraction} = \frac{\dot{m}_{EGR}}{\dot{m}_{air} + \dot{m}_{fuel} + \dot{m}_{EGR}} \quad (1.1)$$

The application of EGR (usually < 50%) reduces the volumetric efficiency of the engine due to the rise in inlet charge temperature with less dense, hot exhaust gas replacing cool inlet air. The oxygen content of the combustion mixture is also reduced when using EGR. As a result, the local flame temperature during combustion is reduced, which reduces the formation of NO_x gasses [48, 50]. Unburned hydrocar-

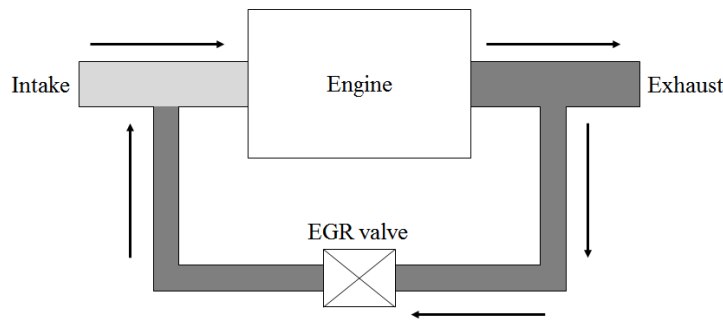


Figure 1.5: EGR set-up

bons (UHC) and CO emissions also increase with increasing use of EGR. To try and reduce PM emissions, increasing the fraction of the combustion mixture that burns in the premixed phase can decrease PM emissions. For blends with high oxygen content, Huang *et al.* [51] found that the high volatility and low cetane number enhances the mixing of the air and fuel which results in a more homogeneous mixture, which promotes complete combustion as the presence of oxygen can promote the particle oxidation process. He *et al.* [52] and Huang *et al.* [51] concluded that adding alcohols to the fuel blend dilutes the aromatics content of the fuel which tends to decrease the soot precursors. Also, longer ignition delay periods and larger proportions of premixed combustion can be a reason for lower PM emissions of higher alcohol fuel blends. Soot forms in the fuel-rich areas of the combustion zone and by increasing the premixed burn fraction, can reduce or eliminate fuel-rich zones. Multiple fuel injections can be used to achieve an increase in the premixed combustion fraction. Plamondon and Seers [53] found that while the addition of 20% waste cooking oil biodiesel to a binary blend increased PM emissions and decreased NO_x emissions with respect to diesel, a pilot and main injection strategy decreased both pollutants below the level observed with a single injection. There are many different configurations that can be used as seen in Figure 1.6. Most engines currently incorporate the pilot main (P-M) injection strategy. Biswas *et al.* [55] investigated the use of different multiple injection scenarios which include pilot, main and after injections (P-M-A) and early, pilot, main and after injections (E-P-M-A). The results show that adding an early injection to a P-M-A strategy lowers the NO_x , CO and THC emissions, while keeping PM emissions the same. The early injection promotes the mixture of

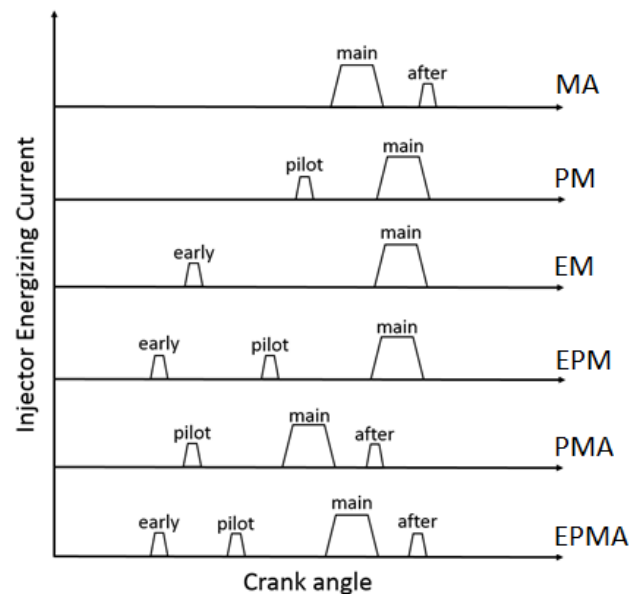


Figure 1.6: Different multiple injection strategies that can be used to implement low temperature combustion [54].

the fuel with the air in the cylinder and as the piston reaches top dead centre (TDC) it creates an almost homogeneous environment. Carlucci *et al.* [56] found that the duration and timing of injections such as the pilot injection have an effect on the formation of NO_x and PM emissions. By advancing the pilot injection timing, PM emissions can be reduced, as the pilot injection increases the main injection delay which results in the reduction of diffusive combustion. Zhang *et al.* [57] also reported a reduction in PM emissions by advancing the pilot injection. The pilot injection duration was shown to have a major effect on the formation of NO_x . By increasing the injection duration, cylinder temperatures will increase, resulting in an increase in NO_x emissions. The increased duration of the pilot injection also decreases the main injection delay, which reduces NO_x formation. Zheng *et al.* [48] also investigated the use of multiple injections and found that NO_x emissions decrease when the the main injection delay is increased. Mathivanan *et al.* [58] compared combustion of diesel using only a main injection with the emissions from combusting diesel using multiple injections. Multiple injections reduced the engine out NO_x emissions from approximately 381 ppm to 17 ppm. Mathivanan *et al.* [58] also reported that decreasing the duration of the pilot injection will result in the retarded combustion of the main injection, which decreases the formation of NO_x gasses. The use of multiple injections such as the E-P-M injection strategy as seen in Figure 1.6 can ultimately reduce both PM emissions and NO_x emissions.

For the purposes of this research, the LTC strategies will be categorised into two groups, strategies that reduces combustion temperature and strategies that increases

Table 1.5: Effect of different LTC strategies on combustion temperature and air-fuel mixture [60].

LTC strategy	Combustion Temperature	Charge Homogeneity
Increase pilot injection duration	+	+
Advance pilot injection SOI	+	+
Advance main injection SOI	+	–
Increase EGR percentage	–	+

the homogeneity of the air-fuel mixture. LTC technologies have contrasting effects on cylinder temperature and air-fuel mixture. Carlucci *et al.* [56] found that pilot injection combustion increases cylinder temperature, which increases NO formation, but it also reduces the main injection's ignition delay, which causes a decrease in the fraction of fuel burned in the premixed combustion phase which results in a decrease in NO_x formation. Also, the use of EGR increases the ignition delay of the main injection which promotes premixed combustion, but lowers the combustion temperature due to the increase in inert gasses in the inlet charge [59]. Table 1.5 summarises the effects that LTC technologies have on combustion temperature and charge homogeneity. The + sign indicates an increase in value and the – sign indicates a decrease in value. In order to use LTC effectively, it is necessary to optimise the use of different LTC techniques in a compression ignition engine to achieve emission reductions. This research aims to optimise the different LTC strategies identified in Table 1.5 to ensure their opposing and complimentary effects on the combustion temperature and charge homogeneity result in emissions reduction.

1.2.6.2 Using biofuel with LTC

The use of biodiesel together with ethanol, can drastically reduce the engine out emissions of diesel cars as discussed in Section 1.2.5. Although using biodiesel and ethanol increases the NO_x emissions due to higher in-cylinder temperatures, this can be mitigated using LTC. Mofijur *et al.* [43] reviewed the available literature and suggested that the NO_x emissions can be countered with the use of exhaust gas recirculation [48, 50]. Zhang *et al.* [57] reported that even though high percentages of EGR can inhibit mixing between air and fuel, thus increasing PM emissions even more, the oxygen content of biodiesel and ethanol permits increased use of EGR, resulting in less PM emissions than that of petroleum diesel. Zheng *et al.* [48] also showed that high percentages of EGR together with neat biodiesel can result in a decrease in NO_x emissions as well as soot emissions. High percentages of EGR is able to counter the negative effect that neat biodiesel has on NO_x emissions. Mofijur

et al. [43] also found that EGR can reduce the NO_x emissions when using biodiesel blends while still getting a reduction in CO, PM and HC emissions.

1.2.7 Modelling engine combustion

The modelling of internal combustion (IC) engines can be built from simple air standard cycles to complex 3D models that may include turbulence, chemical reactions and spray dynamics. Modelling IC engine combustion can be classified into three categories in the order of increasing complexity:

- 0D/1D single zone models
- Quasi-dimensional multi-zone models
- Multidimensional models

The single and multi-zone models are classified as thermodynamic models as they are used to analyse the contents of the engine cylinder during its operating cycle. The models follow the changing thermodynamic and chemical state of the working fluid through the engine's intake, compression, combustion, expansion and exhaust processes. The cylinder charge is assumed to be uniform in both composition and temperature and the first law of thermodynamics is used to calculate the mixture energy accounting for the enthalpy flux due to fuel injection. The fuel is assumed to mix instantaneously with the cylinder charge and that the whole mixture behaves like an ideal gas. In the multi-zone model, the temperature, composition, volume and all thermodynamic properties are allowed to vary from one zone to another, but within the confines of each zone they are regarded as uniform. Multidimensional models require a detailed description of the fluid flow geometry. The entire combustion chamber is divided into a number of computational zones representing the various physical regions present in the combustion chamber [61].

1.2.7.1 0D/1D single zone models

The zero-dimensional models are based on the first law of thermodynamics and mass balance equations. In the zero-dimensional model, the entire combustion chamber is taken to be a single, homogeneously mixed zone. As such, this assumption affects the model's capability to simulate wave propagation into pipes and manifolds as well as fuel spray evolution and spatial variation in mixture composition and temperature [62, 63]. When fuel is added to the cylinder through the combustion period, the only relationship it has with the injection process is that its total mass is equal to the

actual total fuel mass. As leakage through the piston rings and the mass flows into crevices are neglected, conservation of mass for the engine is:

$$\frac{dm}{dt} = \dot{m}_{intake} + \dot{m}_{fuel} - \dot{m}_{exhaust} \quad (1.2)$$

where m is the mass contained in the cylinder, \dot{m}_{intake} and $\dot{m}_{exhaust}$ are the instantaneous mass flow rates through the intake and exhaust valves, and \dot{m}_{fuel} is the rate of fuel added to the mixture. Energy conservation is applied to the single zone while accounting for the work absorbed and produced by the piston as well as the heat release due to combustion of fuel:

$$\frac{dU}{dt} = -p \frac{dV}{dt} - \dot{q}_{wall} + \sum h_j \dot{m}_j \quad (1.3)$$

where U is the internal energy of the cylinder mixture, \dot{q}_{wall} is the instantaneous heat transfer rate into the cylinder coolant and $\sum h_j \dot{m}_j$ represents the enthalpy fluxes through the intake and exhaust valves as well as the flux associated with the fuel injection. Also, conservation of momentum is not considered and spatial variations of composition, thermodynamic properties (pressure, temperature, composition, etc.) and transport properties (viscosity, thermal conductivity, diffusion coefficients) are considered negligible. The assumption of an ideally mixed combustion chamber means that the heat released during the combustion phase of the engine cycle can only be accurately modelled by empirical sub-models, such as the Woschni correlation [64], and pollutant formation rates that are highly dependent on local temperatures and mixture compositions cannot be accurately determined. Empirical models try to reproduce the characteristic heat release rates obtained from experiments by simple mathematical equations with as few parameters as possible. The Wiebe function is usually used for this purpose with rate of mass burning or heat release rate specified as a function of the crank angle.

1.2.7.2 Quasi-dimensional models

A common feature of quasi-dimensional models is the inclusion of some aspects of the physical and chemical processes in the basic thermodynamic model. In the zero dimensional model, the combustion rate (burn rate) is defined by a simple burning law (e.g. Wiebe correlation) whereas in the quasi-dimensional combustion model it is based on the phase-divided spray mixing model, and it includes break-up time calculations, air entrainment calculations, ignition delay period calculations, heat transferring calculations, thermodynamic calculations, combustion product calculations and emission calculations [65]. This enables the prediction of the

ignition delay and combustion rate as a function of engine design and operating parameters. By this approach, quasi-dimensional models, attempt to account for the interaction that exists between engine design as well as operating conditions and the combustion process without the need for prior measurement and the details and complexity that are characteristic of multi-dimensional models.

1.2.7.3 Multidimensional models

Multidimensional models are able to divide the engine cylinder space into fine grids, thus providing a considerable amount of temporal and spatial information of the flow field, temperature, composition, pressure and turbulence within the combustion chamber. Multi-dimensional models rely on sub-models to describe the turbulence, chemical kinetics and boundary layer effects and as such, they are limited by the adequacy of these sub-models. The drawback is that the computational time and storage constraints is much higher compared to single-zone models and precludes it from being used routinely in design work. Therefore, they are usually employed for modelling just the combustion chamber rather than model the full engine cycle. As such, the use of single-zone models for this research will be further investigated.

1.2.7.4 Single zone compression ignition engine models

In this project, a single zone model was developed for a compression ignition engine. Mass and energy balance equations were used for an open thermodynamic system in order to take into account the gas exchange process during the intake and the exhaust strokes. The rate of change of the total mass in any open thermodynamic system is equal to the mass flow rates into and out of the system as seen in Equation 1.2. The first law of thermodynamics for an open system which is quasi static may be written as:

$$\frac{dU}{dt} = \sum_i \dot{m}_i h_i - \dot{q}_{wall} - \dot{W} + \dot{q}_{comb} \quad (1.4)$$

where $\sum_i \dot{m}_i h_i$ is the net rate of influx and outflux enthalpy, \dot{q}_{wall} is the total heat transfer to the walls, \dot{W} is the rate at which the system does work by boundary displacement and \dot{q}_{comb} is the energy source due to the combustion process. For direct injection engines, the only mass flow across the system boundary (when intake and exhaust valves are closed) is the fuel injected into the cylinder.

$$\frac{dU}{dt} = \dot{m}_f h_f - p \frac{dV}{dt} + \frac{dq}{dt} \quad (1.5)$$

If U is taken as the internal energy of the cylinder contents and h_f as the enthalpy of the injected fuel, then dq/dt becomes the difference between heat released by combustion of the fuel and the heat transfer from the system. With $h_f \approx 0$, Equation 1.5 then becomes:

$$\frac{dq}{dt} = p \frac{dV}{dt} + \frac{dU}{dt} \quad (1.6)$$

If it is assumed that the contents of the cylinder can be modelled as an ideal gas, then

$$\frac{dU}{dt} = mc_v \frac{dT}{dt} \quad (1.7)$$

and from the ideal gas law, $pV = mRT$, with R assumed constant:

$$m \frac{dT}{dt} = \frac{1}{R} \left(p \frac{dV}{dt} + V \frac{dp}{dt} \right) \quad (1.8)$$

and thus Equation 1.7 becomes:

$$\frac{dU}{dt} = \frac{c_v}{R} \left(p \frac{dV}{dt} + V \frac{dp}{dt} \right) \quad (1.9)$$

Equation 1.6 can then be rewritten using Equation 1.9:

$$\frac{dq}{dt} = p \frac{dV}{dt} + \frac{c_v}{R} \left(p \frac{dV}{dt} + V \frac{dp}{dt} \right) \quad (1.10)$$

which can be rewritten using $c_v/R = 1/(\gamma - 1)$:

$$\frac{dq}{d\theta} = \frac{1}{\gamma - 1} \left(p\gamma \frac{dV}{d\theta} + V \frac{dp}{d\theta} \right) \quad (1.11)$$

For diesel combustion analysis, Equation 1.11 is adequate [66, 67]. Once the heat release profile is calculated from experimental cylinder pressure data using Equation 1.11, the fuel mass fraction burned can be calculated:

$$\frac{dq}{d\theta} = m_{inj} q_{LHV} \frac{dx_b}{d\theta} \quad (1.12)$$

where m_{inj} is the mass of fuel injected into the cylinder, q_{LHV} is the lower fuel heating value of the fuel and x_b is the mass fraction of fuel burned during combustion. Diesel combustion proceeds in two phases as seen in Figure 1.7, premixed combustion and mixing controlled combustion (diffusion combustion). Watson *et al.* [68] have developed a model where the fuel burning rate is expressed as the sum of two

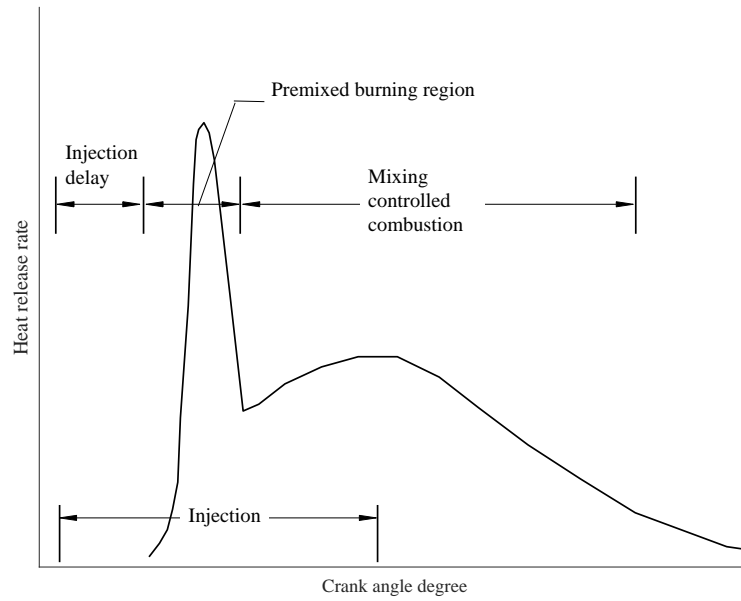


Figure 1.7: Schematic of the heat release rate in a direct injection diesel engine. Adapted from Ramos [61].

components relating to the premixed and the diffusion combustion phases. It is given by:

$$\frac{dx_b}{d\theta} = \beta \frac{dx_{bp}}{d\theta} + (1 - \beta) \frac{dx_{bd}}{d\theta} \quad (1.13)$$

where β is the weight factor expressed as the ratio between the fuel burned by premixed combustion and the total fuel burned. The subscripts p and d indicate the fuel mass fraction burned in the premixed and diffusion combustion stages, respectively. The mass fraction of burned fuel can be modelled by the Wiebe function:

$$x_b = 1 - \exp \left[-a \left(\frac{\theta - \theta_{comb}}{\Delta\theta_{comb}} \right)^{m+1} \right] \quad (1.14)$$

The rate of fuel burned, introduced in Equation 1.13, is the derivative of Equation 1.14:

$$\frac{dx_b}{d\theta} = a(m+1) \left(\frac{1}{\Delta\theta_{comb}} \right) \left(\frac{\theta - \theta_{comb}}{\Delta\theta_{comb}} \right) \exp \left[-a \left(\frac{\theta - \theta_{comb}}{\Delta\theta_{comb}} \right)^{m+1} \right] \quad (1.15)$$

where m and a are the Wiebe function tuning parameters, $\Delta\theta_{comb}$ is the duration of the energy release for the combustion event and θ_{comb} is the start of combustion crank angle degree. Equation 1.15 is applied to the premixed and diffusion combustion

phases respectively in order to solve Equation 1.13:

$$\frac{dx_{bp}}{d\theta} = a_p(m_p + 1) \left(\frac{1}{\Delta\theta_{comb p}} \right) \left(\frac{\theta - \theta_{comb p}}{\Delta\theta_{comb p}} \right) \exp \left[-a \left(\frac{\theta - \theta_{comb p}}{\Delta\theta_{comb p}} \right)^{m_p + 1} \right] \quad (1.16)$$

$$\frac{dx_{bd}}{d\theta} = a_d(m_d + 1) \left(\frac{1}{\Delta\theta_{comb d}} \right) \left(\frac{\theta - \theta_{comb d}}{\Delta\theta_{comb d}} \right) \exp \left[-a \left(\frac{\theta - \theta_{comb d}}{\Delta\theta_{comb d}} \right)^{m_d + 1} \right] \quad (1.17)$$

The method of using the above equations to solve the total fuel mass burned is known as the double Wiebe equation model.

The combustion model induces seven unknown parameters: the weight factor β , the Wiebe parameters a_p , a_d , m_p and m_d for premixed and diffusion combustion and the combustion duration of each phase $\Delta\theta_{comb p}$ and $\Delta\theta_{comb d}$ respectively. In this study, the combustion efficiency represented by a_p and a_d has been set to 6.9 which represents 99.9 % of fuel burnt at the end of combustion. An example of correlating Equation 1.16 and Equation 1.17 to calculated fuel burned mass fraction can be seen in Figure 1.8. By accurately fitting the equations to the experimental data, values for the equation parameters can be determined. Additionally, the start of combustion introduced in Equation 1.16 and Equation 1.17 needs to be modelled using the available experimental data.

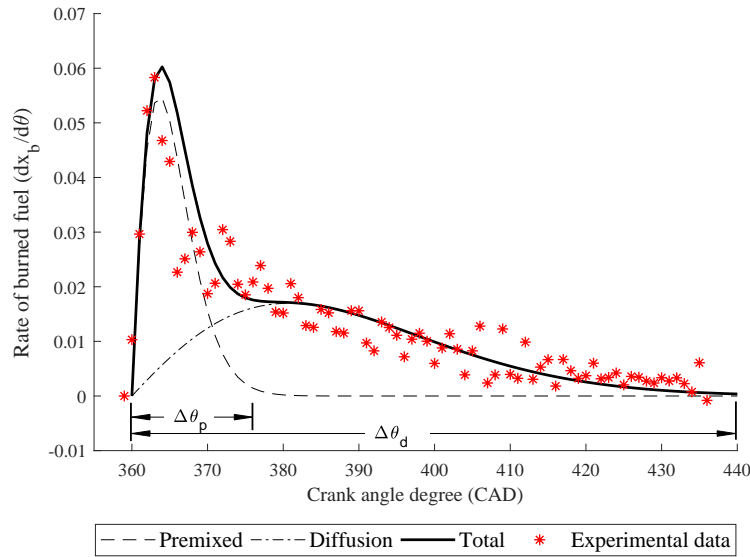


Figure 1.8: Visual representation of the double Wiebe equations from Equation 1.13 using data generated in Chapter 5.

The start of combustion required by the Wiebe correlations can be calculated

using:

$$\int_{SOI}^{SOC} \frac{1}{\tau_{ID}} dt = 1 \quad (1.18)$$

where SOI is the time of start of injection, SOC is the start of combustion and τ_{ID} is the ignition delay period. In general, τ_{ID} is a function of mixture temperature, pressure, equivalence ratio and fuel properties. In an engine cylinder, the pressure and temperature change during the delay period due to the compression stroke. Ignition delay data can be correlated by an equation in the form of:

$$\tau_{ID} = Ap^{-n} \exp\left(\frac{E_A}{RT}\right) \quad (1.19)$$

where E_A is the apparent activation energy for the fuel's autoignition process, R is the universal gas constant and A and n are constants. Watson *et al.* [68] developed a similar ignition delay model that can be correlated for diesel fuel:

$$\tau_{ID} = A^{-n} \exp\left(\frac{T_a}{T}\right) \quad (1.20)$$

where A , n and T_a are parameters that depend of the fuel used. Values for the parameters when diesel fuel is used, as suggested by Ramos [61], is T_a equal to 2100 K; n equal to 1.02 and A equal to 3.45. However, other available research suggest that these parameters have to be calibrated for each specific engine application. Maroteaux and Saad [69] found that by correlating the parameter A to experimental data, while keeping the parameters n and T_a constant, gave better results, than using the values suggested by Ramos [61]. A was chosen to be calibrated, as it is directly proportional to the ignition delay (Equation 1.20) and is easier to calibrate than n and T_a . Maroteaux and Saad [69] further concluded that using Equation 1.20, can still result in some error when predicting the ignition delay, which is a result from the variation of the charge temperature and pressure during compression. To get around this error, Maroteaux and Saad [69] expressed the ignition delay in the form of a multiple regression line. Engine operating parameters that influence ignition delay such as fuel pressure, equivalence ratio, charge inlet temperature and inlet pressure were used as parameters to construct the multiple regression equation. The error between the calculated and the experimental ignition delay was reduced from approximately 5 % to around 1 % when using a multiple regression equation compared to using Equation 1.20. Similarly, rather than using the constant values for Equation 1.20 as suggested by Ramos [61], Awad *et al.* [66] calibrated the equation's parameters A , n and T_a using experimental combustion data when investigating the use of diesel fuel and biodiesel fuel in a compression ignition engine. An error of

approximately 2 % was reported by Awad *et al.* [66] when using the modified ignition delay equation together with the Wiebe equations to calculate engine combustion data. Prasath *et al.* [70] also reported the successful use of experimental data to characterise the ignition delay and Wiebe equations to predict compression ignition engine combustion behaviour when running on diesel or biodiesel. This research will use experimental pressure data to determine the fuel mass fraction burned profile of the combustion event and create multiple Wiebe combustion equations from the data. Multiple regression models will also be used to characterise the Wiebe equation's variables. The use of regression models will enable the simulation to investigate transient engine scenarios as well as decrease computational time.

1.2.7.5 Emission models

The emission models that will be discussed in this section is the CO emissions model and the NO_x emissions model. The modelling of Particulate Matter (PM) was not considered in this research since the modelling of PM formation is complex and cannot be accurately modelled using single zone models [71].

There are two main sources of CO emissions from compression ignition engines: over mixing and under mixing of fuel with the intake charge. The case of over mixing of fuel is associated with lean combustion during the ignition delay period. The low temperatures associated with lean combustion fails to oxidise CO completely within the time scale even though there is enough oxygen present. In the case of under mixing of fuel, CO is the product of rich premixed combustion. This type of situation arises where the fuel is not mixed properly with air. The CO formed fails to mix with the available oxygen to complete combustion and result in incomplete combustion of the fuel.

Chemical equilibrium calculations can be used to describe detailed emission formation models that are based on the kinetics of various species. The equilibrium products can be calculated as outlined by Olikara and Borman [72] and Way [73]. The calculations include all the major species such as CO₂, CO, H, OH, H₂O, NO, N, N₂, O₂, O, H₂ and Ar. The use of the chemical equilibrium calculations to determine CO emissions can result in under predicting CO emissions by as much as ten times the measured value. Newhall [74] found that during the initial expansion stage of combustion, CO is destroyed at a rate corresponding to the shifting chemical equilibrium expansion, but as the process continues, an increasing deviation from equilibrium values for CO occurs. The deviation from equilibrium is a result of the reduction in pressure and temperature during expansion that retards the reaction of

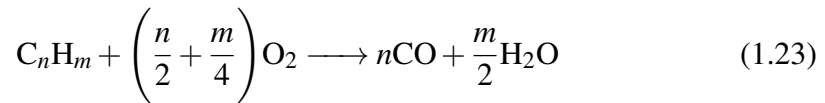
CO with the hydroxyl radical:



Newhall [74] found that throughout the expansion stroke, Equation 1.21 is continuously equilibrated. This suggests then that if Equation 1.21 is at all times in equilibrium, levels of carbon monoxide and carbon dioxide will be controlled by the existing levels of hydroxyl radicals and hydrogen atoms as well as the ratio between the two:

$$\frac{[\text{CO}]}{[\text{CO}_2]} = \frac{1}{K_{c_{12}}} \frac{[\text{H}]}{[\text{OH}]} \quad (1.22)$$

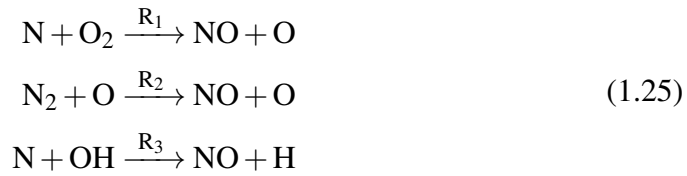
where the equilibrium rate constant $K_{c_{12}} = 7.1 \times 10^{12} \exp(-7700/RT)$. When compared to experimental results, Equation 1.22 shows good agreement in approximating CO emissions at exhaust, especially for lean fuel combustion scenarios. Predictions where the combustion is rich, suffer in accuracy when using Equation 1.22. To account for CO emissions for fuel rich combustion a two step mechanism can be used as described by Westbrook and Dryer [75]:



Bagal *et al.* [76] found good agreement between simulated and experimental CO emission results when using the two step mechanism. Improvements to the model as suggested by Bagal *et al.* [76] include the addition of the reaction kinetics between CO and the hydroxyl radicals (Equation 1.22) as mentioned by Newhall [74].

Diesel fuels release significant quantities of nitrogen based pollutants in the air when undergoing combustion. Nitrogen oxides (NO_x) comprise of nitrogen monoxide (NO) and nitrogen dioxide (NO_2). From all the NO_x emissions, NO is dominant (at high temperature engine operating conditions) and NO_2 is neglected during NO_x emissions modelling [77]. The NO emissions formation process are categorised into the prompt NO formation stage and the thermal NO formation stage. Thermal NO formation is influenced by multiple factors, such as temperature and oxygen and nitrogen concentrations in the inlet charge. Among these factors, the most important is the local temperature. The atmospheric nitrogen molecules can only be broken down at very high temperatures within the flame because high activation energies are required to split the triple bond of the nitrogen molecule. This mechanism involves a reaction between the atmospheric nitrogen and the atomic

oxygen produced in the high temperature flame regions and the subsequent reactions with the nitrogen as described by Zeldovich *et al.* [78]. The nitrogen accumulated within the combustion chamber reacts with the atomised oxygen O created due to the high combustion temperature. The products of this initial reaction are NO and unstable nitrogen which is further oxidised. For fuel rich conditions, where the concentration of OH radicals is high, an additional elementary reaction is included. Thermal NO is thus calculated using the Zeldovich mechanism below:



The concentration of thermal NO versus time is solved using an open system in which Equation 1.25 is used with the rate constants reported by Heywood [79]. The first rate constant, R_1 , is given by:

$$R_1 = A \cdot \text{ARC}_1 e^{T_a \cdot \text{AERC}_1 / T} \quad (1.26)$$

For the second and third reaction equations, the rate constants R_2 and R_3 , are given by:

$$R_{2/3} = A \cdot e^{T_a / T} \quad (1.27)$$

where A is the pre-exponential constant, ARC_1 is the user defined pre-exponent multiplier, AERC_1 is the user defined exponent multiplier, T is the burned zone temperature and T_a is the activation temperature for the reaction. The majority of research uses the extended Zeldovich mechanism to determine the thermal NO emissions formed during combustion [79–83].

The second NO formation process is the prompt nitrogen formation process which occurs much earlier in the fuel-rich regions of the flames. The rich-fuel spray core is mainly responsible for the prompt NO formation, particularly if the combustion chamber contains a sufficient amount of active radicals. The prompt NO mechanism is initiated by the rapid reactions of the hydrocarbon radicals, which arise from fuel fragmentation in a combustion process taking place in the presence of molecular nitrogen, and resulting in the dissociation of the nitrogen molecule and production of hydrogen cyanide (HCN).

Numerous hydrocarbon radicals are involved in the prompt NO formation process, but CH and CH₂ are most influential. The formation of prompt NO can be accounted for from the correlation data as reported by Fenimore [84] which gives the ratio

of prompt NO to equilibrium NO as a function of equivalence ratio. Kosmadakis *et al.* [82] successfully used the correlated data for the calculation of prompt NO together with Equation 1.25 to predict NO_x emissions and found that thermal NO is highly favoured at high temperature combustion contributing to almost 90 % of total NO emissions. Petranović *et al.* [85] also used the Zeldovich mechanism together with the correlation data from Fenimore [84] and found good agreement when comparing it to experimental NO_x emissions when using binary blends of biodiesel and petroleum diesel.

1.2.7.6 Simulation software

There are several codes available for the simulation of an engine as a 0D/1D single-zone model. For simulation packages in particular, GT-Suite and Ricardo Software will be considered for this project. The software packages are compared in Table 1.6. The Ricardo software has been chosen as the preferred simulation tool for this project

Table 1.6: Comparison between Ricardo software and GT-suite simulation packages.

Characteristic	Ricardo Software	GT-Suite
1D single-zone model	Yes - Ricardo WAVE	Yes - GT-Power
Engine performance capabilities	Yes	Yes
Emission calculations	Yes	Yes
Co-simulation capabilities	Yes	Yes
Drive cycle simulation	Yes - Ricardo IGNITE	Yes
3D CFD application	Yes - Ricardo VECTIS	No
University has a licence	Yes	No

as it fulfils all the project's requirements and has a cost benefit over GT-suite.

Ricardo software has been developed by a world leading automotive consultancy and is focussed on automotive applications. The software is ubiquitous within the automotive research and engineering sector and is used by OEMs [86] and research institutions with a plethora of peer reviewed articles [87–92] thus supporting its credibility for applications in engine performance and emissions simulation.

Ricardo WAVE and Ricardo IGNITE will be used in this project to assist in the development and optimisation of different automotive configurations. Ricardo IGNITE is a system based simulation package that can be used to focus on complete vehicle system simulation and optimisation [93]. It can simulate full duration drive cycle simulations and predict fuel consumption and emissions enabling the exploration of the impact of various technologies on overall engine emissions and

fuel consumption. IGNITE also has the capacity to conduct co-simulations with Ricardo WAVE. WAVE provides a fully integrated treatment of time-dependent fluid dynamics and thermodynamics in the form of one-dimensional calculations that enables simulations to be carried out based on intake, combustion and exhaust systems [94].

1.2.8 Summary

2020 signifies a metaphorical finish line for a majority of renewable energy targets which ultimately helps to combat climate change. A lot has been done to increase the percentage share of renewable energy as well as curbing vehicle emissions. The advancements suffer from a number of failings, which are summarised here.

1. Government efforts to introduce renewable energy into the electricity generation sectors were successful, but the transport sector is lacking behind in reaching its 2020 targets.
2. ULEV uptake by consumers are slow and cannot be relied on to assist the transport industry in reaching its 10 % renewable energy targets.
3. The removal of compression ignition engines from cities is a short term solution to improve air quality in cities. A more sustainable solution is needed to reduce engine out emissions that will assist in reaching 2050 emission targets.

Research will be done to try and better understand the combined use of biofuel together with novel combustion techniques to ultimately assist the government to reach its 2020 targets. The following sections outline how the above criticisms will be addressed in an automotive content.

1.3 Aims and Objectives

The aims and objectives of the project is listed in the following sections.

1.3.1 Aims

The aims of this project are:

- To identify an optimum ternary fuel blend for a compression ignition engine that can be used as a drop in fuel to reduce vehicle emissions of CO, CO₂ and

NO_x as well as contribute to the UK's renewable transport energy target for 2020.

- To identify the optimum Low Temperature Combustion techniques for a compression ignition engine running on a ternary fuel blend in order to minimise engine out emissions.
- To evaluate the compliance of engine out emissions with European Union (EU) law by testing the engine over the World Harmonised Light Vehicle Test Procedure (WLTP).

1.3.2 Objectives

In order to achieve the aims of the project, the following objectives will be realised:

1. Simulate the test engine on a commercially available simulation tool to aid in predicting vehicle emissions of CO and NO_x.
2. Validate the simulation tool using data obtained from the engine test cell.
3. Construct a mixture design of experiment (DoE) to characterise the influence of fuel blends of petroleum diesel, biodiesel and ethanol on the engine emissions of CO, CO₂ and NO_x.
4. Use the results from the mixture DoE to determine an optimum fuel blend that complies with the renewable energy directive (RED) of the UK as well as minimise harmful emissions.
5. Construct a design of experiment (DoE) to characterise the influence of fuel injection timing, fuel injection amount and exhaust gas recirculation percentage on the engine emissions of CO, CO₂, PM/PN and NO_x.
6. Optimise the engine operating parameters which include fuel injection timing, fuel injection amount and exhaust gas recirculation percentage to minimise harmful emissions of CO, CO₂, PM/PN and NO_x.

1.4 Thesis structure

This document is structured as follows:

Chapter 2 begins with a discussion of the epistemological and methodological

approach of the research. This is followed by a detailed discussion of the experimental equipment used as well as the approaches used to calibrate some of the measuring instruments.

This is followed by Chapters 3-5 which comprise of the simulation and experimental aspects of this research and loosely correspond to the order of the research questions in Section 1.3.2. The Chapters examine:

- **Chapter 3: Engine Simulation.** Initially, the set up of the engine model in Ricardo WAVE and vehicle model in Ricardo IGNITE are presented, with detailed discussion on the elements used and assumptions made to ensure the two models are representative of the engine test cell and complete vehicle under consideration. This is followed by discussions of how experimental data such as valve discharge coefficients were used to increase the fidelity of the model. Combustion sub model validation techniques that were developed are also presented as well as the set up of a co-simulation between the WAVE and IGNITE models.
- **Chapter 4: Optimising emissions reduction using biofuel.** Emissions reduction of a compression ignition engine using ternary blends are investigated. It is demonstrated that the use of a mixture Design of Experiment (DoE) can be used to determine the effects of ternary and binary blends between diesel, biodiesel and ethanol on engine out emissions. Following, it is demonstrated that the DoE data can be used to optimise towards a blend that achieves a renewable content of 10% as well as reduce engine out emissions compared to using pump diesel when tested over the World Harmonised Light vehicle Test Procedure.
- **Chapter 5: Emissions reduction using low temperature combustion.** The use of LTC strategies to reduce engine out emissions while running with a ternary blend are investigated. It is demonstrated that the use of a Response Surface Method (RSM) DoE together with an engine model can be used to optimise multiple LTC strategies to ultimately reduce compression ignition engine emissions running on ternary blends of biofuels and petroleum diesel. The validation of the co-simulation used together with the RSM using experimental engine data is also presented.

The document closes with Chapter 6, which contains a summary of the contribution of this research, its limitations and scope for further work.

Chapter 2

Experimental Setup

This chapter contributes to the set up and calibration of all experimental measuring equipment installed on the engine test cell at the University of the West of England. In doing so, it is demonstrated that it is possible to use the engine and dynamometer set up to generate reliable experimental data that can be used to validate simulations and help to achieve the objectives of this study.

Initially the characteristics of the engine and measuring equipment are discussed, after which the calibration process is investigated for each measuring device.

2.1 Introduction

As researchers we are pushing the boundary of knowledge, adding to it through research. According to Feldman [95] sources of knowledge can come from our perception of things, the reasoning or rational insight as to why certain things happen or even from other's testimonies. Yet, there are still questions such as:

- How does a person know something to be true.
- Under what conditions can a belief be justified.

Three paradigms exist in the epistemological field that are used to try and answer these questions:

- **Positivism:** supports the idea that natural science methods can be used to study our social reality. Sensory information through observation and measurement are sources of dependable knowledge.
- **Realism:** states that our social reality could be understood through natural science methods, but it is not assumed to be objective due to the observer's bias.
- **Interpretivism:** is opposite to Positivism and states that people create and maintain their own social world. Scientists need to gain access to people's common sense to understand their point of view.
- **Post-positivism:** adapted from the Positivist framework and states that observations cannot be relied upon and experiments have to be critically evaluated through multiple, different methods of inquiry to minimise possible errors.

This research will follow a post-positivist epistemological framework, where an understanding of the research questions can be based on multiple, different experimentations and their respective observations. The knowledge gained from the experimentation will be a product of the researcher's experience through rational deduction [96]. Also, a quantitative research methodology will be used in the proposed research. The majority of the research will be done through experimentation. The experimental works cover both steady and transient scenarios on a compression ignition engine. Experimental data will be collected from the university's engine test bench. All equipment used in the experimentations are listed in Table 2.1. The calibration and set-up of all the equipment in Table 2.1 will be explained in more detail in the following sections.

Table 2.1: Equipment used in experimental runs.

Engine test cell equipment	
Engine	2008 Ford Puma (H9FB)
Dynamometer	Froude F0271
MAF	Factory fitted
ECU	Typhoon after-market
Pressure transducer	Kistler 6056A
Charge amplifier	Kistler 5018
Data Acquisition	Picoscope 4224
Gas analysers	
NO, NO ₂ , CO ₂	NOVA 7466K
CO	TESTO 350
PM, PN	Pegasor M-sensor

2.2 Test fuels

The test fuels used in this project were B0 reference diesel, rapeseed methyl ester biodiesel (RME) and ethanol. B0 diesel was chosen as a reference fuel and benchmarked throughout the project. As pump diesel has biodiesel present in the fuel blend, it is necessary to use B0 diesel to make it possible to accurately control the percentage of biodiesel present in the blends used during testing. The fuel supplier provided physiochemical properties for the diesel fuel, RME and ethanol, respectively. The fuel properties of each fuel can be seen in Table 2.2.

Table 2.2: Main fuel properties of neat test fuels.

	Diesel	Biodiesel	Ethanol
Cetane number	51.7	52.8	7.0
LHV (MJ/kg)	42.8	38.0	26.8
Density at 15 °C (kg/m ³)	831.1	883.2	790.0
Viscosity at 40 °C (mm ³ /s)	2.686	4.372	1.200
Oxygen content (%)	0	10.8	34.8
CFPP (°C)	-26	-6	-38
Flash point (°C)	65	179	20

Table 2.3: Engine set up for experimentation.

Description	Data
Power (kW)	100
Peak torque (Nm)	475
Displacement (cc)	2400
Bore (mm)	89.9
Stroke (mm)	94.6
Cylinders	4
Euro standard	Euro 4
Injection system	Common rail
Aspiration	Turbocharged
Firing order	1-3-4-2
Compression ratio (CR)	17.5

2.3 Engine test bench

The experimental work was performed on a 2008 Ford Puma four stroke compression ignition engine with a high pressure common rail fuel system. The engine is water-cooled, has a direct injection fuel delivery system and is equipped with a variable geometry turbine (VGT) turbocharger and an exhaust gas recirculation (EGR) system. Although the research is being conducted on a Euro 4 engine, which was manufactured in 2008, this research is still highly relevant to the current UK fleet. According to the Department for Transport's statistics [97] approximately 14 % of the current diesel fleet is of this engine type. Additionally the conclusions for this paper are qualitatively relevant to more modern Euro 5 and Euro 6 diesel engines [98–101].

The main engine specifications are summarised in Table 2.3. The engine has a rated power output of 100 kW with a maximum torque level of 475 Nm between 2000 rpm and 2500 rpm. The engine is connected to a water-brake dynamometer model Froude F0271 to control the torque and speed of the engine. Figure 2.1 shows a photograph of the engine set up used in this study. The engine is controlled from a separate control room for safety purposes. A picture of the control room is shown in Figure 2.2. A NOVA 7466K gas analyser and a TESTO 350 gas analyser are connected to the exhaust gas pipe to measure CO, CO₂ and NO_x emissions. In the analysers, the NO_x was measured with a electrochemical sensor, CO with a non-dispersive infra-red sensor (NDIR) and CO₂ with a electrochemical sensor (TESTO) and NDIR (NOVA). A Pegasor M-sensor particle counter was used to

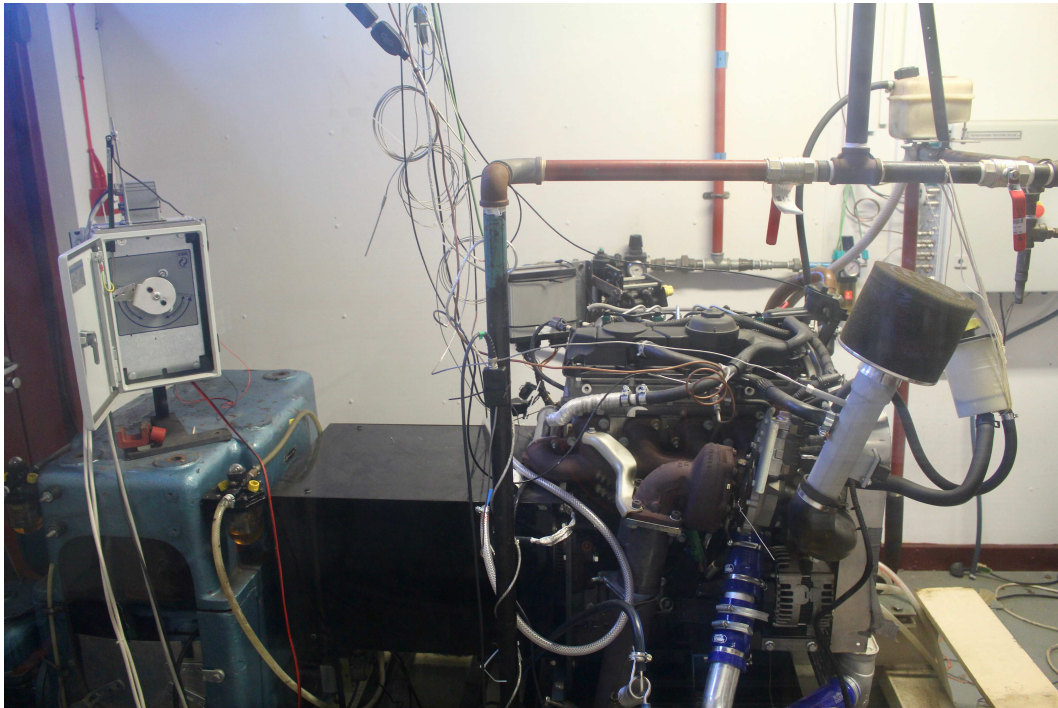


Figure 2.1: UWE engine test cell set up.

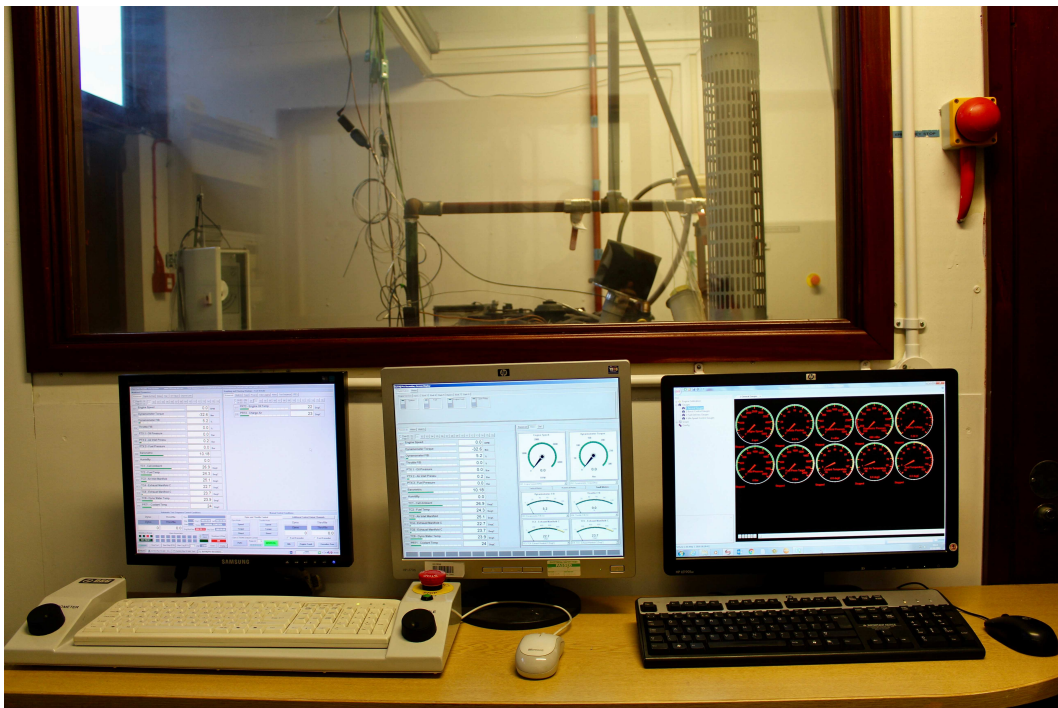


Figure 2.2: Engine test cell control room.

count the particle numbers in real time using electrical detection of aerosol following the *escaping current* technique. To record engine operation several pressure sensors and thermocouples were attached to the test bench. For detailed combustion analysis

a Kistler pressure transducer 6056A was mounted in cylinder 4 to record the in-cylinder pressure. A factory fitted hall effect sensor was mounted at the flywheel to provide crank-angle based timing information for the pressure transducer. From the pressure and crank angle data the heat release profile and combustion duration were derived. The pressure sensor signal was converted from an electrical charge into a proportional voltage signal and amplified through a Kistler 5018 charge amplifier and recorded through a high-speed Picoscope oscilloscope 4224. The DaTAQ Pro control software was used to control engine speed and torque as well as record engine operation conditions. The schematic of the engine set up is illustrated in Figure 2.3.

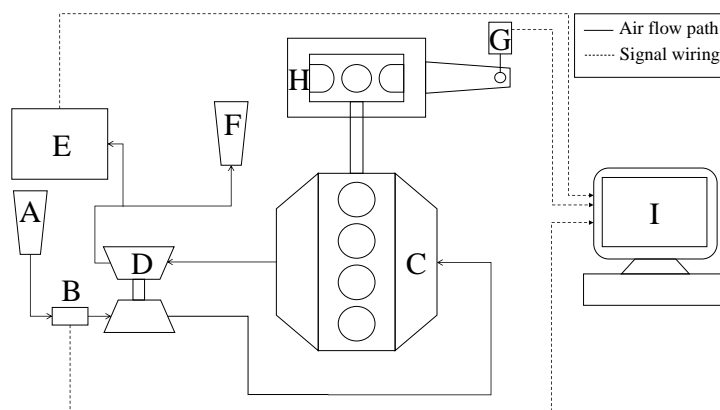


Figure 2.3: Layout of the UWE engine test cell together with measuring equipment. A: air filter; B: mass airflow sensor; C: engine; D: turbocharger; E: gas analyser; F: exhaust outlet; G: load cell; H: dynamometer; I: Data acquisition system.

2.3.1 Engine and dynamometer control software

To achieve reliable engine testing results an engine test bed with a sophisticated control software is essential. The engine and dynamometer are connected via an ordinary shaft consisting of a round bar with flanges on each side. The shaft has no significant friction and other transmission losses. The dynamometer was not just used to measure speed and torque of the engine, but also to simulate the driving environment if the engine was installed in a powertrain system. This means that all these components needed to be controlled by the dynamometer control software:

- Fuel delivery system
- Cooling and combustion air flow including temperature control for water and oil
- Throttle control

- Engine electrical system
- Engine starting system

The software, which controlled the dynamometer, was DaTAQ Pro supplied by DSG. DaTAQ Pro supports up to 512 input channels, being a mix of low and high speed analogue inputs, such as thermocouples, pressure sensors, speed and torque inputs. The test bed was operated with an electronic throttle control, whereby a voltage signal between 0 V and 5 V was sent from the throttle pedal to the ECU. The control software allowed several control settings. Most commonly the throttle and dynamometer controls were set to control engine speed and engine torque feedback parameters. Most of the time, however, the throttle was set to speed-mode (rpm) and the dynamometer to torque-mode (Nm). In this mode, the user is able to change torque without affecting the speed and vice versa. Furthermore the user has the opportunity to create a test plan for the engine by setting conditions, such as ramp time, settling time and step duration at specific engine conditions. Up to 400 test points can be set and then the dynamometer operates through the test plan automatically to ensure repeatable test conditions without major external influences. For each test the user can record the engine conditions over a period of time or in interval sequences and calculate the average values for each condition.

2.3.2 ECU control software

The engine is controlled by a TYPHOON engine control unit (ECU). The ECU has a 32 bit Motorola main processor that provides the processing power. The ECU's configurable injector outputs make it possible to drive the engine with fully sequential fuelling. Other configurable settings include:

- Boost control.
- Fuel pressure control.
- Pilot and main injection timing maps.
- Pilot and main injection duration maps.
- EGR control.

The engine control unit (ECU) is accessible through the CAN bus and can be connected via USB to any computer or laptop. The engine operating maps can be configured using the calibration software SXTune provided by Specialist Control Systems Ltd. All engine maps are a function of engine speed (rpm) and throttle position (%).

2.3.3 Test bench fuel system

Since different blends were tested on the engine it was important to develop a procedure for switching fuel blends to ensure that the system was drained and flushed sufficiently with the next fuel blend to ensure no contamination of different fuels took place. The schematic diagram of the fuel system is illustrated in Figure 2.4. The engine is equipped with a high-pressure common rail fuel injection system. With

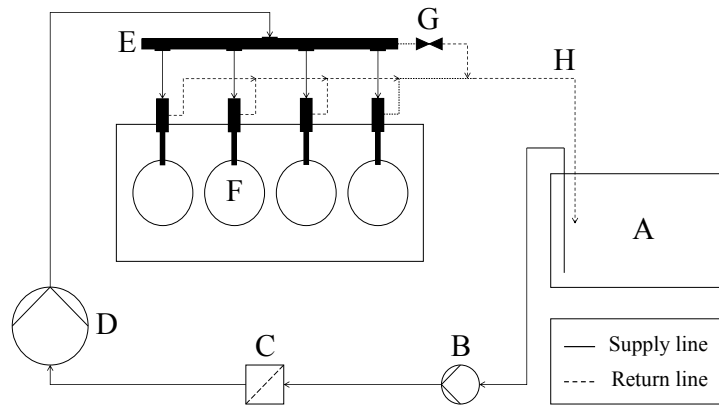


Figure 2.4: Layout of the engine test cell's fuel system. A: fuel tank; B: transfer pump; C: fuel filter; D: high-pressure fuel pump; E: common fuel rail; F: fuel injector; G: fuel overpressure safety valve; H: fuel return line.

this fuel injection process, a high-pressure fuel pump delivers a uniform level of pressure to a shared fuel rail (also known as a common rail), which serves all 4 fuel injectors. Pressure is controlled up to a pressure of 1600 bar. The system supports a pre-injection (pilot) phase. Fuel injection pressure is generated independently of engine speed and fuel injection events. The fuel injection timing and volume are calculated by the Engine Control Unit (ECU), which then energises the appropriate solenoid actuated injector. The fuel system is divided into 2 sub systems: low-pressure system and high-pressure system. The low pressure system features the following components:

- Transfer pump
- Fuel filter

The high pressure system features the following components:

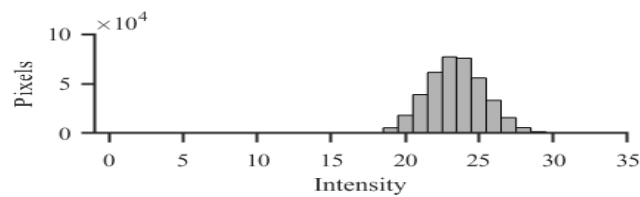
- High-pressure fuel pump
- Fuel rail
- High-pressure fuel pipes

- Injectors

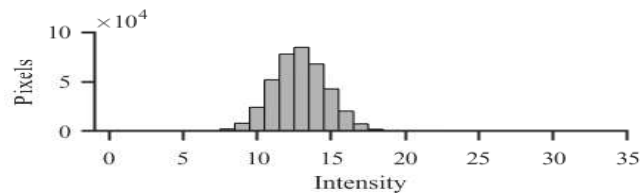
The transfer pump draws the fuel from the fuel tank, through the fuel filter, and then pumps the fuel to the high pressure pump. The transfer pump maintains a constant fuel pressure through a regulating valve within the fuel pump. The high pressure pump pressurizes the fuel and then transfers it to the common rail. Fuel leaking from the injectors and/or returning fuel from the high-pressure pump are fed back to the fuel tank. A 5 L tank provided sufficient fuel for a complete test sequence. A new fuel filter for each fuel type was used to reduce the degree of contamination in the system. In order to ensure that the old fuel blend from the previous test, in the fuel system does not influence the next test, the fuel system was flushed with the next test's blend of fuel before formal testing began. It was necessary to determine the amount of flushes required that will successfully remove all remaining fuel blend from the previous test. This was done using red fuel dye. The following procedure was followed using the engine's fuel delivery system (Figure 2.4):

- Step 1: Run engine with fuel which contains the red dye.
- Step 2: Use fuel transfer pump to pump out all fuel from the fuel system.
- Step 3: Replace current fuel filter with an empty fuel filter.
- Step 4: Replace fuel in the fuel tank with clean fuel and run the fuel transfer pump for 5 minutes.
- Step 5: Idle engine for 5 minutes.
- Step 6: Run engine at 2500 rpm for one minute.
- Step 7: Use fuel transfer pump to pump out all the fuel from the fuel system.
- Step 8: Repeat steps 4-7.

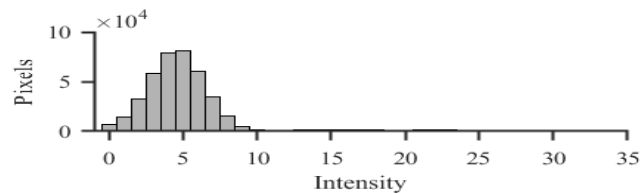
A sample of the fuel in the fuel tank was taken after each flush iteration. The samples were photographed with a Canon EOS 700D under homogeneous light conditions. The red spectrum of each sample was calculated using Matlab. The red spectrum of the clean fuel was subtracted from the other sample's spectrum to eliminate any red colours that were already present in the clean fuel. After the fourth flush, more than 95 % of the pixels examined exhibited a red intensity of less than 5 (Figure 2.5). It was determined that flushing the fuel system four times following the developed procedure would eliminate significant contamination between different fuel blends.



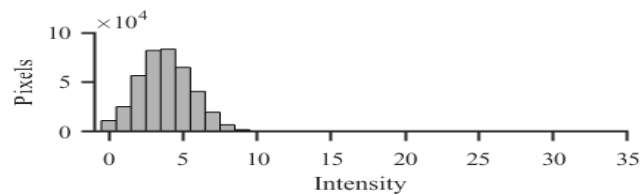
(a) Red spectrum of fuel with red dye added.



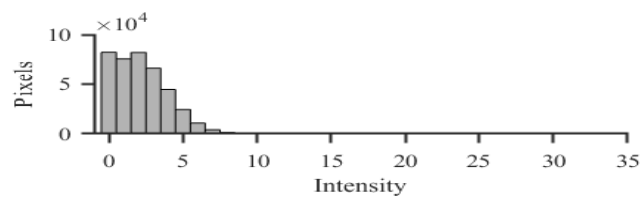
(b) Red spectrum of fuel after the first flush.



(c) Red spectrum of fuel after the second flush.



(d) Red spectrum of fuel after the third flush.



(e) Red spectrum of fuel after the fourth flush.

Figure 2.5: Change in red spectrum for the fuel samples taken after each fuel system flush [41].

2.3.4 Test bench exhaust system

For exhaust gas measurements, ports were added to the exhaust system to connect the exhaust analysers, which are explained in detail below. The main measured emissions were CO, CO₂, NO_x, particle mass and particle number. Three engine emission analysers were used in measuring different exhaust gasses (Figure 2.6):

- NOVA gas analyser: CO₂, NO and NO₂.

- TESTO gas analyser: CO.
- Pegasor M-sensor: Particle number and particle mass.



(a) NOVA 7466K gas analyser.



(b) TESTO 350 gas analyser.



(c) Pegasor M-sensor particle mass and particle number sensor.

Figure 2.6: Gas analysers used for engine exhaust measurement.

2.3.4.1 NOVA gas analyser

The NOVA model 7466K gas analyser was used to measure CO_2 , NO and NO_2 in the engine exhaust (Table 2.4). The analyser was calibrated by the manufacturer before any testing began. CO_2 is detected by a single non-dispersive infra-red detector. An infra-red beam is pulsed intermittently through a sample tube through which sample

Table 2.4: Method and accuracy of the NOVA 7466K used to measure engine emissions.

Exhaust gas	Range	Accuracy	Method
CO ₂ (%)	0 – 20	±0.2	infra-red
NO (ppm)	0 – 2000	±20	electrochemical
NO ₂ (ppm)	0 – 800	±8	electrochemical

gas is flowing. A detector at the other end of the tube senses the amount of infra-red falling upon it. An optical filter is also placed in the infra-red beam. This optical filter only allows the 4.3 μm wavelength that CO₂ gases absorb to pass through it. The grade of absorption of these wavelengths are proportionate to the gas concentration at constant pressure. Sample gas needs to be dried prior to entering the sensor, as water in the exhaust absorbs infra-red easily. If there is no CO₂ in the sample gas, all of the infra-red energy in these wavelengths will reach the detector. As the levels of CO₂ in the sample gas increase, they begin to absorb some of the infra-red energy in these wavelength so that less energy reaches the detector. A digital 4-20 mA output signal is generated to be read by computer software.

NO and NO₂ are detected by an electrochemical sensor. Electrochemical sensors are devices that measure gas constituents through the principle of ion selective potentiometry. The sensor contain a electrolytic matrix that is designed for a specific gas to be detected. Two or three electrodes (gas specific) are placed in this matrix and an electrical field is applied. Exhaust gas enters the sensor and chemically reacts through oxidation or reduction on the electrode releasing electrically charged particles (ions). This reaction causes the potential of the electrode to rise or fall with respect to the counter electrode. With a resistor connected across the electrodes, a current is generated which is proportional to the concentration of gas present. The current is then amplified and a digital 4-20 mA output signal is generated to be read by computer software. The gas analyser output signal of 4 mA to 20 mA needed to be converted to a 0 V to 5 V reading in order to be read by a data acquisition system. The conversion from 4 mA to 20 mA to 0 V to 5 V was calibrated using 10 readings from the engine (Table 2.5). Each reading was recorded for one minute at steady state conditions and the average volt reading was taken together with the corresponding reading on the gas analyser display. The recorded voltage points were plotted together with the corresponding exhaust gas reading from the gas analyser. Linear regression was conducted on the data in order to get an equation for each exhaust gas in the form of:

$$\hat{Y} = b_0 + b_1X \quad (2.1)$$

The measured exhaust gas's coefficient b_0 and b_1 together with each regression line's

confidence interval are listed in Table 2.6. The confidence intervals for all the gasses are high and the equations used to calculate the gas content from the input voltage are acceptable.

Table 2.5: Recorded points from gas analyser screen.

	CO ₂ (%)	NO (ppm)	NO ₂ (ppm)
Point 1	5.4	226	28
Point 2	5.8	131	28
Point 3	5.8	131	28
Point 4	7.7	191	20
Point 5	7.6	188	20
Point 6	6.4	247	23
Point 7	8.3	291	15
Point 8	8.3	313	15
Point 9	6.9	623	31
Point 10	6.8	624	30

2.3.4.2 TESTO 350 gas analyser

The TESTO 350 is an exhaust gas measuring system in which the gas is directly sampled out of the main stream and the concentration continuously measured (Table 2.7). The analyser was calibrated by the manufacturer before any testing began. CO, NO and NO₂ are measured with the use of an electrochemical sensor. CO₂ is measured using an NDIR sensor.

2.3.4.3 Pegasor M-sensor

The Pegasor Particle Sensor (PPS-M) is based on the electrical detection of aerosol following the *escaping current* technique, which was first described by Lehtimäki [102]. A sample of the exhaust gas is charged by a corona-ionized flow as it is being pumped by an ejector type diluter inside the Pegasor sensor. While the majority

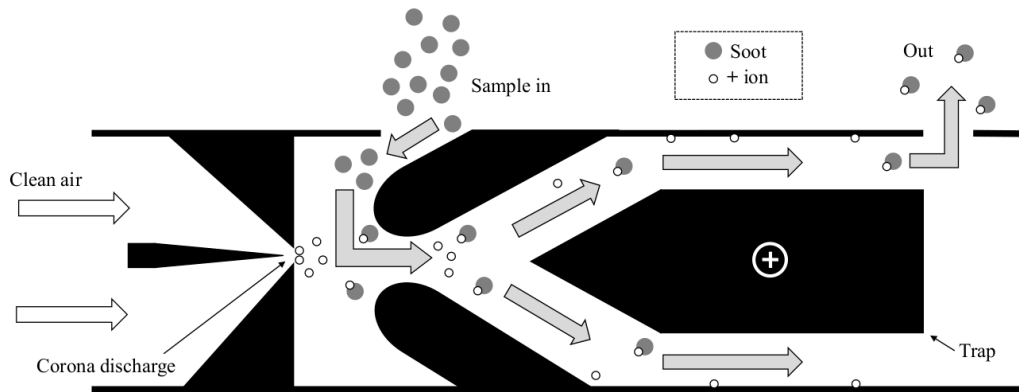
Table 2.6: Gas analyser linear regression line constants and confidence interval

Exhaust gas	b_0	b_1	R^2	P-value
CO ₂	0.222	4.851	98.01%	<0.02
NO	64.9	476.2	95.78%	<0.02
NO ₂	3.50	148.9	85.10%	<0.02

Table 2.7: Method and accuracy of the TESTO 350 used to measure engine emissions.

Exhaust gas	Range	Accuracy	Method
CO (ppm)	0 – 2000	±10	electrochemical
CO ₂ (%)	0 – 50	±0.3	infra-red
NO (ppm)	0 – 4000	±100	electrochemical
NO ₂ (ppm)	0 – 500	±5	electrochemical

of the corona ions return to the grounded sensor's body due to their high electrical mobility, a small quantity is lost with the charged particles exiting the sensor. This *lost current* is a measurement of the particle concentration in the exhaust gas. The Pegasor M-sensor working principle is shown graphically in Figure 2.7. The Pegasor

**Figure 2.7:** Visual representation of the working principle of the Pegasor M-sensor.

M-sensor has the following benefits compared to other particle number measuring equipment:

- Is a non-collective, flow through device.
- Can work continuously without maintenance for extended periods of time.
- Can measure raw exhaust without external dilution.
- Has no consumables.

The conversion of the voltage trap signal inside the Pegasor M-sensor to particle concentration is based on the introduction of L and N coefficients for mass and number respectively. The calibration coefficients provide the number and mass concentration of exhaust aerosol, when directly multiplied with the signal of the Pegasor M-sensor. The mass and number calculations are thus $Mass = L \times PPS$

and $Number = N \times PPS$ respectively where PPS is the Pegasor M-sensor trap signal in fico Amphere. The particle mass is measured in mg/m^3 and particle number is measured in $1/cm^3$. The values of L and N are calculated as a function of the sample flow rate:

$$L = \frac{6.3 \times 10^{-5}}{Q_{in}} \quad (2.2)$$

and

$$N = \frac{288}{Q_{in}} \quad (2.3)$$

The sample flow rate, Q_{in} is expressed in litres per minute at atmospheric conditions and should be determined when the sensor is at its normal operating temperature of $200\text{ }^{\circ}\text{C}$ [103]. The Pegasor M-sensor was calibrated by the manufacturer prior to the commencement of testing. The sample flow rate was set as per the measurements done by the manufacturer's calibration tests. It is necessary to use a restrictor plate with the Pegasor M-sensor to further increase the internal dilution rate, as the particulate mass and particulate number concentrations at cold start for raw exhaust is very high. The sensor's software needs to be updated with the new sample flow rate, which have decreased due to the restrictor plate. A Sensirion mass flow sensor was used to measure the new sample flow rate when the inlet flow restrictor is installed. The mass flow sensor's accuracy was first tested by measuring a known value of 5.59 ± 0.28 lpm. The recorded mass flow was 5.91 ± 0.06 lpm which falls inside the error margin of the known flow rate. The updated value for Q_{in} for Equation 2.2 and Equation 2.3 when using the inlet flow restrictor was measured at 2.25 ± 0.02 lpm.

2.3.4.4 Mass airflow sensor

The airflow into the engine is measured using a hot wire mass air flow sensor (MAF). When air flows past the wire, the wire cools, decreasing its resistance, which in turn allows more current to flow through the circuit, since the supply voltage is a constant. As more current flows, the wire's temperature increases until the resistance reaches equilibrium again. The MAF's control circuit measures current flow and generates an output signal which is proportional to the mass flow of the air. A factory fitted MAF, calibrated with a Superflow SF-120 flow bench, was used to measure the intake mass air flow. A housing was manufactured for the sensor to enable it to fit on the current engine assembly. The calibration process consisted of running the flow bench at different flow rates (in L/s) and recording the output signal from the MAF. The output signal (in Hertz) is plotted against the flow rates and a regression line is

fitted to the data. The flow rates are converted to kilograms per second using:

$$\dot{m}_{air} = \frac{\rho_{air} Q_{air}}{1000} \quad (2.4)$$

where Q_{air} is the flow of air in L/s and ρ_{air} is the density of air in kg/m³ at a given temperature when the measurement was taken. All recorded data of the flow bench is found in Appendix A. An exponential equation was fitted to the measured data to describe the data accurately with the use of the least square method:

$$\dot{m}_{air} = 1.26421 \times 10^{-14} Hz^{3.19206} \quad (2.5)$$

Equation 2.5 resulted in a goodness of fit of $R^2 = 99.6\%$ (Figure 2.8) indicating a high correlation between the measured data and the predicted data calculated by the fitted equation. The inlet air mass flow together with the fuel injected into the

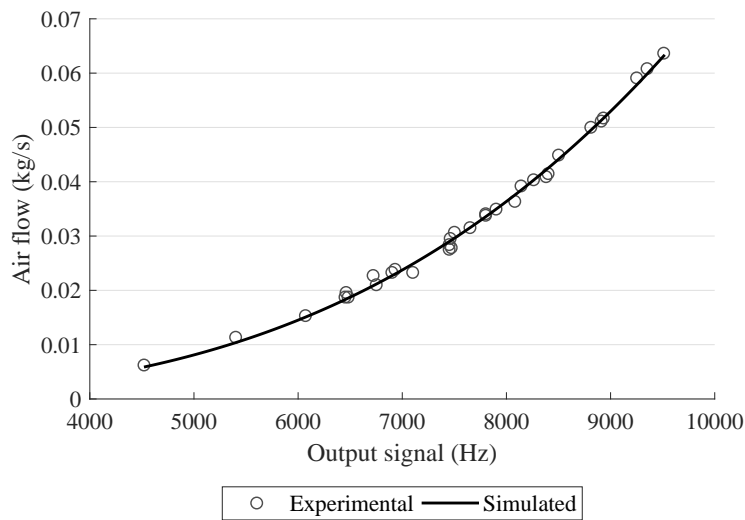


Figure 2.8: Calibration of MAF output signals.

cylinders can be added together to calculate the total exhaust flow:

$$\dot{m}_{exhaust} = \dot{m}_{air} + \dot{m}_{fuel} \quad (2.6)$$

The fuel flow, \dot{m}_{fuel} are taken from the ECU maps. The use of the values given by the ECU is acceptable as the fuel flow only accounts for a small fraction of the total exhaust flow [104].

2.3.5 Combustion analysis

In-cylinder pressure based combustion analysis is a common tool in modern engine research since this method is reliable and robust. The core part of this method is a piezoelectric pressure transducer, which can measure the in-cylinder pressure at high frequencies and is also accurate over long periods of time. Quartz has a very good piezoelectric behaviour and the electrical charge is proportional to the force acting on the crystal. The combustion analysis using a piezoelectric pressure transducer also requires a charge amplifier, a data acquisition device and a crank angle encoder. In this research a Kistler 6056A pressure transducer was used. The measuring range went up to 250 bar with a natural frequency of approximately 160 kHz. The sensor has a sensitivity of 20.56 pC/bar as well as a shock resistance of 2000 g maximum. The small voltage output signal has to be magnified and conditioned before it is used. This was done by the Kistler 5018 charge amplifier, which also compensated dynamic drifts of the sensor signal. The output signal of the amplifier was -10 V to 10 V. The Kistler 5018 was calibrated by the manufacturer prior to use. To reference the pressure signal an external sensor in terms of crank angle degrees was used. In engine research it is common practice to use an angle based reference instead of a time reference, since changes in engine speed will not be affected by the angle location. The hall effect crank angle sensor being used by the ECU was used in this project. The amplifier voltage signal and the crank angle signal were connected to a Picoscope oscilloscope 4224. The card offered up to 4 channel inputs with 32 MS buffer memory on a 12-bit resolution. Picoscope software was used to acquire the readings from the charge amplifier and the hall effect sensor. The number of cylinder pressure cycles recorded were a minimum of 100.

The health of the pressure transducer signal was analysed using the method described by Lancaster *et al.* [105]. In order to ensure that the signal from the pressure transducer is accurate, qualitative checks can be done on motored and fired data obtained from the engine. For motored pressure traces, the complications of inhomogeneities, heat transfer rates and other combustion introduced quantities are absent. The motored data exhibit little cycle-to-cycle variability and can yield valuable information about the accuracy and reliability of the entire test set up and measuring devices. Motored data was recorded while cranking the engine. Figure 2.9 shows the compression-expansion process of the motored data compared to simulated data. The correlation between the two data sets are acceptable, with a difference of about 3% between the measured and simulated values. The difference can be contributed to the inaccuracies of the heat exchange calculations between the air and the engine block. The phasing of the pressure with respect to cylinder volume can

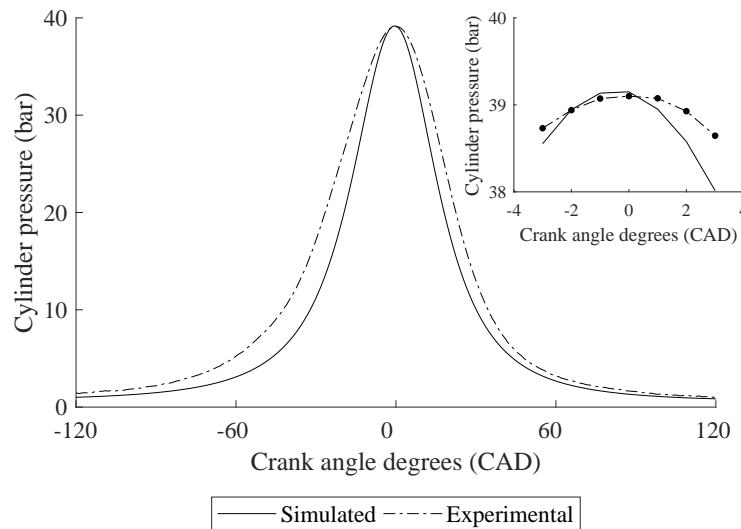


Figure 2.9: Simulated and measured cylinder pressure for motored engine.

also be checked by looking at the motored cylinder pressure near the region of peak pressure. A section of the peak pressure for the motored pressure trace is shown in Figure 2.9. As per Lancaster *et al.* [105] the peak pressure should not be more than 2 degrees before TDC which can indicate that the pressure data is advanced with respect to volume. As seen in Figure 2.9, peak pressure is reached at TDC and the pressure data from the pressure transducer is correctly phased with respect to cylinder volume.

Figure 2.10 shows cylinder pressure data when the engine is running at 3000 rpm and 75 % load. A visual check confirms that the graph is as expected [105]. The compression curve in Figure 2.10, on a logarithmic scale, is straight and has a reasonable slope, with the pumping curve properly orientated. The expansion line is also straight and does not curve as it nears maximum volume.

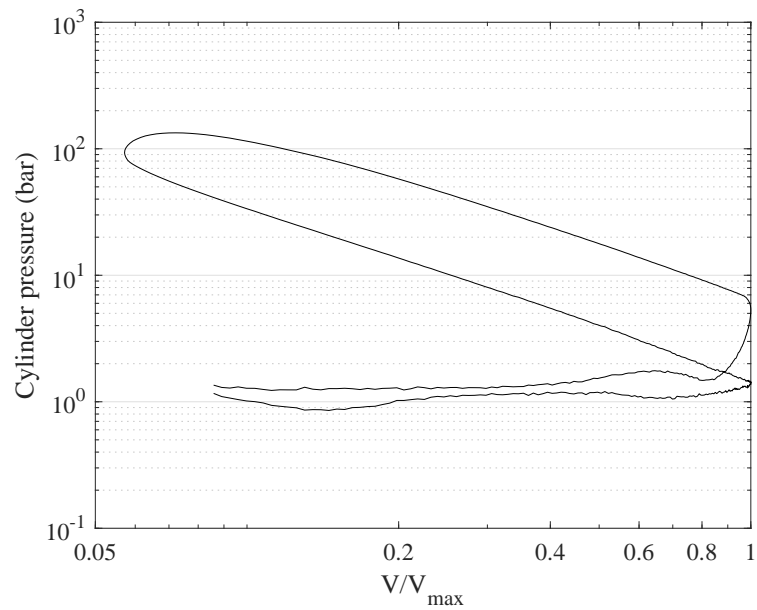


Figure 2.10: Log p-log V diagram at 75% load at 3000 rpm .

2.4 Closing remarks

The test fuels and test engine set up has been discussed. All equipment that will be used to generate experimental data for this project has been explained and where necessary, the calibration of the equipment has been discussed. As was mentioned at the beginning of this chapter, this research follows a post-positivist epistemological framework. Multiple, different experimentations will be conducted and observations on the results generated from these experiments will be used to further our understanding in the field of biofuel use and low temperature combustion. It is thus crucial that all measuring equipment is accurate and true when observations are made. All measuring equipment used in this research is accurate and all calibration techniques were followed correctly.

Chapter 3

Engine Simulation

This chapter contributes to the development of a high fidelity, 1D single zone engine simulation of the engine test cell at the University of the West of England as well as a system-based simulation to enable investigations over legislative drive cycles. In doing so, it is demonstrated that it is possible to build a comprehensive simulation that can be used effectively to investigate a vehicle's engine characteristics over drive cycles such as the WLTP and the RDE. The simulation was validated with the use of engine dynamometer data.

Initially the construction of the engine simulation as well as the system-based simulation is discussed, after which the validation process of each simulation is investigated.

3.1 Introduction

As mentioned in Section 1.2, the 1D single zone gas dynamics simulation codes are used to simulate engine performance. Compared to multi-zone models and 3D CFD models, single zone models provide a good balance between prediction accuracy and computation intensity. The Ricardo software has been chosen as the preferred simulation tool for this project. Ricardo WAVE and Ricardo IGNITE will be used in this project to assist in the development and optimisation of different automotive configurations. Ricardo WAVE provides a fully integrated treatment of time-dependent fluid dynamics and thermodynamics in the form of one-dimensional calculations that enables simulations to be carried out based on intake, combustion and exhaust systems [94]. Ricardo IGNITE is a system-based simulation package that can be used to focus on complete vehicle system simulation and optimisation [93]. It can simulate full duration drive cycle simulations and predict fuel consumption and emissions enabling the exploration of the impact of various technologies on overall engine emissions and fuel consumption. Ricardo IGNITE also has the capacity to conduct co-simulations with Ricardo WAVE. The following sections discuss how the different simulations are configured to successfully simulate the engine test cell used in this research.

3.2 Ricardo WAVE simulation development

Figure 3.1 shows a screen shot of the simulation in Ricardo WAVE. Table A.1 in Appendix A lists explanations for all the elements used in the Ricardo WAVE model. Access to the engine operating maps on the ECU is possible and it was used in Ricardo WAVE to configure the engine simulation. All ECU map values are listed in Appendix A. Map values are a function of throttle position (TPS) and engine speed (rpm). A mapless compressor was used to simulate boost as per the targets set out in the ECU data as detailed turbocharger and compressor maps were unavailable. Multi-pulse injectors were used to deliver the fuel to the engine. A pilot injection as well as a main injection were simulated. The exhaust gas recirculation (EGR) system was replicated using an orifice with variable diameter to control the percentage of exhaust gas being recirculated. Ricardo WAVE's emission sub-models were activated to enable calculations for CO emissions and NO_x emissions.

Table 3.1: Characteristics of the engine.

Description	Data
Bore (mm)	89.9
Stroke (mm)	94.6
Connecting rod length (mm)	106
Piston pin offset (mm)	0
Clearance height (mm)	5.7
Compression ratio (CR)	17.5
Number of cylinders	4
Firing order	1-3-4-2
IVO (CAD)	2° aTDC
IVC (CAD)	40° aBDC
EVO (CAD)	24° bBDC
EVC (CAD)	15° aTDC

3.2.1 Geometric data

Geometric data was first collected for the engine. This includes the dimensions of all the intake and exhaust systems, including the ports. Access to a second engine identical to the test engine made it possible to inspect parts such as the inlet manifold, exhaust manifold and EGR valve. Inlet and exhaust pipes are easily disassembled to measure wall thickness and inside diameters. All the necessary data was entered into the the pipe elements making up the pipes and manifolds of the model as seen in Figure 3.1.

3.2.2 Engine data

Table 3.1 lists all the engine data used in the simulation. Other engine data include

- Inlet and exhaust valve dimensions
- Valve lift profiles
- Valve flow coefficients
- Fuel mass injected

It is also necessary to model active PID controllers for accurate EGR percentage and boost control.

3.2.2.1 Valve characteristics

The lift profiles of the intake and exhaust valves were measured using the engine that was available. Table 3.1 shows the opening and closing times of the intake and exhaust valves in crank angle degrees (CAD). The maximum lift for both the intake and exhaust valves is 5 mm.

The flow restriction caused by the valve and valve port together, is usually the most important flow restriction in the intake and exhaust system of IC engines [79]. In order to describe real gas flow effects through the inlet and exhaust systems of the engine, it is necessary to determine the discharge coefficient (C_D) experimentally. The discharge coefficient can be calculated with the use of experimental flow measurements:

$$\dot{m} = \frac{C_D A_R p_0}{(RT_0)^{1/2}} \left(\frac{p_T}{p_0} \right)^{1/\gamma} \left\{ \frac{2\gamma}{\gamma-1} \left[1 - \left(\frac{p_T}{p_0} \right)^{(\gamma-1)/\gamma} \right] \right\}^{1/2} \quad (3.1)$$

where p_0 and T_0 are the stagnation pressure and temperature, p_T is the static pressure just downstream of the flow restriction and A_R is the reference area. R is the gas constant and γ is the heat capacity ratio of air. For air flow into the cylinder through the intake valve, p_0 is the intake pressure and p_i and p_T are the cylinder pressures. Similarly, for flow out of the cylinder through the exhaust system, p_0 is the cylinder pressure and p_T is the exhaust system pressure. The reference area A_R , is calculated using the valve curtain area:

$$A_C = \pi D_v L_v \quad (3.2)$$

where D_v is the diameter of the valve head and L_v is the lift of the valve. The use of the valve curtain area is appropriate since it varies linearly with valve lift and is simple to determine compared to the geometric minimum flow area which is a complex function of valve and valve seat dimensions [79]. The reference area does change over to the valve head area when

$$\pi D_v L_v > \pi D_v^2 / 4 \quad (3.3)$$

The curtain area will reach a point at approximately $L_v = D_v/4$ where even though the curtain area is increasing, the airflow is restricted by the throat area of the valve port. The discharge coefficients calculated using the experimental flow rates and theoretical flow rates are shown in Figure 3.2. For the inlet values (Figure 3.2a) maximum values of C_D of just above 0.6 are achieved. For the exhaust valves (Figure 3.2b), maximum values of C_D between 0.65 and 0.75 are achieved. These results are in line with literature for inlet and exhaust valves, where the maximum

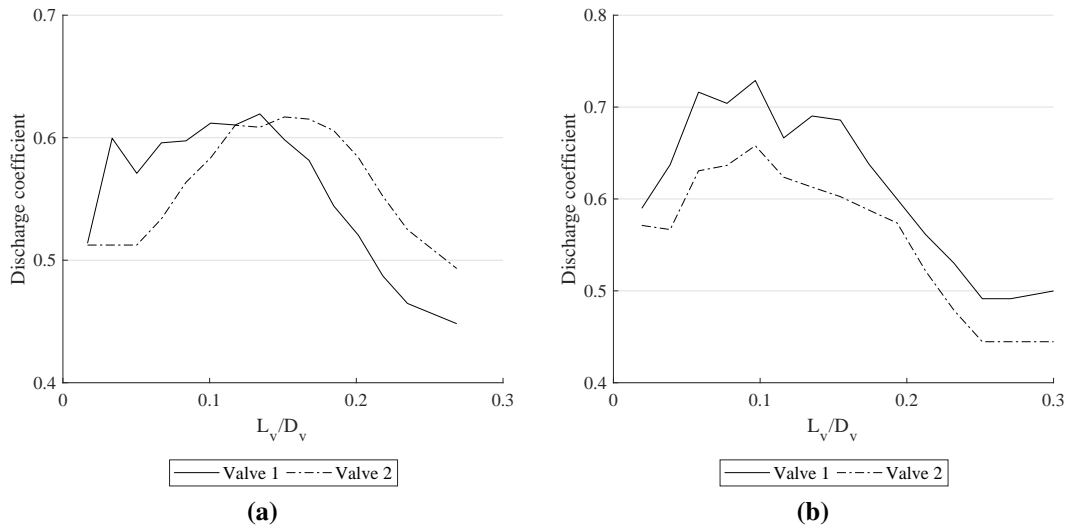


Figure 3.2: Discharge coefficient of the inlet valves (a) and outlet valves (b) as a function of valve lift.

discharge coefficient is achieved between a valve lift to diameter ratio (L/D) of 0.1 and 0.2 [79, 106].

3.2.2.2 Exhaust gas recirculation

In order to ensure that the correct EGR percentage is modelled in Ricardo WAVE, a PID controller is used to control the diameter of an orifice that acts as the EGR control valve with a diameter $D = 30$ mm (Figure 3.3). The system receives mass flow values from the intake as well as the EGR pipe branch going back to the inlet manifold (discussed in Chapter 1, Figure 1.5). The function element calculates the fraction of EGR in the intake charge using the equation:

$$EGR = \frac{\dot{m}_{EGR}}{\dot{m}_{EGR} + \dot{m}_{air}} \quad (3.4)$$

A PID control element receives the current EGR percentage as well as the EGR percentage required by the EGR operating map. The map value is determined by interpolating the given map in Table A.8 using the current engine speed and throttle position. The PID control element outputs a new diameter value for the EGR valve, either closing or opening the valve to ensure the correct percentage of exhaust gas is introduced into the intake air charge. Table 3.2 shows the gain factors used in the EGR control model.

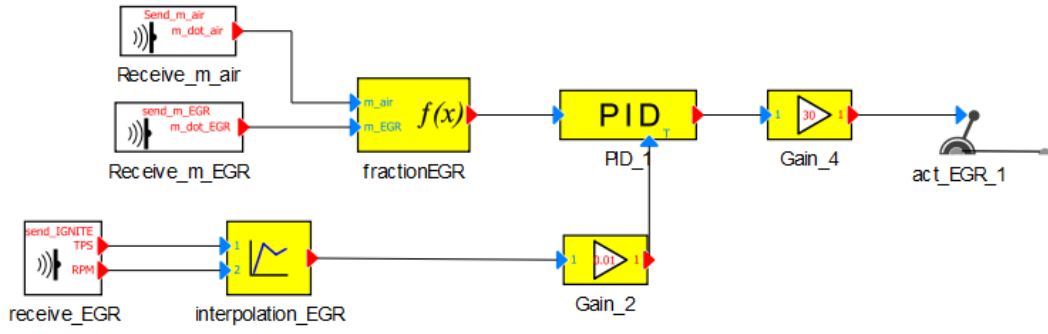


Figure 3.3: Control diagram of EGR used in Ricardo WAVE model.

Table 3.2: PI gain factors for EGR control.

K_p	-0.423573
K_i	-17.486100

3.2.2.3 Fuel injection

The rate of fuel injected is calculated using the pilot and main injection maps as well as the fuel pressure maps available. The injectors used in the engine are Denso injectors with 6 holes; each hole has a diameter equal to $D_{nozzle} = 0.15$ mm. The density of the fuel, ρ_{fuel} is taken equal to 831.1 kg/m³. The value of the density will change in later simulations when different fuel blends are used. The injection pressure p_{inj} is calculated through interpolation using the fuel pressure maps and the engine speed and throttle position. The injection mass flow rate of the pilot injection and main injection respectively are:

$$\dot{m}_{inj} = \rho_{fuel} Q_{inj} \quad (3.5)$$

$$Q_{inj} = C_D A_{nozzle} \sqrt{\frac{2(\Delta p)}{\rho_{fuel}}} \quad (3.6)$$

where C_D is the discharge coefficient of the injector taken equal to 0.9 as per the manufacturer, A_{nozzle} is the total nozzle surface area and Q is the calculated fuel mass flow rate through the injector. The value of Δp can be taken as the value of p_{inj} [79]. The total injected mass can be calculated from the injection mass flow rate and the injection period:

$$m_{inj} = \dot{m}_{inj} \Delta t_{inj} \quad (3.7)$$

Table 3.3: Statistical analysis of the maximum measured in-cylinder pressure

Engine load (%)	n	Mean (bar)	StDev (bar)
2000 rpm			
25	16	65.5	± 3.3
50	28	80.0	± 0.9
75	15	133.7	± 6.4
2500 rpm			
25	48	65.8	± 1.9
50	40	84.1	± 1.6
75	48	132.6	± 1.6
3000 rpm			
25	40	58.9	± 1.3
50	38	81.6	± 0.9
75	41	109.3	± 2.2

3.2.3 Engine operating sub-models

The cylinder element's combustion and emission sub-models are activated for improved combustion and emissions modelling. Each sub-model operation and validation is discussed below. A total of nine steady-state experimental points at engine loads of 25%, 50% and 75% at engine speeds of 2000 rpm, 2500 rpm and 3000 rpm were used in the validation process. Table 3.3 shows the statistical analysis of the experimental in-cylinder pressure data that was used in the combustion model validation process.

3.2.3.1 Combustion sub-model

At each experimental point, cylinder pressure data was recorded. From the pressure data, heat release data for each experimental point was calculated as discussed in Section 1.2.4:

$$\frac{dQ}{d\theta} = \frac{1}{\gamma - 1} \left(p\gamma \frac{dV}{d\theta} + V \frac{dp}{d\theta} \right) \quad (3.8)$$

Once the heat release profile was calculated from experimental cylinder pressure data using Equation 3.8, the fuel mass fraction burned was calculated:

$$\frac{dQ}{d\theta} = m_{inj} q_{LHV} \frac{dx_b}{d\theta} \quad (3.9)$$

where m_{inj} is the mass of fuel injected into the cylinder, q_{LHV} is the fuel's lower heating value and x_b is the mass fraction of fuel burned during combustion.

The fuel burning rate is expressed as the sum of two components relating to the premixed and the diffusion combustion phases. It is given by:

$$\frac{dx_b}{d\theta} = \beta \frac{dx_{bp}}{dt} + (1 - \beta) \frac{dx_{bd}}{d\theta} \quad (3.10)$$

where β is the weight factor expressed as the ratio between the fuel burned by premixed combustion and the total fuel burned. The rate of fuel burned is given by:

$$\frac{dx_b}{d\theta} = a(m+1) \left(\frac{1}{\Delta\theta_{comb}} \right) \left(\frac{\theta - \theta_{comb}}{\Delta\theta_{comb}} \right) \exp \left[-a \left(\frac{\theta - \theta_{comb}}{\Delta\theta_{comb}} \right)^{m+1} \right] \quad (3.11)$$

where m and a are the Wiebe function tuning parameters, $\Delta\theta_{comb}$ is the duration of the energy release for the combustion event and θ_{comb} is the start of combustion crank angle degree. Ricardo WAVE has a built-in combustion sub-model tool, multi-Wiebe combustion fitting tool, which provides the values for parameters needed in the generic semi-predictive combustion model:

- Location of 50% burn point
- Combustion duration
- Wiebe exponent (m)
- Mass fraction burned, β (Equation 3.10)

Some of the parameters are shown visually in Figure 3.4. Total combustion of the fuel is assumed which results in $a = 6.9$. The assumption of total combustion for the Wiebe combustion model is acceptable based on previous research that also used the same assumption [67]. These parameters are calculated by the software when the experimental cylinder pressure data is provided. The software can fit a total of 8 Wiebe functions to the heat release data, but it is generally accepted that two Wiebe functions can accurately represent most heat release profiles [94]. One Wiebe function usually represents the premixed burn duration and the other Wiebe function represents the diffusion burn duration. The downside of using Ricardo WAVE's fitting tool is that the values generated are only valid for the engine operating points under consideration. Also, the fitting tool uses the 50% burn point to shift the combustion profile, while the use of the start of combustion crank angle degree is used widely in published research [65–67]. Rather than using Ricardo WAVE's fitting tool to generate parameters for the Wiebe combustion model, the Wiebe

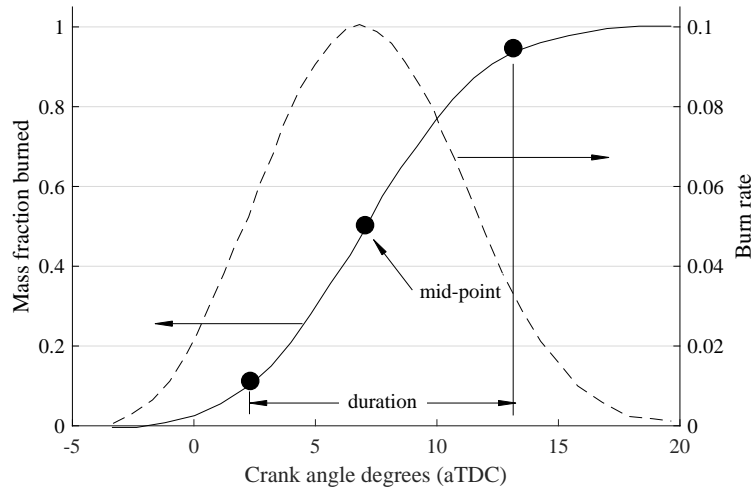


Figure 3.4: Illustration of parameters used by Ricardo WAVE.

combustion model parameters were determined manually and a regression model fitted to the data. This ensures flexibility for when the engine model is run at engine operating points that are different from the experimental points in the validation process. According to the Ricardo WAVE's literature, the software uses a modified Wiebe combustion model that is different from Equation 3.11:

$$x_b = 1 - \exp \left[-a(\theta_i - \theta_0)^{m+1} \right] \quad (3.12)$$

where θ_i is the i_{th} crank angle and θ_0 is the start of combustion crank angle. For multiple Wiebe combustion models, Equation 3.10 is used to determine β . A correlation analysis was conducted to derive multiple regression equations that express the parameters as a function of engine operating values. The equation for start of combustion (SOC) is:

$$\theta_0 = 24.95 - 6.93p_0 + 0.689\theta_{minj} \quad (3.13)$$

where p_0 is the inlet charge pressure in bar and θ_{minj} is the injection timing of the main fuel injection in degrees after Top Dead Center (aTDC). For calculating the fraction of fuel burned in the premixed phase (β):

$$\beta = -3.55 - 0.0524\theta_{pinj} + 0.007056\Delta\theta_{pinj} \quad (3.14)$$

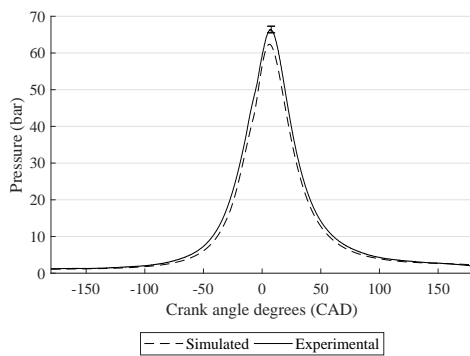
where θ_{pinj} is the injection timing of the pilot fuel injection in degrees aTDC and $\Delta\theta_{pinj}$ is the injection duration of the pilot injection in microseconds. The Wiebe

fitting parameters can be calculated using:

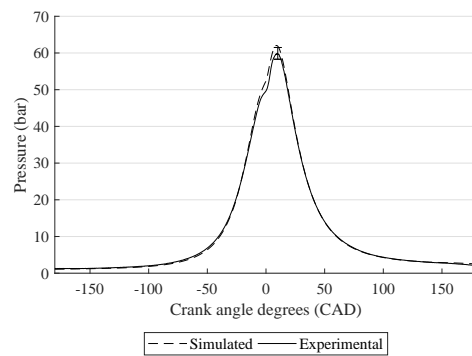
$$m_p = 1.027 - 0.00024n \quad (3.15)$$

$$m_d = 1.027 - 0.0002n \quad (3.16)$$

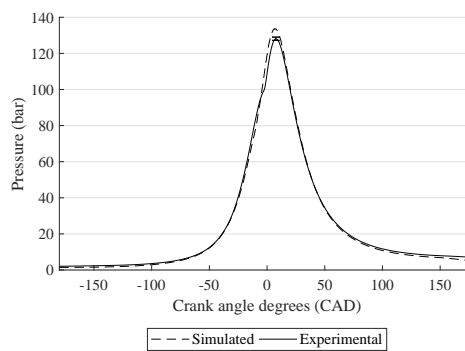
where n is the engine speed in revolutions per minute (rpm). All the terms of the correlation equations generated for the Wiebe combustion model were found to be significant with $p < 0.02$. Furthermore, the regression statistics goodness of fit (R^2) showed high values of 93% for θ_0 , 97% for β , 65% for m_p and 71% for m_d . Figures 3.5 shows the comparison between the experimental in-cylinder pressure profiles and the simulated results when using the multi-Wiebe combustion model.



(a) Wiebe functions at 2000 rpm and 25% load.



(b) Wiebe functions at 2500 rpm and 25% load.



(c) Wiebe functions at 3000 rpm and 75% load.

Figure 3.5: In-cylinder pressure profile comparison between steady-state experimental data and simulated data.

3.2.3.2 Emissions sub-models

CO emissions and NO_x emissions were validated using steady-state data. As mentioned in Section 1.2.7.5, the calculation of CO emissions uses a two step mechanism

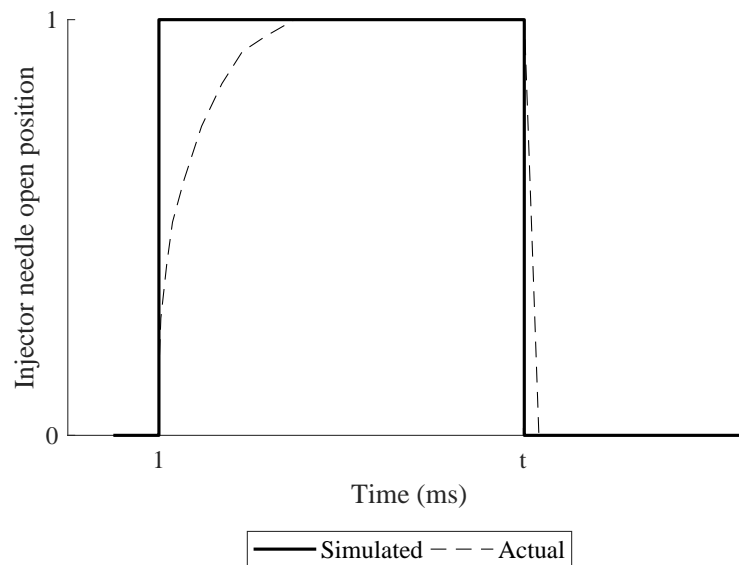


Figure 3.6: Illustration of a different simulated injector operating events.

(Equation 1.23 and Equation 1.24) as well as the reaction kinetics between CO and the hydroxyl radicals (Equation 1.22). In Ricardo WAVE, the combustion model assumes total combustion of the fuel with the Wiebe parameter set at $a = 6.9$. As such all fuel is combusted, except when over fuelling occurs. This is evident in the software when the CO emissions is abnormally high. It is thus necessary to change the amount of fuel specified according to the fuel map values used from the after market ECU. The only information provided by the ECU, is the open time of the injector in μs . It is thus only possible to simulate an injection event as a step change from close to open and open to close. The disadvantage of using step changes when modelling fuel injection is that it is not representative of a real injection event. The change from fully closed to fully open occurs over a period of time rather than instantly. The same is true for the injector closing event. This is visually illustrated in Figure 3.6. Simulating injector operation as a step change can introduce more fuel than is accurate and can result in very high simulated CO emissions. It is necessary to alter the fuel flow parameters (Equation 3.7) to ensure accurate calculation of CO emissions. The validation of the simulated CO emissions of the engine simulation compared to steady-state experimental results are shown in Figure 3.7. Simulated results are in good agreement with the experimental values.

For NO_x emissions, the user-defined values for ARC_1 and $AERC_1$ in Equation 1.26 and Equation 1.27 can be used to ensure the simulated and experimental NO_x emission values correspond to each other. The value of ARC_1 was kept at 1.5 and the value of $AERC_1$ was changed to fit the experimental data. The values used for $AERC_1$ in the emission models are shown in Table 3.4. The validation of the

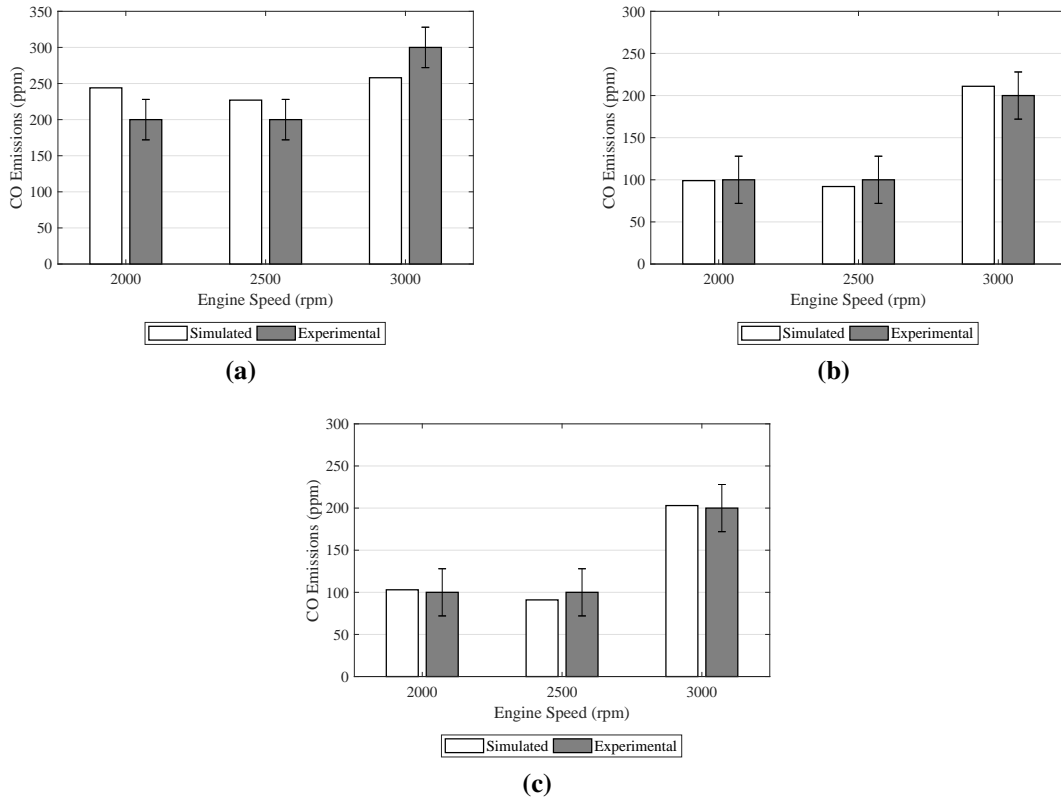


Figure 3.7: CO engine emissions comparison between steady state experimental data and simulated data for different engine speeds at (a) 25% load, (b) 50% load and (c) 75% load [60].

simulated NO_x emissions of the engine simulation compared to steady-state experimental results are shown in Figure 3.8. Simulated results are in good agreement with the experimental values.

3.3 Ricardo IGNITE development

The use of the lower fidelity Ricardo IGNITE enables the simulation to undergo a legislative driving cycle or any other custom-programmed route. Vehicle characteristics such as frontal area, wheel diameter, engine inertia as well as vehicle weight are

Table 3.4: User defined values for $AERC_1$ for the NO_x emissions sub-model.

Engine load (%)	2000 rpm	2500 rpm	3000 rpm
25	0.95062	0.90000	1.21667
50	1.12603	1.12222	1.11070
75	1.06222	1.11667	1.07592

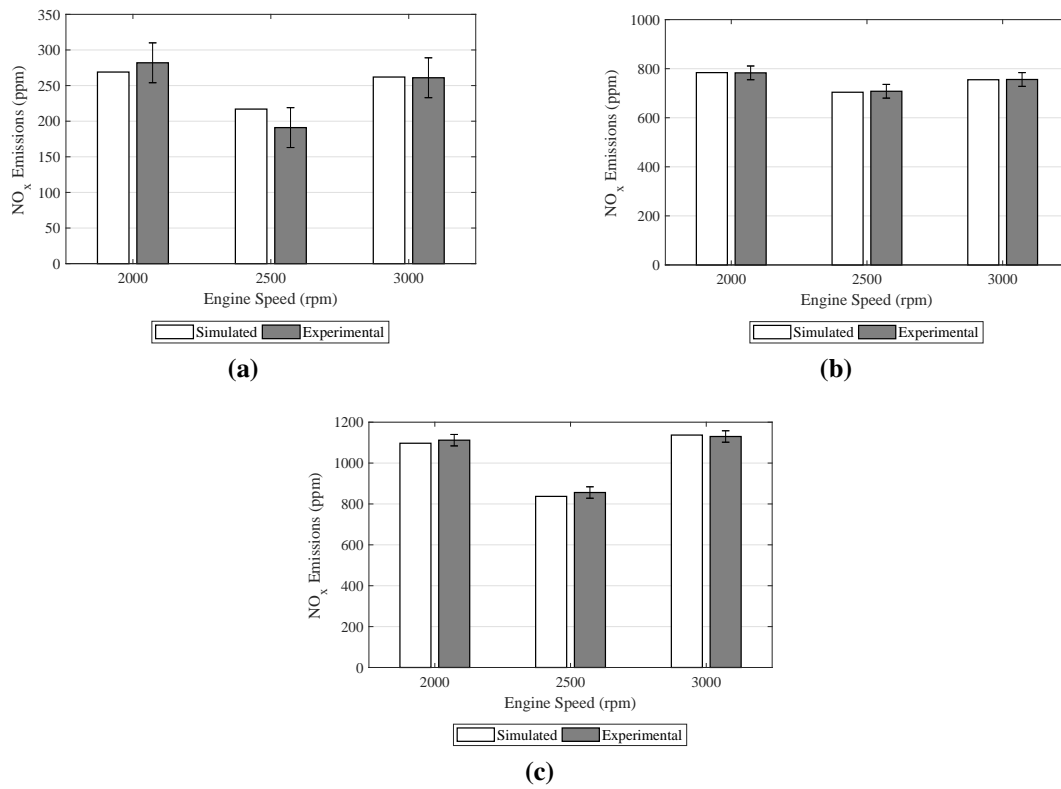


Figure 3.8: NO_x engine emissions comparison between steady state experimental data and simulated data for different engine speeds at (a) 25% load, (b) 50% load and (c) 75% load [60].

Table 3.5: Ricardo IGNITE input data.

Description	Data
Vehicle test mass (kg)	3500
Vehicle frontal area (m ²) [107]	5.6
Wheel radius (m)	0.33
Engine inertia (kgm ²)	0.343
Rolling resistance coefficient	0.01125
Drag coefficient [107]	0.445

Table 3.6: Gear ratios used in Ricardo IGNITE.

Gear number	Gear ratio
1	5.441
2	2.840
3	1.721
4	1.223
5	1.000
6	0.794
Final drive ratio	3.730

also required for the simulation. IGNITE calculates the required engine speed and load in order to follow the defined driving cycle.

3.3.1 General set-up

The input used in the development of the simulation is listed in Table 3.5. The engine inertia and the rolling resistance coefficient were calculated using the procedure as set out by Kunninger [108]. The NEDC driving cycle is pre-programmed in IGNITE and can be selected when choosing the required driving cycle. Other information such as the gear shift strategy, is available in the Council Directive 91/441/EEC [109]. The gearbox ratios for the vehicle as well as the final drive ratio are shown in Table 3.6. The gear ratios are available in the Ford workshop manuals [110]. A Ricardo WAVE engine object was also added to the IGNITE simulation (Figure 3.9) to enable co-simulation between the two simulation packages.

3.3.2 Validation of simulation

The engine speed profile was calculated using the following equation:

$$RPM = \frac{30vG_tG_f}{\pi R} \quad (3.17)$$

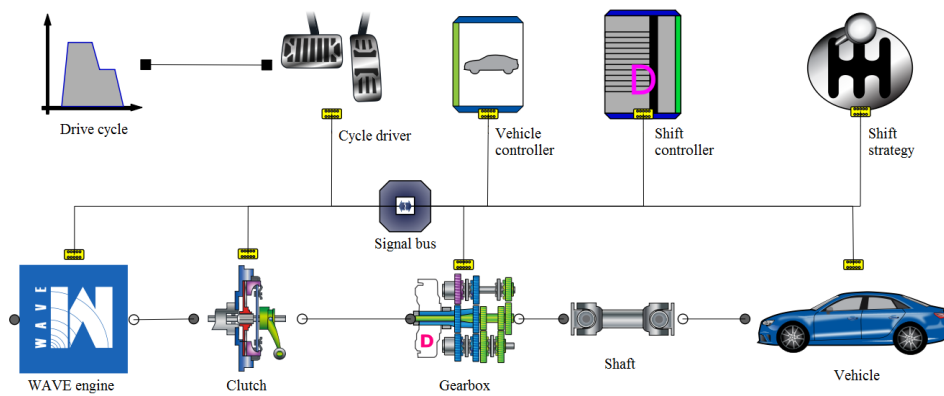


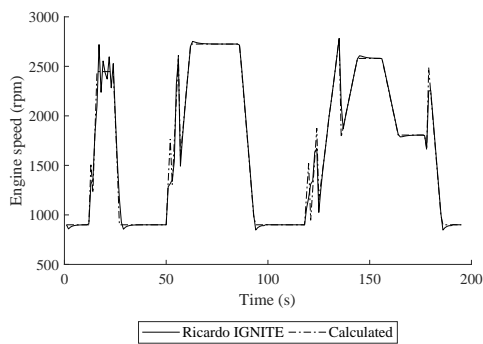
Figure 3.9: Vehicle simulation in Ricardo IGNITE [93].

Table 3.7: PI gain factors for IGNITE driving model.

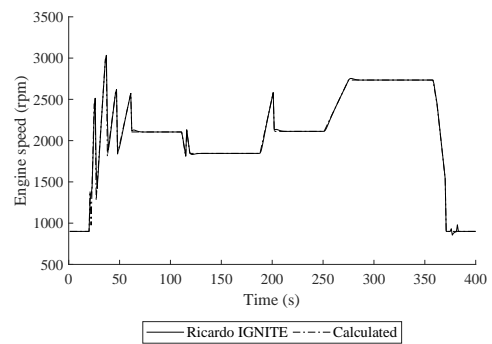
K_p	2.000
K_i	0.005

The speed of the vehicle, v in m/s, is available from the driving cycle profile, R in m, is the radius of the wheels, and G_t and G_f are the current gear ratio selected and the final drive ratio of the drive train, respectively. Figure 3.10a and Figure 3.10c show the results of the comparison for the NEDC urban cycle and Figure 3.10b and Figure 3.10d show the results of the comparison for the NEDC extra urban cycle. Both graphs show good agreement between the IGNITE generated profiles and the calculated profiles. In Figure 3.10c as well as in Figure 3.10d there are slight overshoots evident just after each acceleration period and deceleration period for the IGNITE calculations. This is caused by the fact that IGNITE is using a PID controller to calculate acceleration and braking for the vehicle to ensure that it accurately follows the programmed driving cycle [93]. Table 3.7 lists the PI controller factors that were used in the IGNITE model to accurately follow the drive cycle. The overshoot is within the tolerance of ± 1 km/h set out in the Council Directive 91/441/EEC [109].

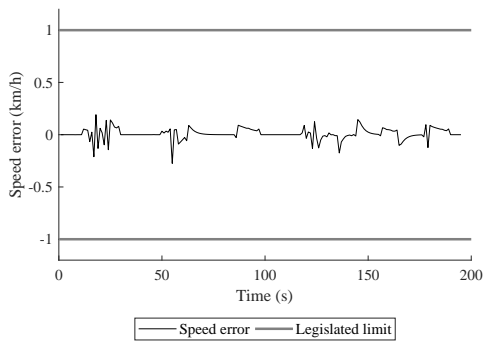
The engine load requirements as calculated by IGNITE for the NEDC drive cycle were validated using the procedure as set out by Kunninger [108]. The powertrain of a vehicle converts the torque developed by the engine into torque available at the wheels of the vehicle. Key rotating elements that form the powertrain are shown in Figure 3.11a. Figure 3.11a represents a manual transmission which include the gearbox gear ratio (G_t) and the final drive ratio (G_f). Other rotational parts include the inertia of the engine (I_e), the clutch (I_c), the transmission (I_t), the drive shaft (I_{dr}), the differential (I_f), the wheel axle (I_{ax}) and the wheel (I_w). The system shown in



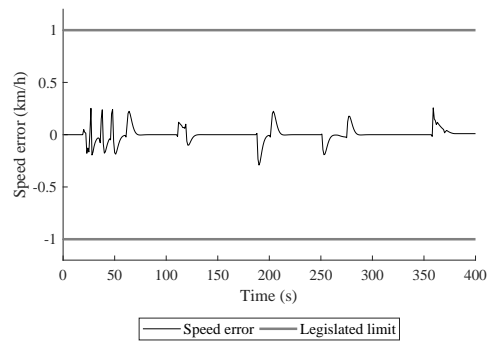
(a) Variation of vehicle speed over the NEDC urban cycle for Ricardo IGNITE simulation and calculated results.



(b) Variation of vehicle speed over the NEDC extra urban cycle for Ricardo IGNITE simulation and calculated results.



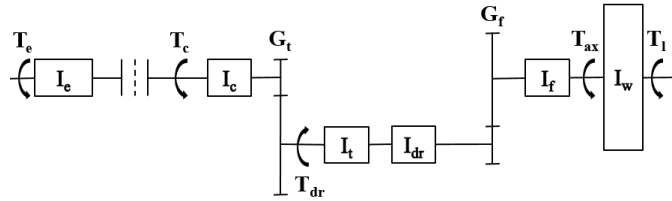
(c) IGNITE speed error compared to NEDC urban cycle.



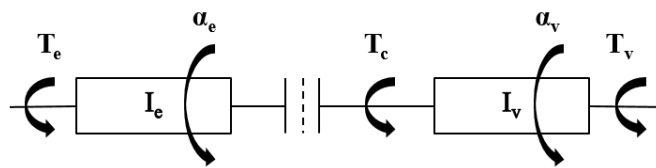
(d) IGNITE speed error compared to NEDC extra urban cycle.

Figure 3.10: Comparison between Ricardo IGNITE and calculated engine speed for the NEDC [111].

Figure 3.11a can also be represented by an equivalent system shown in Figure 3.11b in which all the torque and speed values are related back to the engine clutch interface [112]. Considering Figure 3.11b and starting with the engine, the torque available



(a) Mechanical elements of the powertrain system.



(b) Equivalent torque system of the vehicle powertrain.

Figure 3.11: Illustration of simplifying the complex inertia system of the powertrain.

at the clutch needs to be determined. T_e and T_c will differ as the engine needs to generate an amount of torque to accelerate the inertia of the engine and any other rotating parts attached to the engine. The torque available at the clutch can be calculated using Newton's second law:

$$T = I\alpha \quad (3.18)$$

where T is torque, I is inertia and α is rotational acceleration. Frictional losses from bearings and other mountings in the vehicle transmission are omitted as it is deemed negligible [108]. For the available torque at the clutch (decoupled):

$$T_c = T_e - I_e\alpha_e \quad (3.19)$$

where I_e is the inertia of the engine. Equation 3.19 can be rewritten as:

$$\alpha_e = \frac{T_e - T_c}{I_e} \quad (3.20)$$

Similarly, for the vehicle:

$$\alpha_v = \frac{T_c - T_v}{I_v} \quad (3.21)$$

With the clutch engaged, Equation 3.20 and Equation 3.21 can be combined:

$$\alpha_e = \alpha_v = \frac{T_c - T_v}{I_v} \quad (3.22)$$

In order to determine the torque required at the clutch:

$$T_c = T_v + I_v \alpha_e \quad (3.23)$$

where I_v is the inertia of the vehicle and α_e is the rotational acceleration of the engine. A correlation can be used to determine I_v :

$$I_v = \frac{f_m m R^2}{G_f^2} \quad (3.24)$$

where f_m is the mass factor, m is the mass of the vehicle, R is the radius of the tyre and G_f is the final drive gear ratio. For the mass factor [113]:

$$f_m = 1 + 0.04G_f + 0.0025G_f^2 \quad (3.25)$$

To calculate T_v required at the clutch:

$$T_v = \frac{(F_r + F_a)R}{G_t G_f \eta_{tf}} \quad (3.26)$$

where F_r and F_a are the rolling resistance and aerodynamic forces, respectively. R is the radius of the tyre, G_t and G_f is the gearbox gear ratio and the final drive gear ratio, respectively. η_{tf} is the efficiency of the drive line. Forces due to the rolling resistance can be calculated using:

$$F_r = f_0 + 3.24f_1 \left(\frac{v}{44.704} \right)^{2.5} \quad (3.27)$$

where f_0 and f_1 are empirically derived coefficients that depend on the tyre pressure and can be obtained from Figure 3.12. The aerodynamic forces can be calculated using:

$$F_a = \frac{1}{2} \rho_{air} C_d A v^2 \quad (3.28)$$

where ρ_{air} is the density of air, A is the frontal area of the vehicle and C_d the coefficient of drag for the vehicle. All values used in the calculations of the torque required at the clutch of the vehicle are listed in Table 3.5.

Figure 3.13a shows the results of the comparison between the calculated engine

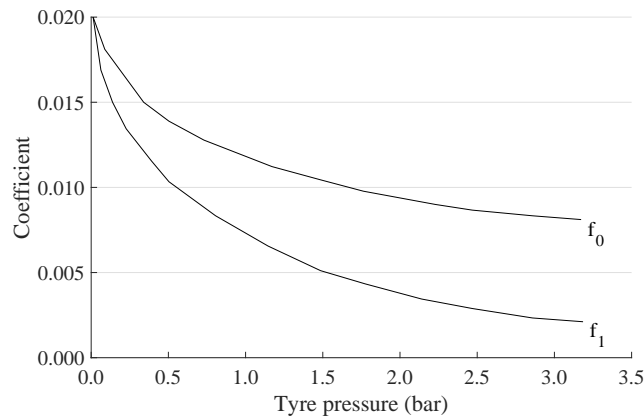
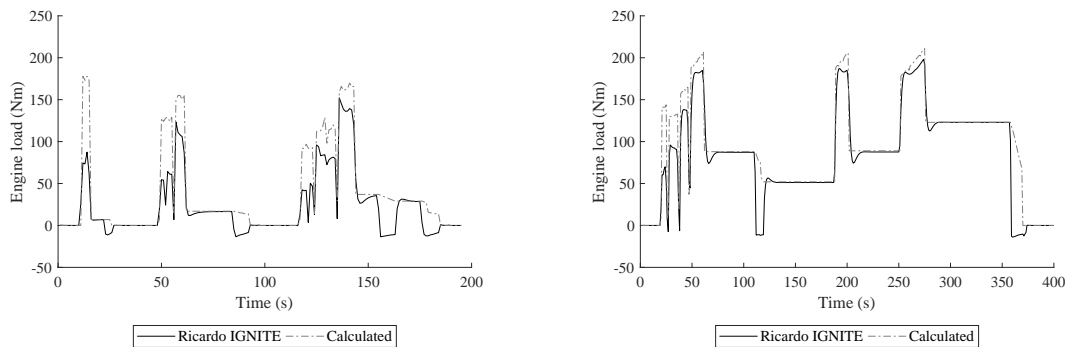


Figure 3.12: Empirically derived coefficients for the calculation of rolling resistance of vehicle tyres [108].

load requirements and the IGNITE results for the NEDC urban cycle and Figure 3.13b compares the results for the NEDC extra urban driving cycle. The biggest differences



(a) Variation of vehicle load over the NEDC urban cycle for Ricardo IGNITE and calculated results.

(b) Variation of vehicle load over the NEDC extra urban cycle for Ricardo IGNITE and calculated results.

Figure 3.13: Comparison between Ricardo IGNITE and calculated engine load for the NEDC [111].

between the compared data sets are during the acceleration and braking stages. Ricardo IGNITE does not state what equations it uses in order to determine the inertial forces that dominate the acceleration stages and as such it is difficult to accurately replicate IGNITE's results. The differences in calculations for the steady state sections of the driving cycle are negligible. Differences in calculated torque and the torque values calculated by IGNITE are also evident after an acceleration or braking event. The difference in these calculated torques can be attributed to the acceleration PID controller in IGNITE [93]. The PID controller uses a feed forward model that dynamically estimates a non-dimensional load level required to follow the drive cycle. Just after an acceleration event, the load requirements reduces

significantly and it can take the controller some time to adjust accordingly. The settling time can be decreased with a smaller time step to increase its accuracy, at the expense of simulation time. Braking events in the NEDC are also evident with the IGNITE calculated engine torque values being negative. The braking calculations were not in the scope of the validation and these events will be seen as zero demand in torque for the engine in the dynamometer drive cycle program.

The high level validation of Ricardo IGNITE was successful with the engine speed and engine torque requirements closely correlating with the calculated requirements. Larger differences were evident when the torque requirements were compared and are contributed to the simplicity of the model used for the validation purpose as well as not knowing what models Ricardo IGNITE is using to determine equivalent inertia forces during acceleration. Ricardo IGNITE can simulate vehicle requirements accurately and will be used going forward in this project.

3.4 Co-simulation set-up

A wiring connector element is used in Ricardo WAVE to link control elements to Ricardo IGNITE. Any control element which is connected to a *From WAVE* pin on the wiring connector element sends its signal out to the external program. Any control element which is connected to a *To WAVE* pin on the wiring connector element receives its signal from the external program. Figure 3.14 shows the wiring connector used in the engine model to send and receive signals. A compulsory

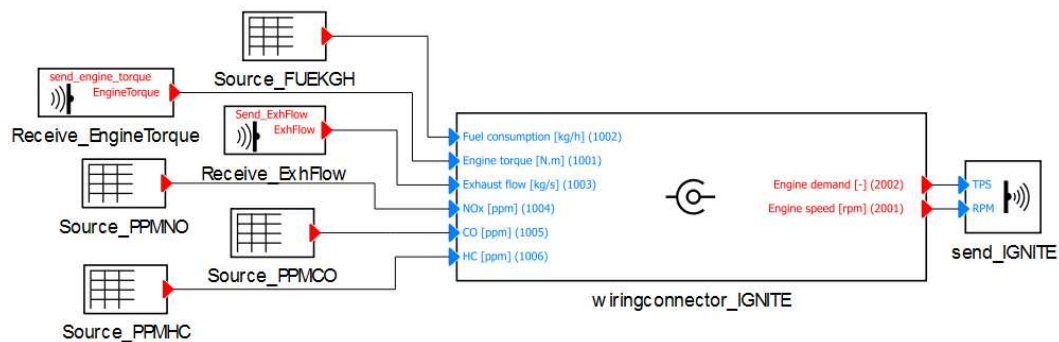


Figure 3.14: Wiring connector between Ricardo WAVE and Ricardo IGNITE.

signal that need to be sent to Ricardo IGNITE, is engine torque (Nm). Similarly, compulsory signals that Ricardo WAVE needs are engine demand (% throttle) and engine speed (rpm). Other signals such as the emissions generated by the engine model have also been added to ensure calculations of engine emissions over the whole drive cycle is possible.

3.5 Closing remarks

This chapter investigated the set-up and validation of a one dimensional single zone model for the test engine at the University of the West of England as well as a vehicle systems simulation for drive cycle investigations. The following can be concluded:

1. The use of experimental data to validate the engine simulation in Ricardo WAVE as well as the vehicle model in Ricardo IGNITE is effective.
2. When trying to duplicate Ricardo IGNITE's engine load requirement over a drive cycle, large differences are evident due to the simplicity of the model used as well as not knowing what models Ricardo IGNITE are using to determine equivalent inertia forces during acceleration.
3. The sample size of the experimental data used in this study to validate the engine combustion and emissions models is modest and a more comprehensive validation is needed when this model is used again in this research project.
4. The same validation procedure for the WLTP drive cycle is unnecessary as IGNITE will use the same vehicle characteristics for calculating the engine load and speed.

Chapter 4

Optimising emissions reduction using biofuel

This chapter contributes to the determination of an acceptable fuel blend that will increase the renewable content of fuel used in the transport industry as well as reduce regulated emissions when tested over the WLTP legislative drive cycle. This will be done through the use of a mixture DoE statistical tool. In using the mixture DoE, it is demonstrated that an engine's response can be successfully characterised with the use of statistical tools and that the results are useful to use in determining a suitable blend for emissions reduction as well as increasing the renewable content in fuel blends. The results obtained demonstrate that it is possible to decrease engine emissions with the use of binary and ternary fuel blends and that the use of ethanol in fuel blends with diesel and biodiesel contributes to further emission reduction and an increase in renewable fuel content.

Initially, an investigation is presented into the use of a mixture DoE as well as the interpretation of the results from the statistical tool, after which the use of an optimisation tool is investigated to get an acceptable fuel blend for increased renewable content in the fuel blend as well as maximum emissions reduction.

4.1 Introduction

As part of the targets set out by the Kyoto Protocol (Table 1.1), the EU needs to ensure that all member states collectively reduce their GHGs by 20% by 2020. One aspect that will help reduce the EU's GHG emissions, is increasing the renewable energy content in the transport sector. The UK needs to achieve a renewable energy content of 10% by 2020 of total energy used in transport, but as of 2018, it has only reached approximately 4.5% (Figure 1.2). Traditionally, biodiesel is used together with diesel while ethanol is used together with petrol in binary blends to offset the use of carbon fuels in the transport sector. As mentioned in Section 1.2.5, research has also gone into the use of ternary fuel blends between diesel, biodiesel and ethanol to try and increase the renewable content of transport fuel, but also to reduce harmful emissions. This chapter will focus on determining a ternary blend that will aid the UK in achieving its 10% renewable energy in transport target, as well as reducing harmful emissions produced by compression ignition (CI) engines.

In order to determine a suitable blend of diesel, biodiesel and ethanol that will reduce engine emissions, a multivariate analysis is needed to provide a clear and thorough knowledge of the combustion characteristics of the engine. As mentioned in Section 1.2.5, the operation of the engine also needs to be taken into account as the operating envelope of the engine, together with the use of different renewable fuels, has a wide range of different effects on harmful emissions. The use of non-linear techniques like Design of Experiment (DoE) are suitable to explore the interaction effects of diesel, biodiesel and ethanol and its effect on engine responses. DoE is the most cost effective and economical technique to evaluate the individual effects and combined effects of the blend components on the output response [114]. DoE techniques have been used successfully in other studies to investigate the effects between engine speed and load and blends between diesel, biodiesel and ethanol [44], to quantify the effects of fuel compositions on GDI-derived particle emissions using a mixture DoE [115] and to optimise a double pilot injection strategy to improve diesel performance and emissions [54]. Although multiple studies used DoE to optimise engine system parameters, the instances where mixture DoEs were used to optimise ternary fuel blends over a given drive cycle is scarce.

The following sections investigate the use of a mixture DoE to characterise the response of a CI engine fuelled with ternary blends of diesel, biodiesel and ethanol while being tested over the WLTP. Engine responses that were considered are CO emissions, CO₂ emissions (tank-to-wheel emissions), NO_x emissions and engine fuel consumption. The results for each exhaust emission are analysed, before the holistic improvement of the engine emissions and performance is discussed.

4.2 Experimental set-up

The following subsections explore the set-up of the mixture DoE. The physiochemical properties of diesel, biodiesel (rapeseed methyl ester) and ethanol as well as the binary and ternary blends are listed in Table 4.1. The physiochemical properties of the pure blends shown in Table 4.1 are provided by the fuel supplier, while the physiochemical properties of the binary and ternary blends are calculated.

Table 4.1: Physiochemical properties of diesel, biodiesel, ethanol and their blends.

	Cetane number	LHV (MJ/kg)	Density at 15 °C (kg/m^3)	Viscosity at 40 °C (mm^3/s)	CFPP (°C)	Flash point (°C)
Diesel	51.7	42.8	831.1	2.686	-26	65
Biodiesel	52.8	38.0	883.2	4.372	-6	179
Ethanol	7.0	26.8	790.0	1.200	-38	20
B20	51.9	41.8	841.5	3.023	-22	87
E20	42.8	39.6	822.9	2.388	-28	56
B14E3	50.5	41.6	837.2	2.877	-24	78
B3E14	45.5	40.4	826.9	2.529	-27	60
B3E3	50.4	42.2	831.4	2.692	-26	58
B7E7	48.7	41.3	831.9	2.700	-25	66

4.2.1 Design of experiment set-up

A mixture design approach was adopted to explore the individual effects of diesel, biodiesel and ethanol and their interactions in a blend for different engine responses. The selection of the mixture DoE is appropriate as the sum of the input variables, in this case the blend components, must be unity [116]. As opposed to a response surface design, the factors in a mixture design are not independent from each other. If x_1, x_2, \dots, x_p denote the proportions of p components of a blend (volumetrically based), then

$$0 \leq x_i \leq 1 \quad i = 1, 2, \dots, p \quad (4.1)$$

and

$$x_1 + x_2 + \dots + x_p = 1 \quad (4.2)$$

For a mixture design with three components, the design space is a triangle with vertices corresponding to formulations that are pure blends (100% of one blend). Figure 4.1 shows an extreme vertices design, where upper limits have been set to the amount of biodiesel and ethanol. The upper limits are based on previous research

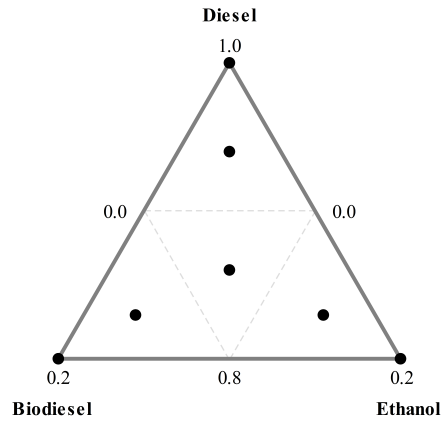


Figure 4.1: Extreme vertices simplex design plot of the mixture DoE.

[33, 34] where the maximum addition without engine modification was determined:

$$x_D + x_B + x_E = 1 \quad x_B, x_E \leq 0.2 \quad (4.3)$$

where x_D is the fraction component of diesel, x_B is the fraction component of biodiesel and x_E is the fraction component of ethanol in the blend. Centroid and axial points have been added to the design to increase its capability to fit models for ternary blends. The centroid point and axial points are shown in Figure 4.1 and were calculated using:

$$\begin{aligned} x_D &= 0.83, x_B = 0.14, x_E = 0.03 \\ x_D &= 0.83, x_B = 0.03, x_E = 0.14 \\ x_D &= 0.86, x_B = x_E = 0.07 \\ x_D &= 0.94, x_B = x_E = 0.03 \end{aligned} \quad (4.4)$$

The whole mixture design was replicated once and the runs were randomised to ensure experimental errors are independently distributed. The mixture design consists of one centroid point, three axial points and three vertices points. With the replication, a total of 14 runs of mixture experiments were used to analyse the data acquired from the experimental runs.

4.2.2 Flushing Procedure

The flushing procedure as set out in Section 2.3.3 was used.

4.2.3 Mixture stability

The diesel, biodiesel and ethanol fuel were mixed in batches of 5 L in the determined blend ratios based on the mixture DoE. The fuels were mixed together using lab equipment with an accuracy of 10 ml to make the homogeneous fuel blends. Samples of each blend were then kept in a sealed glass container for a maximum of 24 hours to observe its physical appearance. All blends, except E20, exhibited a stable mixture, with no observable separation between the different fuels evident. Figure 4.2 shows the E20 fuel sample, where it is evident that the ethanol and diesel has separated from each other. 2 Ethanol is immiscible with diesel fuel over a wide range of



Figure 4.2: Qualitative check for blend stability for E20 fuel blend [41].

temperatures, leading to separation. Consequently, in many cases the presence of a surfactant and co-solvent additive in the binary blends between diesel and ethanol becomes necessary. Lapuerta *et al.* [117] found that the water content in ethanol, temperature of the fuel and percentage of additive used can influence the stability of the binary blend between diesel and ethanol. Binary blends with a maximum of approximately 10% ethanol in the blend can be used in diesel engines in countries where temperatures rarely fall below -5°C . The addition of stability additives will increase miscibility of the fuel thus extending the use of binary blends of diesel and ethanol to colder countries. Hansen *et al.* [118] also found that the stability of the fuel blend depends on temperature and ethanol's water content. For blends between dry ethanol and diesel, the blend was stable for temperatures higher than 10°C . Fernando and Hanna [119] and Kwanchareon *et al.* [39] found that biodiesel can be used successfully as an amphiphile (a surface-active agent) to stabilize ethanol and diesel. They reported that the addition of biodiesel to the binary blend between ethanol and diesel increases the lubricity characteristics of the blend and makes it

stable well below sub-zero temperatures. For the testing of E20, no additives were added to the blend to improve its stability as the addition of additives could influence the results [120]. Qualitative checks showed that after approximately 25 minutes, signs of separation was evident in the E20 blend. The homogeneity of the blend was ensured by actively stirring the fuel blend during testing with a magnetic stirrer.

4.3 Results

In this present study, the effects of different blends of fuel on different engine responses were considered. Fuel blends included binary and ternary blends between diesel (x_D), biodiesel (x_B) and ethanol (x_E). Engine responses include CO, CO₂, NO_x emissions as well as fuel consumption when tested over the WLTP drive cycle. The experimental response of 14 runs in the design matrix (Figure 4.1) along with their corresponding points of the fitted mixture design are shown in Table 4.2. All 14 runs were cold start runs, with the engine oil and cooling water temperature at approximately 20 °C ($\sigma = 2$) at the start of each test. The principal model analysis was based on the analysis of variance (ANOVA) which provided statistical information including the p-values of the different model terms (Table 4.3). P-values of less than 0.02 are deemed as highly significant, which means that the probability of this phenomena is due to chance is less than 2% [121, 122].

The residual error of the mixture DoE is made up of the pure error and the lack of fit error terms. The pure error term reflects on the variability of the observations within each response and the lack of fit term measures the error due to deficiency in the statistical model. The mean square of each term can be used to test the significance of the lack of fit relative to the pure error term. If it is deemed non-significant, then the model is acceptable. The lack of fit term's significance is listed in Table 4.3.

Each engine response is discussed in more detail in the sections below.

4.3.1 Evaluation of CO₂ emissions

The quadratic model developed for CO₂ emissions as fitted based on the mixture design corresponds to:

$$\begin{aligned} Z_{\text{CO}_2} = & 251 \times x_D - 2721 \times x_B + 3768 \times x_E \\ & + 3660 \times x_D \times x_B - 4438 \times x_D \times x_E \\ & + 634 \times x_B \times x_E \end{aligned} \quad (4.5)$$

Table 4.2: The experimental values of the engine response for the mixture DoE.

Run	Parameter settings			Experimental response (g/km)			
	x_D	x_B	x_E	CO	CO ₂	NO _x	FC
1	0.80	0.00	0.20	2.0598	244.52	1.0812	134.00
2	0.83	0.14	0.03	1.2046	258.74	1.0841	122.75
3	0.83	0.03	0.14	1.4141	232.37	1.0584	128.75
4	0.86	0.07	0.07	1.1409	251.43	1.0566	119.27
5	1.00	0.00	0.00	1.0182	252.03	1.1148	120.64
6	0.83	0.14	0.03	1.0624	257.02	1.0841	121.11
7	0.80	0.20	0.00	0.8844	238.07	1.0669	123.23
8	0.83	0.03	0.14	1.2837	232.37	1.0370	129.98
9	0.94	0.03	0.03	0.9863	244.98	1.0741	121.79
10	0.80	0.20	0.00	0.8868	247.06	1.0714	126.50
11	0.94	0.03	0.03	0.9724	247.48	1.0948	126.57
12	1.00	0.00	0.00	0.9874	251.08	1.1518	116.41
13	0.86	0.07	0.07	1.0638	241.27	1.0635	121.18
14	0.80	0.00	0.20	1.9894	245.00	1.0764	135.50

Table 4.3: P-values of the engine response for the mixture DoE.

	CO	CO ₂	NO _x	FC
Linear	< 0.02	< 0.02	< 0.02	< 0.02
Quadratic	< 0.02	< 0.02	< 0.02	0.078
$x_D \times x_B$	< 0.02	< 0.02	0.351	0.973
$x_D \times x_E$	< 0.02	< 0.02	< 0.02	0.297
$x_B \times x_E$	0.249	0.392	0.894	0.030
Lack-of-Fit	0.948	0.782	0.829	0.068

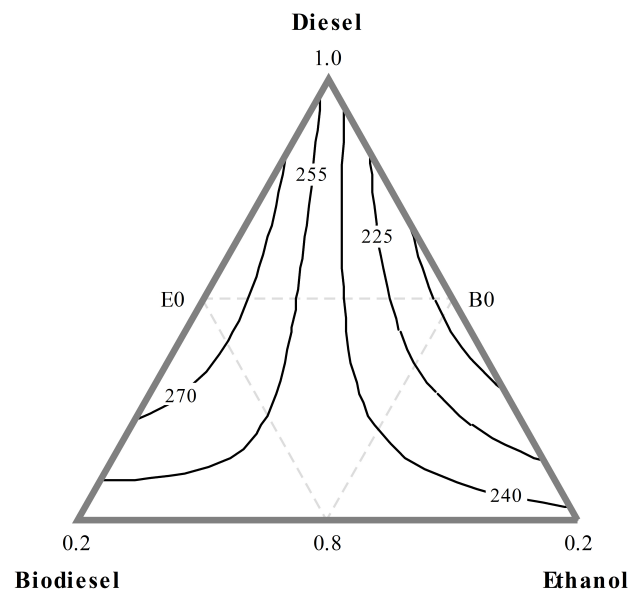


Figure 4.3: Contour plot of the engine response over the WLTP for CO₂ emissions in grams per kilometer [41].

where Z_{CO_2} is the CO₂ emissions in the exhaust gas of the engine in grams per kilometer. The linear terms as well as the quadratic terms in Equation 4.5 are significant with $p < 0.02$. The interaction between the diesel and biodiesel terms and the diesel and ethanol terms are also significant. Interaction between the biodiesel and ethanol terms are not significant, as shown in Table 4.3. High values of R^2 (88.30%) and adjusted R^2 (80.99%) respectively for Equation 4.5 indicate a high correlation between the observed and the predicted values of CO₂ emissions. The variation of CO₂ emissions response with fuel blends based on the model developed from DoE is shown in Figure 4.3. A region of minimum CO₂ emissions is evident for binary blends between diesel and ethanol. For blends of approximately E5 to E15, CO₂ emissions of less than 225 g/km were predicted. Ethanol has a high carbon to hydrogen ratio (3 compared to 1.83 for gasoline) which reduces the CO₂ emissions because of the limited carbon content per unit energy of the fuel when burned. The high oxygen content in ethanol also contributes to better combustion when tested over the WLTP cycle, which increases CO₂ emissions, yet it is offset by the smaller amount of carbon atoms available for combustion in ethanol.

The region of highest CO₂ emissions are for binary blends of diesel and biodiesel in the region of B10. Increasing the binary blend between diesel and biodiesel

beyond B10, results in a reduction of CO₂ emissions of less than 270 g/km. The higher oxygen content in biodiesel promotes complete combustion which results in an increase of CO₂ emissions. The majority of ternary blends between diesel, biodiesel and ethanol resulted in CO₂ emissions between 225 g/km and 270 g/km. An increase in CO₂ emissions towards binary blends between diesel and biodiesel as well as a reduction in CO₂ emissions towards binary blends between diesel and ethanol were also reported in other literature [43, 123, 124].

4.3.2 Evaluation of CO emissions

The quadratic model developed for CO emissions as fitted based on the mixture design corresponds to:

$$\begin{aligned} Z_{CO} = & x_D - 35.34 \times x_B + 70.00 \times x_E \\ & + 44.7 \times x_D \times x_B - 79.86 \times x_D \times x_E \\ & - 13.78 \times x_B \times x_E \end{aligned} \quad (4.6)$$

where Z_{CO} is the CO emissions in the exhaust gas in grams per kilometer and the variables x_D , x_B and x_E are the fraction percentages of the components in the overall fuel blend. The effect of all the linear terms as well as the diesel/biodiesel and diesel/ethanol quadratic terms were found to be significant on CO emissions with $p < 0.02$.

Other terms such as the interaction between biodiesel and ethanol did not have a significant effect on CO emissions as indicated by $p = 0.249$. Furthermore, the regression statistics goodness of fit (R^2) and the goodness of prediction (adjusted R^2) showed high values of 98.65% and 97.81% respectively for the presented model indicating a high correlation between the observed and the predicted values of CO emissions. The variation of CO emissions response with fuel blends based on the model developed from DoE is shown in Figure 4.4. As shown in the figure, there is an area of CO emissions less than 0.85 g/km for a binary blend of diesel and ethanol between approximately E2 and E10. The decrease in CO emissions can be contributed to an improved oxidation process which is possible due to the fact that ethanol has a high oxygen content. Figure 4.5 shows a time series plot for CO emissions of two blends (diesel and B3E14) with the WLTP drive cycle shown in dashed lines. B3E14 has lower CO emissions over the whole of the WLTP compared to diesel. The difference is more pronounced during idling scenarios in the WLTP (0 km/h). The difference becomes less during high speed scenarios, especially between 1000 s and approximately 1400 s. The reduction in CO emissions is a result

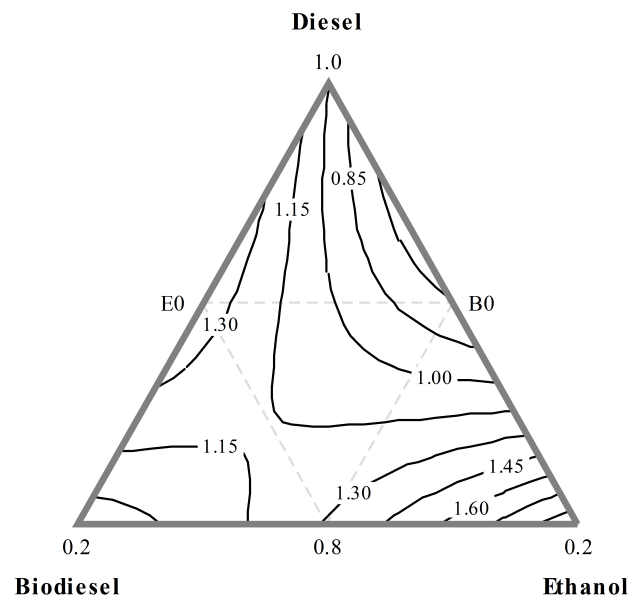


Figure 4.4: Contour plot of the engine response over the WLTP for CO emissions in grams per kilometer [41].

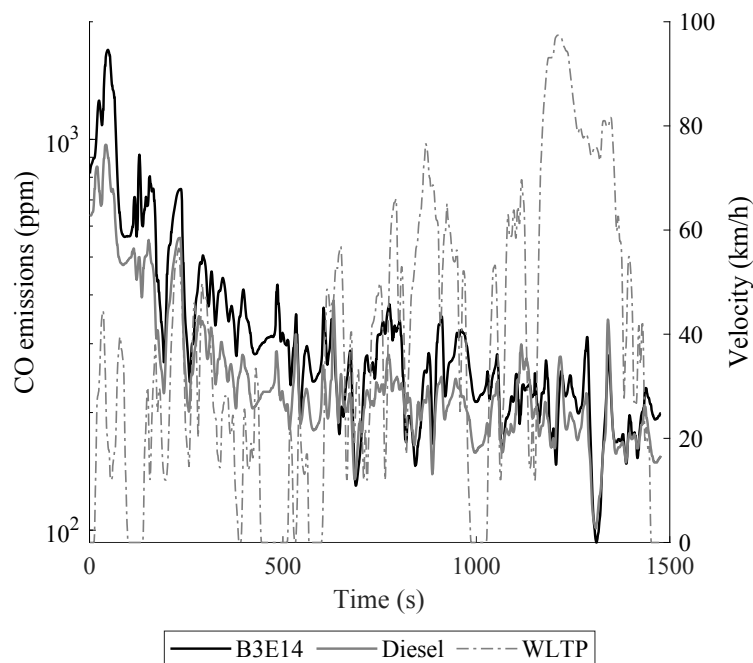


Figure 4.5: CO emissions comparison between B3E14 and diesel.

of improved combustion due to the additional oxygen content in B3E14 which is beneficial especially during idling scenarios when the mixing of the fuel and air is

reduced as a result of the low speed and low load of the engine.

Figure 4.4 also shows that for high concentrations of ethanol (>15%) in the fuel blend, can result in CO emissions higher than 1.6 g/km. Similar studies [45, 120] have also found that for high percentages of ethanol in binary blends, the ignition delay can be increased due to the low cetane number of ethanol which causes the fuel to resist auto-ignition in diesel engines and inhibit complete combustion. The cooling effect of the ethanol on the gas temperature due to ethanol's high latent heat of evaporation can also influence the oxidation process, even though enough oxygen is available for combustion [34]. This is also evident for ternary blends with a high percentage of ethanol. In Figure 4.4 CO emissions increase for binary blends between B5 and B15 and then start to decrease again for percentages of higher blends above approximately B16 [125]. At low engine loads, biodiesel can negatively influence the atomisation of the fuel, which results in poor combustion. Binary blends of diesel and biodiesel less than B20 reduce CO emissions by a small amount at low engine loads and the reduction becomes more pronounced at high load scenarios. The higher oxygen content present in the fuel for higher percentages of biodiesel improves combustion of the fuel. For blends of biodiesel greater than B20, CO emission reduction is more pronounced at low engine loads [39, 126]. Engine operating conditions as well as oxygen content of the fuels play a significant part in the formation of CO emissions [45, 123]. The engine operates more regularly in the low and medium load regions when tested over the WLTP, which results in minor CO emission changes for binary blends of diesel and biodiesel.

For ternary blends, small additions of biodiesel and ethanol will decrease the engine's CO emissions. A maximum addition of B5E5 will result in similar CO emissions compared to using just diesel.

4.3.3 Evaluation of NO_x emissions

The quadratic model developed for NO_x emissions as fitted based on the mixture design corresponds to:

$$\begin{aligned} Z_{\text{NO}_x} = & 1.13 \times x_D - 1.19 \times x_B + 8.97 \times x_E \\ & + 2.50 \times x_D \times x_B - 10.13 \times x_D \times x_E \\ & + 0.33 \times x_B \times x_E \end{aligned} \quad (4.7)$$

where Z_{NO_x} is the NO_x emissions in the exhaust gas of the engine in grams per kilometer. Both the linear and the quadratic models in Equation 4.7 are significant with $p < 0.02$. Interaction between the diesel and ethanol terms is significant with

$p < 0.02$ whereas the interaction between the diesel and biodiesel terms and the biodiesel and ethanol terms are not significant. High values of R^2 (88.24%) and adjusted R^2 (80.89%) respectively for Equation 4.7 indicated that there is a high correlation between the observed and the predicted response of the engine. The variation of NO_x emissions response with fuel blends based on the model developed from DoE is shown in Figure 4.6. A low NO_x emissions region is evident for binary

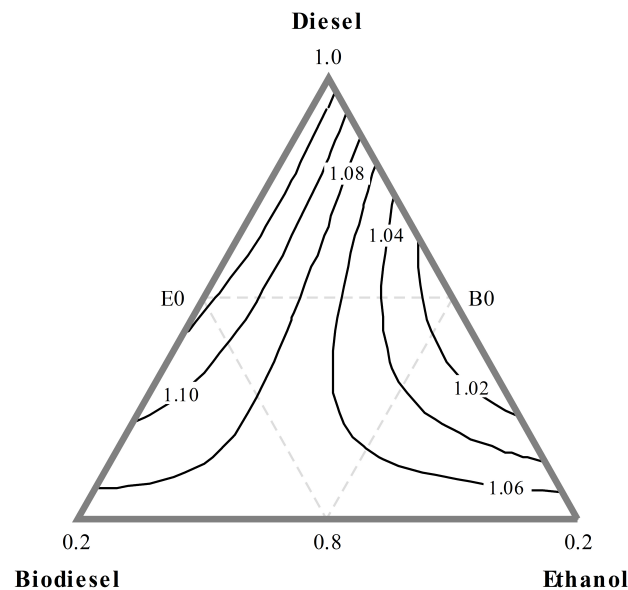


Figure 4.6: Contour plot of the engine response over the WLTP for NO_x emissions in grams per kilometer [41].

blends between diesel and ethanol of approximately E7 to E15. The decrease in NO_x emissions for binary blends between E7 and E15 can be attributed to ethanol's high latent heat of evaporation which decreases the combustion temperature as well as NO_x formation [40]. Figure 4.7 shows a time series plot for NO_x emissions of two blends (diesel and B3E14) with the WLTP drive cycle shown in dashed lines. For the majority of the WLTP drive cycle, the NO_x emissions for the two blends are similar. Differences occur during idling scenarios in the WLTP as well as at the start of the WLTP. The lower NO_x emissions at idling can be contributed to the cooling effect of the ethanol in the blend, which reduces the combustion temperature and as such the formation of NO_x emissions. The difference in NO_x emissions at the start of the drive cycle, when the engine is still cold, is also caused by the ethanol in the blend reducing combustion temperatures.

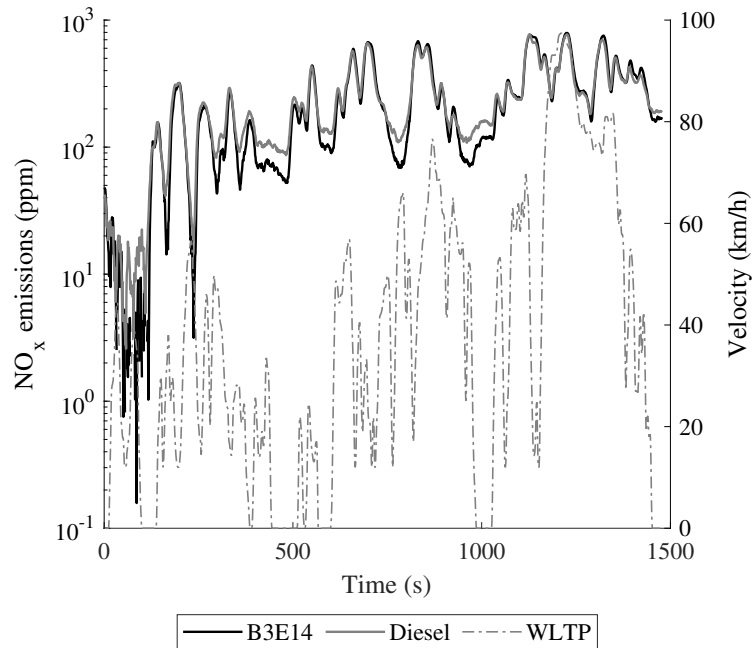


Figure 4.7: NO_x emissions comparison between B3E14 and diesel.

Increasing the ethanol content beyond E15 results in NO_x emissions increasing due to ethanol influencing the combustion characteristics (increased ignition delay) of the engine as well as lowering the cetane number of the fuel blend considerably [34, 120].

A ternary blend between diesel, biodiesel and ethanol manages to achieve an equilibrium between the effects of better combustion due to the higher oxygen content in biodiesel and ethanol, as well as the advanced injection of the fuel because of biodiesel's increased bulk modulus. This can be seen in Figure 4.6 where there is a plateau of NO_x emissions between 1.06 g/km and 1.08 g/km for ternary blends with $x_D = 0.8$.

4.3.4 Evaluation of fuel consumption

The quadratic model developed for fuel consumption as fitted based on the mixture design corresponds to:

$$\begin{aligned}
 FC = & 119 \times x_D + 166 \times x_B - 268 \times x_E \\
 & - 18 \times x_D \times x_B + 586 \times x_D \times x_E \\
 & - 1333 \times x_B \times x_E
 \end{aligned} \tag{4.8}$$

where FC is the fuel consumed by the engine when run over the WLTP in grams per kilometer. The linear model is significant with $p < 0.02$ and the interaction

terms approaches statistical significance with $p = 0.078$. Of the three interaction terms of the quadratic model, only the interaction between biodiesel and ethanol are deemed significant with $p = 0.03$. High values of R^2 (87.48%) and adjusted R^2 (79.65%) respectively for Equation 4.8 show that there is a high correlation between the observed and the predicted response of the engine. The variation of the engine's fuel consumption over the WLTP with fuel blends based on the model developed from DoE is shown in Figure 4.8. The region of minimum fuel consumption of less

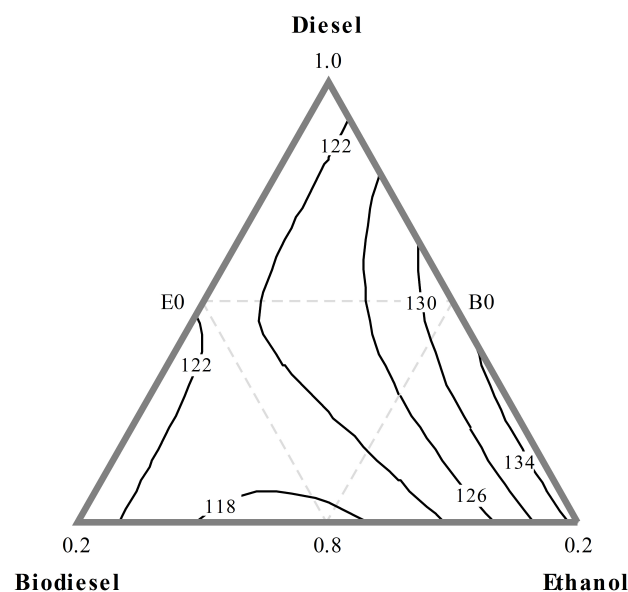


Figure 4.8: Contour plot of the engine response over the WLTP for fuel consumption in grams per kilometer [41].

than 118 g/km is achieved when approximately 10% biodiesel and 10% ethanol are blended with diesel. This region of improved fuel consumption can be attributed to better fuel atomisation as a result of the ethanol in the fuel. The additional oxygen from the biodiesel and ethanol in the blend also contributes to improved combustion and better fuel economy. A plateau region for fuel consumption between 118 g/km and 122 g/km is evident for most of the binary blends between diesel and biodiesel as well as ternary blends with $x_E \geq 3\%$. High concentrations of ethanol in binary blends between diesel and ethanol ($x_E \geq 7\%$) and in ternary blends with the percentage ethanol in the blend being higher than 15%, results in fuel consumption of more than 126 g/km. The increase in fuel consumption when ethanol is increased in the blend has also been reported in other literature [118]. An increased concentration of ethanol

in the blend reduces the energy content of the blend, which causes fuel consumption of the engine to rise. This is also true for binary blends between diesel and biodiesel with biodiesel content higher than 10%. The biodiesel has a lower heating value compared to diesel and as the content of biodiesel increases in the fuel blend, so does the fuel consumption [28, 123, 127]. The increase in fuel consumption was minimal for concentrations of $x_B \leq 0.1$, but became significant for higher concentrations of biodiesel in the fuel blend. The plateau region for ternary blends in Figure 4.8 is also reported in other literature [38] where small percentages of ethanol in the ternary blend does not contribute significantly to the fuel consumption increase. With higher concentrations of ethanol in the ternary blend, the fuel consumption increases significantly [34].

4.3.5 Mixture optimisation

4.3.5.1 Optimising towards a binary blend

It is important to state from the outset of the discussion that the following analysis prioritised emissions reduction and meeting the renewable content target. Some argument could be made to accept a compromise on the engine emissions over renewable content, since exhaust after treatment systems are required to meet the Euro standards anyhow. However, it is commonly accepted that reducing the emissions at source (in the engine) has a knock-on positive effect on the whole vehicle. Since initial emissions reduction will result in a lighter, smaller and cheaper exhaust after treatment system [128].

The optimisation of the mixture is dependent on more than one engine response which include CO emissions, CO₂ emissions and NO_x emissions.

As discussed previously the addition of ethanol to diesel has a positive impact on the harmful emissions. Figure 4.9 show the variation of CO₂, NO_x and CO with increasing amounts of ethanol in diesel. The plot shows that between an ethanol content of around E5 to E15 there is generally a minimisation of all the emissions. For blends greater than E15 the emissions tend to increase rapidly compared to pure diesel. This range of minimum emissions is convenient as the latest UK target for 2020 is a renewable content of 10%. Therefore, assuming that the renewable biofuel content is fulfilled by ethanol alone compared to pump diesel a binary blend of E10 would result in a decrease of CO₂, NO_x and CO of 26%, 12% and 45% respectively. Note the comparison has been made with pump diesel, which we have assumed to have a 5% biodiesel content [129], rather than pure diesel. The reason for this is that it is now not possible to purchase pure diesel from a filling station in the UK, and so the comparison should be made with the fuel that is currently available.

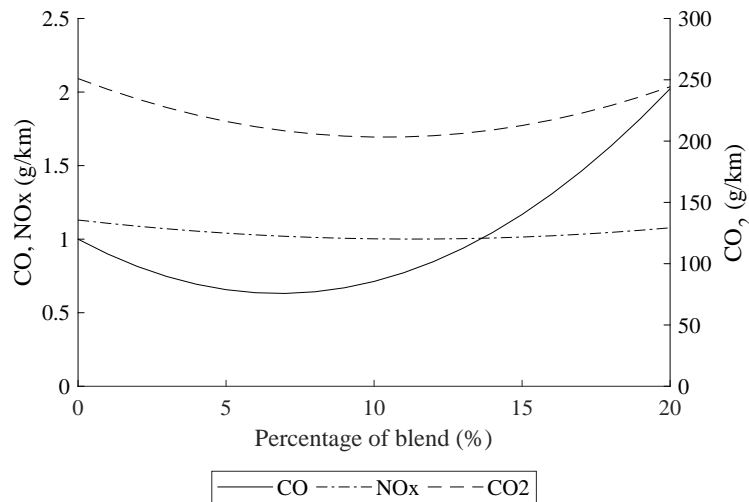


Figure 4.9: Variation of CO₂, NO_x and CO with increasing amounts of ethanol in diesel

The addition of ethanol seems positive in terms of both reducing the harmful emissions from vehicles whilst simultaneously increasing the renewable content of the fuel in line with EU targets. However, there are a number of practical issues that nullify these advantages. Firstly when considering alternative fuels for vehicles, the carbon dioxide emissions from the vehicle should not be considered in isolation. All the carbon dioxide emissions along the supply chain need to be considered.

Table 4.4 shows the equivalent carbon dioxide emissions upstream of the vehicle and are often referred to the *Well-To-Tank* (WTT) emissions. These WTT emissions include everything upstream such as extraction, refining, purification, transportation, etc. The term *equivalent* refers to processes where there is a Greenhouse Warming Potential and these are then expressed as the equivalent grams of carbon dioxide. The data in Table 4.4 shows that the equivalent carbon dioxide emissions for pump

Table 4.4: Comparison of equivalent carbon dioxide Well-To-Tank emissions for diesel and renewable fuels. [130]

Fuel	gCO ₂ e/Litre	Percentage change
Pump Diesel	618.46	—
Ethanol (1st generation)	613.77	−1%
Ethanol (2nd generation)	426.08	−31%
Biodiesel (RTFO average)	312.95	−49%

diesel are similar compared to first generation ethanol. This means that the net carbon dioxide saving of using ethanol comes from the displaced diesel fuel in the tank and the emissions saving from the combustion process, but there are not any upstream savings. If second generation ethanol was to be used, then there will also

be a WTT CO₂ saving, with second generation ethanol generating approximately 31% gCO₂e/Litre less in WTT emissions compared to pump diesel (Table 4.4).

However, a more pressing technical barrier for a binary mixture of ethanol and diesel is that ethanol is immiscible in diesel (discussed in Section 1.2.5 and Section 4.2.3). Therefore additives (emulsifiers) are required to improve the miscibility of the ethanol in the diesel [39, 117]. Biodiesel can act as an emulsifier for ethanol.

The addition of biodiesel also has the added benefit that it has a much lower WTT carbon dioxide emissions compared to ethanol (Table 4.4). Based on current figures the WTT carbon dioxide emissions are around half that of regular pump diesel and first generation ethanol [130].

Consequently, based on the reduced WTT carbon dioxide emissions it would be best to meet the renewable targets with biodiesel alone. However, the addition of biodiesel tends to increase emissions. Figure 4.10 shows the variation of CO₂, NO_x and CO with increasing amounts of biodiesel in diesel. Figure 4.10 shows that for

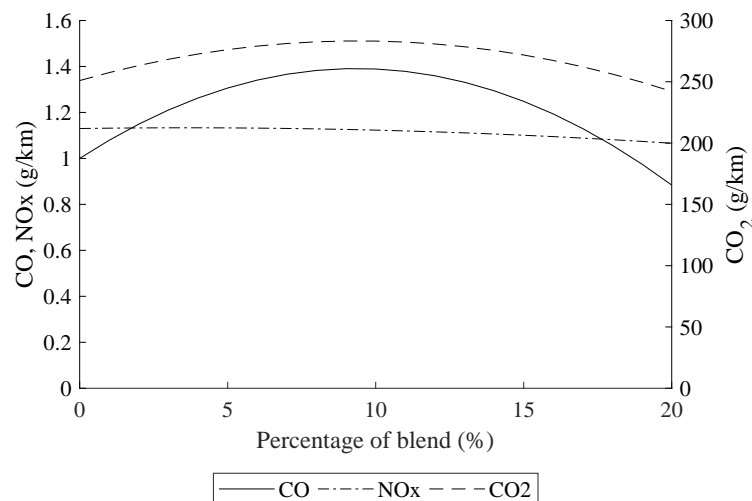


Figure 4.10: Variation of CO₂, NO_x and CO with increasing amounts of biodiesel in diesel

biodiesel blends between B5 and B15 the CO and CO₂ emissions are at a maximum. This is caused by poor atomisation of the fuel and poor mixing of the fuel and air at low engine power. If the renewable fuel target of 10% is fulfilled with biodiesel, then compared to pump diesel, this would result in an increase of CO and CO₂ of 6.3% and 2.5% respectively, whilst a decrease in NO_x of 0.9%.

The changes are modest compared to pump diesel. The reason for this modest increase is because the comparison is with pump diesel, which already has a biodiesel content of 5%. There is an argument that, when considering how best to meet the future renewable targets, the *well-to-wheel* (WTW) CO₂ emissions need to be considered. The WTW emissions consider the carbon dioxide emissions generated from all the upstream processes and the emissions from the vehicle itself.

To address the conflicting requirements of decreasing the WTW CO₂ emissions, additional exhaust harmful emissions and practical miscibility aspects of the fuel a ternary blend of diesel, biodiesel and ethanol is required. The proposed criteria for the fuel is:

- A renewable biofuel content of 10% to meet the 2020 UK target.
- Minimise the well-to-wheel CO₂ emissions.
- Minimise the harmful emissions of carbon monoxide and nitrogen oxides.
- A homogeneous mixture that will not separate.

To minimise the WTW CO₂ emissions the maximum amount of biodiesel is required. To minimise the harmful emissions the maximum amount of ethanol is required.

4.3.5.2 Optimising towards a ternary blend

The desirability approach was used for the optimisation of the mixture parameters (diesel, biodiesel and ethanol) for the properties of the engine response (CO emissions, CO₂ emissions and NO_x emissions). The software transforms each response to a dimensionless desirability value d . The value ranges from $d = 0$, which indicates that the response is unacceptable, to $d = 1$ which shows that the response is more desirable. The goal of this study was to minimise all engine emissions and the desirability of each of the responses was calculated using [131]:

$$d_i(\hat{Y}_i) = \begin{cases} 1 & \text{if } \hat{Y}_i(x) < T_i \\ \frac{\hat{Y}_i(x) - U_i}{T_i - U_i} & \text{if } T_i \leq \hat{Y}_i(x) \leq U_i \\ 0 & \text{if } \hat{Y}_i \geq U_i \end{cases} \quad (4.9)$$

where $d_i(\hat{Y}_i)$ is the desirability function of response $\hat{Y}_i(x)$, T_i and U_i are the target and upper values respectively that are desired for response $\hat{Y}_i(x)$. For minimising the response, T_i will denote a small enough value for the response. The individual desirability functions are combined using the geometric mean, which gives the overall desirability:

$$D = (d_1(Y_1)d_2(Y_2))^{0.5} \quad (4.10)$$

It is noticeable that if any response $d_i(\hat{Y}_i)$ is completely undesirable, $d_i(\hat{Y}_i) = 0$, then the overall desirability is zero.

As there is more than one response to be optimised, it is necessary to set requirements for each response, that the optimisation tool will optimise towards. For

each response, an upper and lower value is required. If the response needs to be minimised by the optimisation tool, the lower limit is given as the target to optimise towards. The lowest and highest values of each response from the tests conducted (Table 4.2) were taken and set as limits for the optimisation tool. All lower and upper limits used by the optimisation tool can be seen in Table 4.5. Figure 4.11 shows

Table 4.5: Optimisation lower and upper limits.

Engine emissions	Lower limit	Upper limit
CO (g/km)	0.889	1.990
CO ₂ (g/km)	232	258
NO _x (g/km)	1.04	1.15
Fuel consumption (g/km)	116	136

the desirability plot when optimising towards a reduction in all engine emission responses. The plotted lines are known as the prediction lines of the different engine

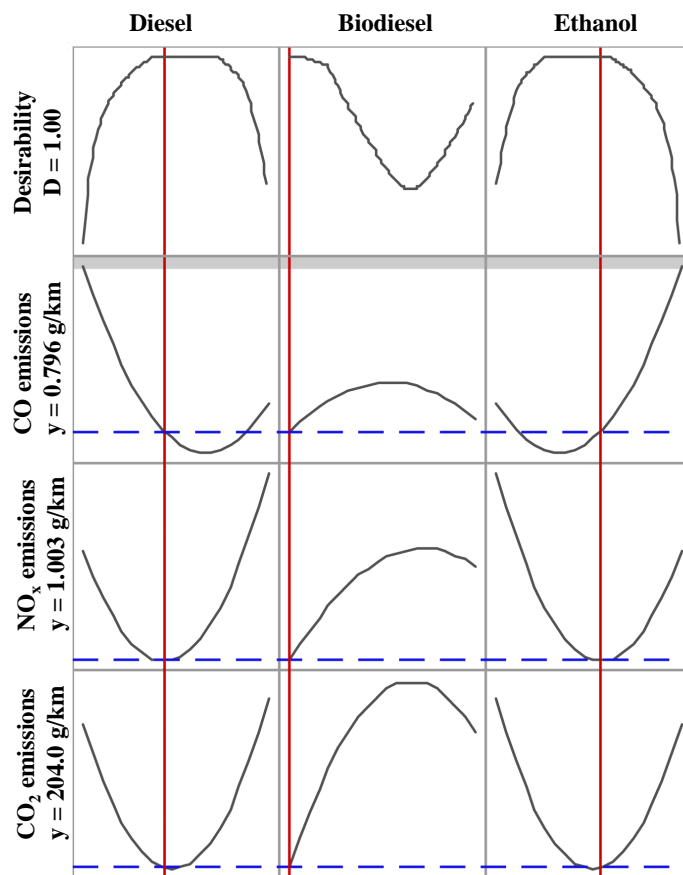


Figure 4.11: Optimisation plot for engine emissions for the fuel blend E11.

emissions. The vertical solid lines for each variable is the current blend ratio setting. By changing the vertical solid line for each blend fraction, the horizontal dashed lines were updated by re-computing the predicted engine emissions for the new blend fraction between diesel, biodiesel and ethanol. The horizontal dashed lines show the final predicted engine emissions according to the blend fractions. The optimisation gives a blend of E11 with the highest desirability percentage of 100%.

Based on previous experience the minimum amount of biodiesel to form a homogeneous mixture of ethanol, biodiesel and diesel is 2%. A previous mixture of B3E14 resulted in a stable blend. Other research has also found ternary blends of B10E20 to be stable [100]. A blend ratio of 1 : 5 between biodiesel and ethanol will ensure a homogeneous mixture. Therefore a mixture of B2E9 is proposed. The predicted reduction in emissions for CO₂, NO_x and CO are 21%, 9.7% and 34%. Table 4.6 compares the changes in emissions for each mixture compared to pump diesel.

The proposed optimum mixture requires a 9% content of ethanol and the EU target caps the ethanol from crops (first generation) to 2%. Currently 100% of the UK ethanol is first generation. Second generation ethanol has a much higher WTT CO₂ saving compared to first generation ethanol (Table 4.4). Therefore, to ensure a high WTT CO₂ saving for B2E9, investment into second generation ethanol sources are required.

Table 4.6: Summary of results showing the change in emissions compared to pump diesel

Fuel Blend	CO ₂	NO _x	CO
E10	-26 %	-12 %	-45 %
B10	2.5 %	-0.9 %	6.3 %
B2E9	-21 %	-9.7 %	-34 %

4.4 Closing remarks

This study investigated the effect of fuel blends between diesel, biodiesel and ethanol on the emission characteristics of a diesel engine tested over the World Harmonised Light vehicle Test Procedure (WLTP). Based on a mixture DoE, 7 different fuel mixtures between diesel, biodiesel and ethanol were formulated and 14 randomised runs were designed, including one replicate of each test to evaluate the reproducibility and the lack-of-fit of the derived models. It was shown that:

1. The optimum mixture to meet the UK biofuel content of 10% in 2020 based on this research is B2E9. The use of B2E9 will also reduce NO_x emissions and CO emissions in older diesel cars currently on the road that do not necessarily have modern after treatment system installed.
2. The addition of ethanol to the mixture can reduce CO emissions, but higher concentrations of ethanol in the blend reduces the cetane number of the fuel blend, which negatively impacts combustion and increases CO emissions. The addition of higher concentrations of biodiesel of more than 15% to the mixture will also reduce CO emissions. Lower concentrations of biodiesel have a smaller effect on CO emissions at low engine loads and can even increase CO emissions as a result of biodiesel's poor atomisation properties.
3. Engine CO_2 emissions are reduced with the addition of ethanol to the fuel blend. The low hydrocarbon atomic ratio of ethanol results in a reduced carbon content per unit energy of the fuel which reduces CO_2 emissions. The high oxygen content in ethanol also contributes to better combustion, which increases CO_2 emissions, yet it is offset by the smaller amount of carbon atoms available for combustion in ethanol. The higher oxygen content in biodiesel also promotes complete combustion which results in an increase of CO_2 emissions for blends that include biodiesel.
4. The increase in NO_x emissions for blends with biodiesel is a result of increased combustion temperatures due to the higher oxygen content in biodiesel. The increase is also associated by the advancement of the injection timing, caused by the higher bulk modulus of compressibility of biodiesel. The decrease in NO_x emissions for blends with ethanol is contributed to ethanol's high latent heat of evaporation which decreases the combustion temperature as well as NO_x formation.
5. An increased concentration of ethanol in the blend reduces the energy content of the blend, which causes fuel consumption of the engine to rise as well as

the running cost of the vehicle. This is also true for binary blends between diesel and biodiesel. This will not be a problem if incentives are put in place by government for the use of fuel with an increased biofuel content.

6. From a carbon dioxide reduction viewpoint a binary mixture of B10 would be best, due to the low well-to-tank emissions of biodiesel. However, increasing the biofuel content in the range B5 to B15 maximises the harmful exhaust emissions.
7. From a harmful emissions reduction viewpoint a binary mixture of E10 would be best, due to the minimisation of carbon monoxide and nitrogen oxides in the range of E5 to E15. However, ethanol is immiscible in diesel and for practical reasons biodiesel needs to be added as an emulsifier.
8. To achieve the optimum mixture, investment into second and third generation ethanol is required.
9. This work demonstrated that the mixture DoE is a useful tool to quantify the effect of fuel mixtures between diesel, biodiesel and ethanol on the engine's emissions response. It is also useful to determine the optimum fuel blend that will meet the researcher's criteria.

Chapter 5

Emissions reduction using low temperature combustion

This chapter contributes to the determination of an optimised engine operating envelope that demonstrates the use of low temperature combustion (LTC) to reduce regulated emissions when tested over the WLTP legislative drive cycle. This will be done through the use of a simulation as well as experimental tests. In using a simulation, it is demonstrated that engine models can be used to test and evaluate new engine technologies successfully to aid in the rapid transition towards low emission vehicles. Experimental data is generated and compared with the results from the simulation to further demonstrate this. The results obtained show that it is possible to decrease engine emissions with the use of low temperature combustion techniques. The results also illustrate that with the combined use of ternary fuel blends and LTC, engine manufacturers are able to meet the stringent emission standards of the EU.

Initially an investigation is presented into the calibration of the simulation to successfully simulate low temperature combustion as well as how it was set up to determine the engine operating points for reduction in regulated emissions. The results of the simulated characterisation tests as well as of the experimental results are interpreted and a final optimised engine operating envelope is calculated.

5.1 Introduction

The European Union (EU) has implemented emission standards to reduce the environmental impact of road transport. These measures include the Euro 6 legislation, which enforces limitations on harmful gasses in vehicle exhaust. Viable after-treatment systems are available to meet the new emission limits, but higher costs, durability issues, fuel economy penalties and ever-increasing space requirements limit the widespread adoption of the devices. As a result, improvements to in-cylinder strategies to further reduce the engine-out emissions to decrease the burden put on after treatment systems, are of great interest [132]. Low temperature combustion (LTC) is a promising combustion concept that can successfully reduce in-cylinder emissions resulting in the significant reduction in after-treatment dependencies [128]. For this research, LTC is defined as *combustion concepts where the overall goal is to achieve a reduction in peak combustion temperature*. The reduction of peak combustion temperatures can be achieved by the use of exhaust gas recirculation (EGR) as discussed in section 1.2.6.

This chapter investigates emission reduction with the use of simulated and experimental engine tests to optimise LTC techniques in a diesel engine while being tested over the WLTP drive cycle. PN emissions and PM emissions will be included in this study as well, as the Pegasor M-sensor (more information in Section 2.3.4.3) has been acquired at this stage of the research. Design of Experiments (DoE) will be used to characterise the response of the diesel engine and determine the parameters that significantly contribute to emission reduction. The statistical tool can be used to determine the operating parameters that result in the largest reduction in engine emissions over a given drive cycle. DoE allows for the investigation of multiple factors and their effect on engine performance and emissions. The levels of the factors are changed simultaneously, rather than one at a time. This contributes to a cost and time saving [114, 133]. The use of DoE is appropriate as other studies have used it successfully to investigate the effects between injection timing, injection pressure and nozzle tip protrusion on emission characteristics [134], to analyse the role of the injection system parameters on engine emissions, noise and fuel consumption [135] and to determine the optimum engine design and operating parameters [136].

5.2 Experimental set-up

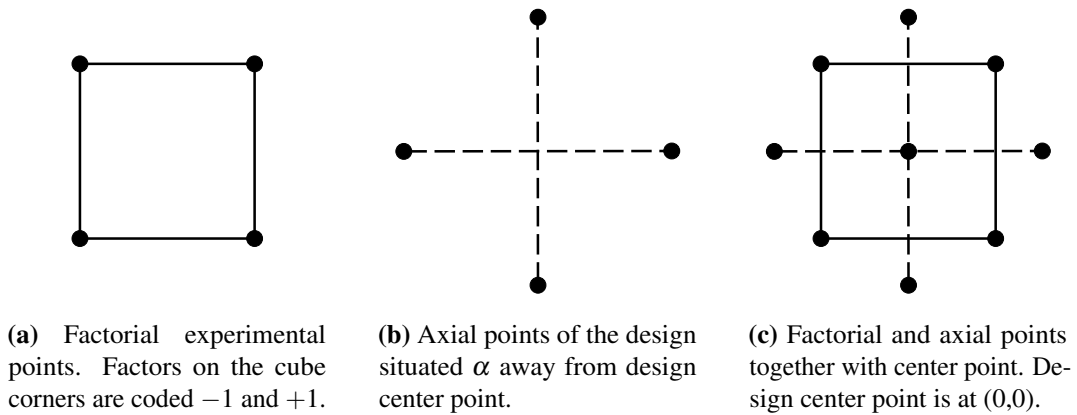
The following subsections explore the set-up of the Response Surface Method (RSM). The physiochemical properties of B2E9 are listed in Table 5.1.

Table 5.1: Physiochemical properties of B2E9.

Fuel property	Value
Cetane number	51.7
LHV (MJ/kg)	42.8
Density at 15 °C (kg/m^3)	831.1
Viscosity at 40 °C (mm^3/s)	2.686

5.2.1 Experimental design set-up

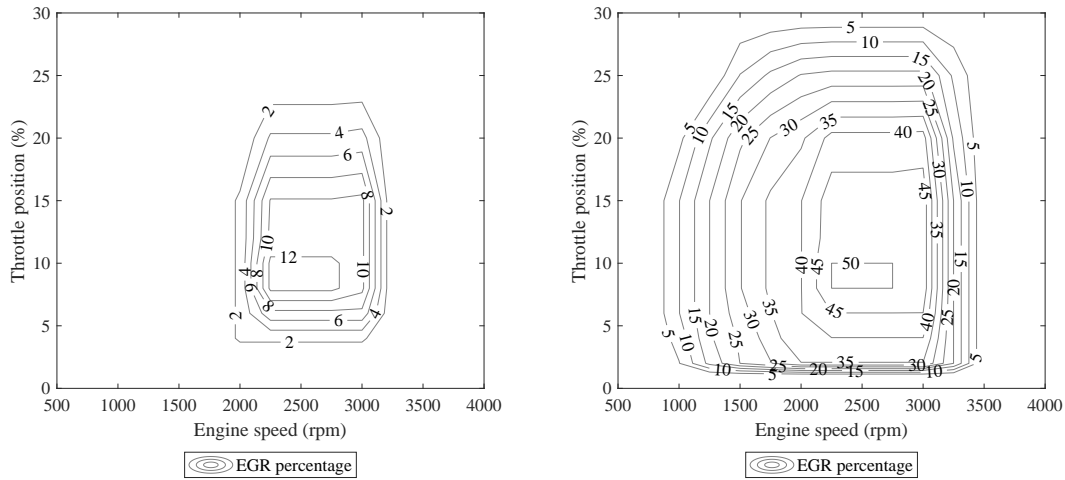
Four engine operating variables were considered for this study. They include EGR percentage, main injection start of injection (SOI), pilot injection SOI and pilot injection duration. The engine responses include CO emissions, CO₂ emissions, NO_x emissions and particulate mass (PM) and particulate number (PN). A 2⁴ central composite design (CCD) was employed for the present study to obtain the experimental data, which will fit full second-order polynomial models representing the response surfaces. Figure 5.1 shows a schematic of what a CCD is composed of. The total number of experimental points in a CCD was calculated by the following

**Figure 5.1:** Central Composite Design [133]

equation:

$$N = 2^k + 2k + n_0 \quad (5.1)$$

where N is the number of experimental runs, k is the number of independent variables and n_0 is the number of central points. In Equation 5.1, 2^k is known as the factorial experimental points, $2k$ as axial points and n_0 as replicates of the center point. Factorial experimental points allow clear estimates of all main effects and interaction effects. The axial points allow the estimation of the pure quadratic effects. Centre points are designed to be run together with both the factorial points and the axial



(a) ECU map for a maximum EGR percentage of 12.5%.

(b) ECU map for a maximum EGR percentage of 50%.

Figure 5.2: ECU maps for different EGR percentages used in the RSM [60].

points and their replication enable the estimation of the experimental error of the RSM. For this RSM, $k = 4$ and will consist of sixteen factorial points, eighth axial points and 6 central points. A total of 30 runs will be used to analyse the data acquired from the experimental runs.

The minimum and maximum ranges of independent variables were considered and the full experimental plan with their values in un-coded and coded forms is listed in Table 5.2. The values for the EGR percentages shown in Table 5.2 indicate

Table 5.2: Independent variables and their levels for a central composite design RSM.

Independent variable	Variable levels				
	-2	-1	0	1	2
EGR (%)	0	12.5	25	37.5	50
θ_{minj} - Main SOI offset (CAD)	-6	-3	0	3	6
θ_{pinj} - Pilot SOI offset (CAD)	5	9	13	17	21
$\Delta\theta_{pinj}$ - Pilot duration (%)	5	16	27	38	49

the maximum EGR percentage of the operating map. Examples of EGR maps that were generated for 12.5% and 50% EGR percentages can be seen in Figure 5.2. The maximum operating point of 50% was chosen as that was the maximum amount of EGR employed by the engine's ECU before testing started. Other published literature also investigated values of EGR in the region of 50%. [48, 49, 137]. Zheng *et al.* [48] found that increasing the EGR percentage above 65% for steady-state tests on a single cylinder engine, results in cycle-to-cycle variability. Asad and Zheng [49]

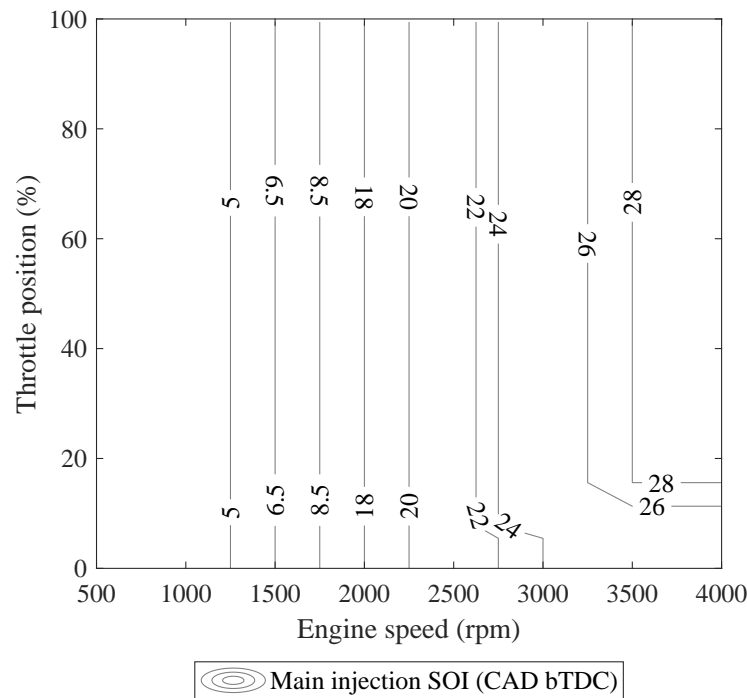


Figure 5.3: Baseline ECU map for the main injection SOI.

also concluded that the use of high percentages of EGR and high boost pressures are challenging. Engines with conventional turbochargers struggle to produce high boost and high EGR at the same time, especially at low loads. Higher boost levels require more of the exhaust to be diverted to the turbine. However, higher EGR percentages require more of the exhaust gases to be re-introduced into the intake manifold. As such, low diesel exhaust temperature at low loads places limits on the practically achievable boost pressure. Also, by investigating higher values of EGR would influence the operation of the turbocharger and ultimately influence the repeatability of the tests on the engine test cell. The limitation of the maximum EGR percentage to 50% and using the layout of the default ECU map for the EGR operation is thus acceptable.

The current ECU map for the main injection start of injection (SOI) will be used to investigate the effect of changing the SOI of the main injection. The ECU map can be seen in Figure 5.3. The main injection SOI baseline map shown in Figure 5.3 will be changed according to the values shown in Table 5.2. By adding values to the baseline main injection SOI map, the main injection SOI will become more advanced and by subtracting values from the baseline map, the main injection SOI will become more retarded.

The operating map that will be used for the pilot injection SOI will be generated using the main injection SOI and offsetting it with the values indicated in Table 5.2.

This can be calculated with the following equation:

$$\theta_{pinj} = \theta_{minj} + offset \quad (5.2)$$

where θ_{minj} and θ_{pinj} is the main injection and pilot injection SOI. The bigger the offset, the earlier the pilot injection SOI is compared to the main injection SOI. This method of determining the pilot injection SOI was taken from published work by Beatrice *et al.* [100] and Biswas *et al.* [55]. By using an offset value, it is possible to investigate the effect of dwell time of the fuel delivered through the pilot injection on emissions. Other research done by Carlucci *et al.* [56] and Zhang *et al.* [57] investigated the pilot injection SOI relative to top dead center (TDC). This method will not be effective in determining the effect of the dwell time of the fuel delivered through the pilot injection, as the main injection SOI is also changing and an advanced pilot injection relative to TDC can still have a small dwell time due to an advanced main injection. The method of offsetting the pilot injection SOI relative to the main injection SOI is thus acceptable.

The pilot duration in Table 5.2 is shown as a percentage of the total fuel being delivered to the engine. As the percentage of fuel introduced with the pilot injection increases, the fuel delivered through the main injection decreases accordingly. This is to ensure that the total amount of fuel entering the cylinders stay the same. The total injector open time for the whole operating envelope of the engine as a function of throttle position and engine speed was determined by adding the default ECU maps for the main injection duration and the pilot injection duration together. The summation is shown in Figure 5.4. The pilot injection duration is calculated from the the map shown in Figure 5.4 with the following equation:

$$\Delta\theta_{pinj} = x_{pinj}\Delta\theta_{total} \quad (5.3)$$

where $\Delta\theta_{total}$ is the total injection duration and x_{pinj} is the percentage of the fuel delivered through the pilot injection as shown in Table 5.2. The main injection duration can thus be calculated by:

$$\Delta\theta_{minj} = \Delta\theta_{total} - \Delta\theta_{pinj} \quad (5.4)$$

Expressing the fuel amount as a percentage of the total fuel delivered has been done in other research as well [57, 138, 139] where multiple injections were tested and the amount of fuel delivered by each injection was expressed as a percentage of the total fuel. A visual representation of the parameters used in the central composite design can be seen in Figure 5.5.

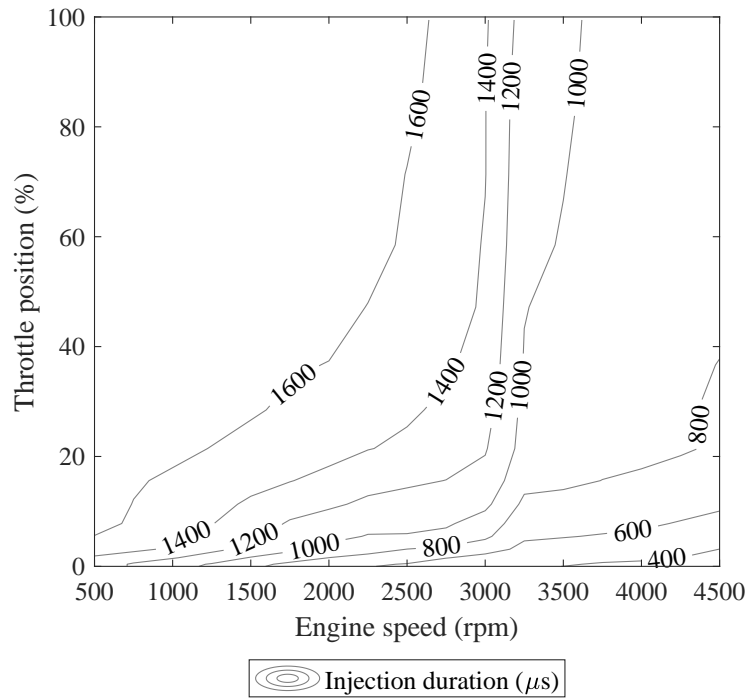


Figure 5.4: Total fuel delivered to the engine.

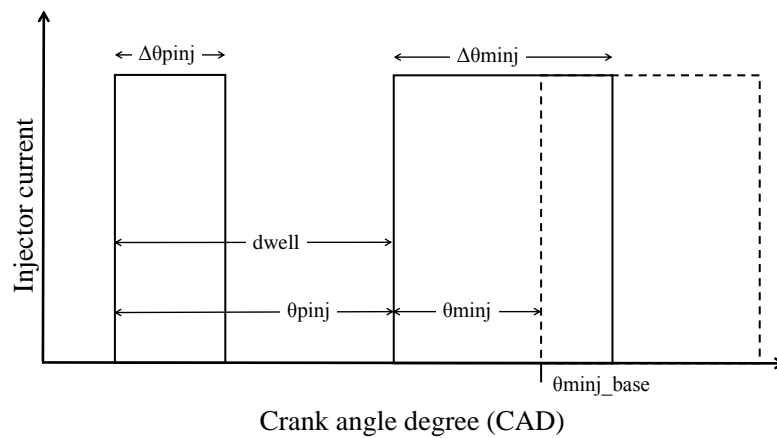


Figure 5.5: Visual representation of the parameters listed in Table 5.2

5.2.2 Co-simulation model

The following sub-sections will focus on the changes made to the simulation discussed in Chapter 3. The procedure for converting the WLTP drive cycle from a velocity profile to a load and engine speed profile will also be discussed.

5.2.2.1 WLTP drive cycle

Figure 1.1b shows the WLTP drive cycle that will be used in the simulation as well as during the experimental stages of this research. The velocity profile for the WLTP was used as given by the Commission Regulation 2017/1151 [140].

The drive cycle object in Ricardo IGNITE (Figure 3.9) was updated with the velocity profile of the WLTP. The only other sub-model that also needed to be updated was the Shift Strategy object. As opposed to the NEDC drive cycle, it is necessary to use a prescribed calculation to determine what gear to select while driving the WLTP. The calculation is based on engine speeds as well as full load power curves as a function of engine speed. The $(n/v)_i$ ratio, which is the engine speed divided by the vehicle speed in a specific gear, is calculated first:

$$\left(\frac{n}{v}\right)_i = \frac{60000r_i r_{axle}}{3.6U_{dyn}} \quad (5.5)$$

where n is the engine speed (rpm), v is the vehicle speed (km/h), r_i is the transmission ratio for gear i and r_{axle} is the axle transmission ratio. U_{dyn} is the dynamic rolling circumference of the tyre. U_{dyn} is calculated using:

$$U_{dyn} = 3.05 \left(2W \left(\frac{H}{100W} \right) \right) + 25.4R \quad (5.6)$$

The tyres used on the vehicle under consideration for this research are 195/65 R16 tyres and as such for Equation 5.6 the variables $H/W = 65$, $W = 195$ and $R = 16$. Using $(n/v)_i$ together with the full load power curve provided by the engine manufacturer, a graph can be generated that shows the maximum attainable power for each gear ratio, as seen in Figure 5.6. The required road load power as a function of vehicle speed can be calculated using:

$$P_{required} = \frac{f_0 v_{max} + f_1 v_{max}^2 + f_2 v_{max}^3}{3600} \quad (5.7)$$

where

$$f_0 = mgC_{d_w} \quad (5.8)$$

$f_1 = 0.1$ and

$$f_2 = 0.5\rho_{air}C_{d_v}A_{fr} \quad (5.9)$$

m is the testing mass of the vehicle, g is the gravimetric acceleration constant, C_{d_w} is the coefficient of drag for the tyres, ρ_{air} is the density of air, C_{d_v} is the coefficient

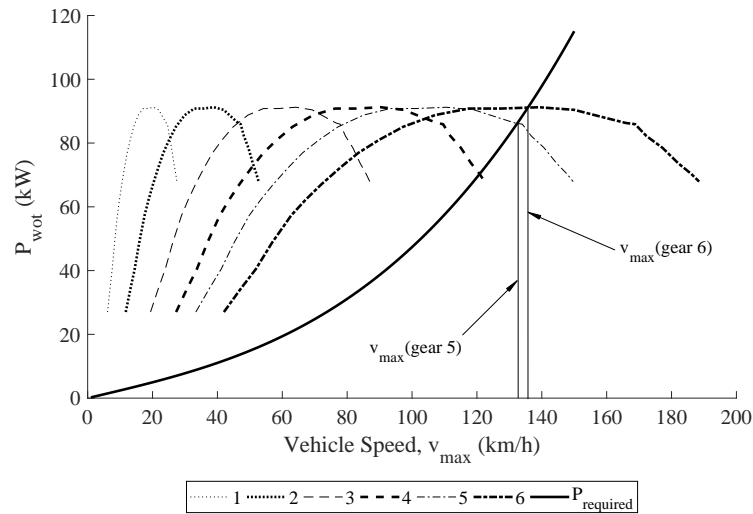


Figure 5.6: Available engine power for each gear ratio.

of drag for the vehicle body and A_{fr} is the frontal area of the vehicle. All values used are listed in Table 5.3. The required power to overcome the driving resistance

Table 5.3: Required data for engine gear selection determination.

Description	Value
P_{rated} (kW)	103
n_{rated} (rpm)	3500
n_{idle}	900
n_g	6
Road load coefficients	
Mass (kg)	3500
g (m/s^2)	9.81
C_{d_w}	0.025
ρ_a (kg/m^3)	1.189
C_{d_v}	0.4
A_{fr} (m^2)	4.6
k_r	1.03

of the vehicle is also shown in Figure 5.6. Using Figure 5.6 the gear ratio at which the maximum vehicle speed is reached, n_{gmax} , can be determined. n_{gmax} is where $v_{max}(n_g) \geq v_{max}(n_g - 1)$. When looking at Figure 5.6, the maximum vehicle speed is achieved in gear 6 and thus $n_{gmax} = 6$. Next, it is necessary to determine the minimum and maximum engine speed values that will require a down shift or an up shift. For $n_g = 1$, the minimum engine speed, n_{min_drive} will be equal to n_{idle} . Similarly, for decelerations to standstill $n_{min_drive} = n_{idle}$. For $n_g > 1$, n_{min_drive} shall

be determined by:

$$n_{min_drive} = n_{idle} + 0.125(n_{rated} - n_{idle}) \quad (5.10)$$

Equation 5.10 gives a minimum engine speed of 1225 rpm. The maximum engine speed, n_{max_drive} , is the maximum engine speed between n_{max_95} , the minimum engine speed where 95% of rated power is reached, and n_{max_6} , the maximum engine speed in gear 6 for the WLTP. At 95% engine power, the minimum engine speed is approximately 2510 rpm. The engine speed in gear 6 at the maximum velocity for the WLTP (Figure 1.1b) is 3128 rpm. For the gear selection process, $n_{max_drive} = 3128$ rpm.

Another measurement that influences the gear selection is:

$$P_{available_i,j} \geq P_{required_j} \quad (5.11)$$

where i is the gear number and j is each second in the WLTP cycle. The available power is the full load power curve, minus a 10% safety margin. The required power can be calculated using:

$$P_{required_j} = \frac{f_0 v_j + f_1 v_j^2 + f_2 v_j^3}{3600} + k_r \frac{a_j v_j T M}{3600} \quad (5.12)$$

where a_j is the vehicle acceleration at second j :

$$a_j = \frac{v_{j+1} - v_j}{3.6(t_{j+1} - t_j)} \quad (5.13)$$

The factor k_r takes the inertial resistances of the drive train during acceleration into account. The following criteria was thus used to determine which gear needs to be selected during the WLTP drive cycle:

$$n_i = \begin{cases} n_{i+1}, & \text{if } P_{available_i,j} \leq P_{required_j} \text{ and } n \geq 3128 \text{ rpm} \\ n_i, & \text{if } P_{available_i,j} \geq P_{required_j} \text{ and } 1225 \text{ rpm} \leq n \leq 3128 \text{ rpm} \\ n_{i-1}, & \text{if } n \leq 1225 \text{ rpm} \end{cases} \quad (5.14)$$

5.2.2.2 Validating Ricardo WAVE combustion model

The following section shows how Ricardo WAVE's combustion model, discussed in Chapter 3 was changed to enable the simulation of LTC with a ternary blend, B2E9. The co-simulation was set up by using and improving the validated simulation of a

2.4 litre diesel engine [111]. Improvements include:

- Improved start of combustion calculations.
- Increased controller accuracy to minimize error when following the selected drive cycle.

As mentioned at the end of Chapter 3, the validation process suffered because of the sample size of the experimental data used to validate the engine simulation. Experimental data points were taken at engine speed intervals of 250 rpm from 1500 rpm to 3250 rpm. The engine load was varied by 0.1 BMEP from 0.2 BMEP to 0.6 BMEP. This resulted in a possible 40 steady state experimental data points compared to the 9 points used in Chapter 3. Due to the inability for some data points to provide steady-state engine operating data, only 28 points were used for the validation process. The number of pressure traces that were used to obtain an average pressure trace, was increased to ≥ 100 as recommended by Lancaster *et al.* [105]. From the experimental pressure traces, the heat release traces are calculated (Equation 3.8) and subsequently the mass fraction of fuel burned during combustion (Equation 3.9) and the premixed burn fraction (Equation 3.10) are determined by fitting the equations to the heat release trace. This is shown in Figure 5.7 for two steady state engine operating points. Multiple regression equations were generated

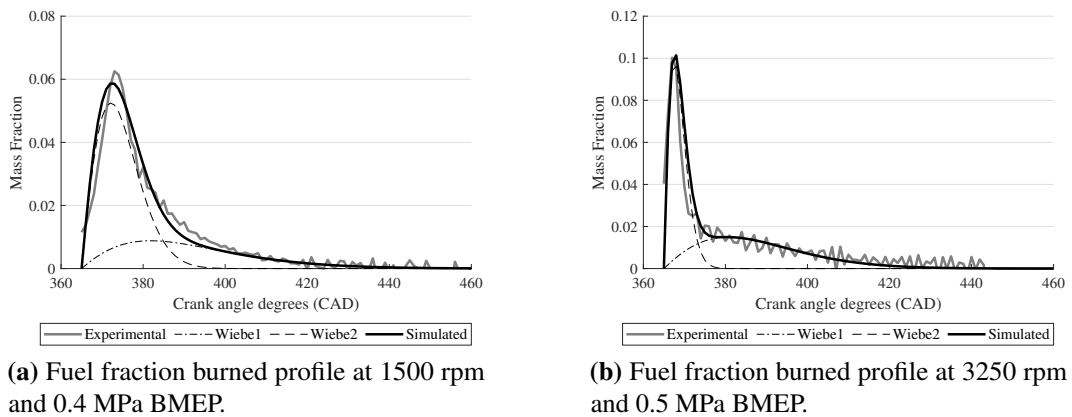


Figure 5.7: Fitting of Wiebe combustion model to experimental combustion heat release data.

for start of combustion (θ_0) and fuel mass fraction burned in the premixed combustion phase (β). This is used to determine the Wiebe combustion equation as a function of selected engine operating parameters. The equation for start of combustion (SOC) is:

$$\theta_0 = a_1 \text{EGR} + a_2 \theta_{minj} + a_3 \theta_{pinj} + a_5 \Delta \theta_{pinj} + a_6 p_0 + a_7 \quad (5.15)$$

and similarly for the fraction of fuel burned in the premixed phase (β):

$$\beta = a_1 \text{EGR} + a_2 \theta_{minj} + a_3 \theta_{pinj} + a_4 \Delta \theta_{minj} + a_5 \Delta \theta_{pinj} + a_6 p_0 + a_7 \quad (5.16)$$

where EGR is the exhaust gas recirculation percentage and θ_{minj} and θ_{pinj} are the injection timing of the main fuel injection and pilot fuel injection in degrees after Top Dead Center (ATDC). $\Delta \theta_{minj}$ and $\Delta \theta_{pinj}$ are the injection duration of the main injection and pilot injection in microseconds and p_0 is the inlet charge pressure in bar. θ_0 is in degrees ATDC and β is a percentage value. The values for the constants a_{1-7} are listed in Table 5.4. All the terms of the correlation equations generated for

Table 5.4: Constant values for Wiebe parameter regression models

	a_1	a_2	a_3	a_4	a_5	a_6	a_7
θ_0	0.09130	0.28830	-0.46900	—	-0.00750	-77.93100	81.26450
β	0.00645	0.03449	-0.01804	0.00125	-0.00101	-3.64177	3.54655

the Wiebe combustion model were found to be significant with $p < 0.02$.

A different approach was followed in implementing the equations in Ricardo WAVE, as compared to Chapter 3. In Chapter 3 the multi-Wiebe simulation tool in Ricardo WAVE was used, which required additional input values such as m_p and m_d for Equation 3.11. The Diesel Wiebe combustion model in Ricardo WAVE only requires the start of combustion as well as the premixed burn fraction to simulate the combustion event. This cuts down on computing requirements as only two regression equations are used to simulate the Wiebe combustion model, compared to Chapter 3's four equations. Figure 5.8 compares the simulated in-cylinder pressure data with the experimental data when Ricardo WAVE's Diesel Wiebe combustion model is used. The comparison shows good agreement between the simulated and experimental data. Ricardo WAVE's Diesel Wiebe combustion model is sufficient for the use in this study to investigate LTC using B2E9 fuel.

5.2.2.3 Validating Ricardo WAVE emissions model

The following section discusses how Ricardo WAVE's emission sub-models, discussed in Chapter 3, were changed to enable the simulation of LTC with a ternary blend, B2E9. The calibration of the CO and NO_x emissions is no longer accurate as the fuel has been changed from B0 to B2E9. The emission sub-models thus need to be re-calibrated using the experimental emissions data obtained during the steady-state engine operation running on B2E9.

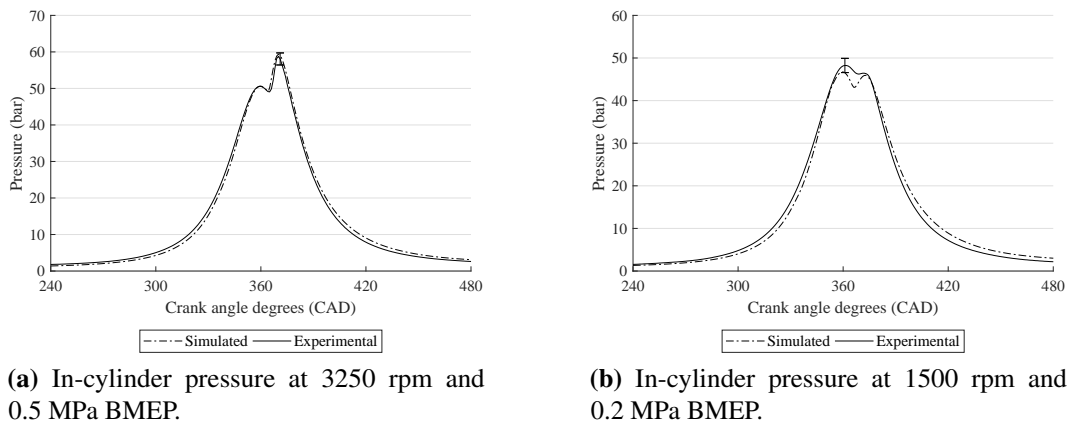


Figure 5.8: In-cylinder pressure profile comparison between steady-state experimental data and simulated data for tests with B2E9 [60].

The simulated CO emissions shown in Figure 5.9b shows good agreement with the experimental values, while the simulated CO emissions shown in Figure 5.9a has a bigger difference when compared to the experimental results. Both graphs in

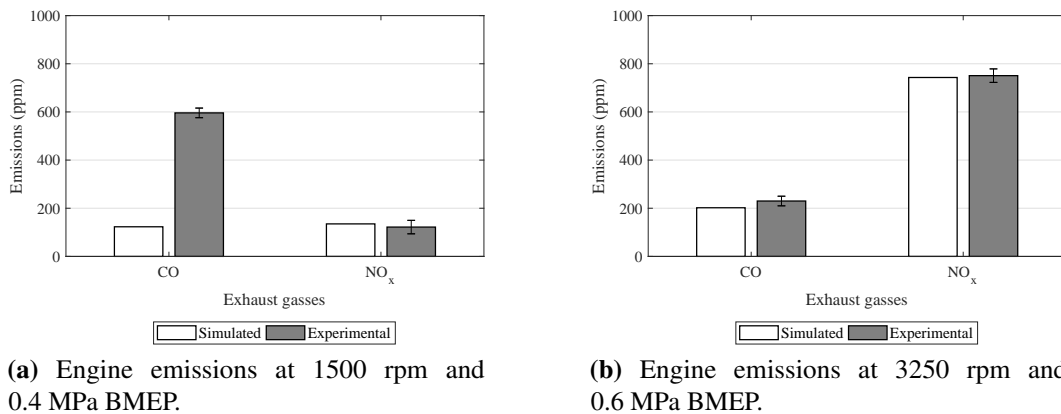


Figure 5.9: Engine emissions comparison between steady-state experimental data and simulated data for tests with B2E9 [60].

Figure 5.9 show that the simulated CO emissions is calculated less compared to the experimental values. As discussed in section 3.2.3.2 it was necessary to modify the fuel quantity delivered to ensure lower CO emissions. In the case of altering the model for using the B2E9 fuel, simulated CO emissions at higher loads show good agreement with the experimental emissions, while simulated CO emissions at lower loads differ from the experimental emissions. It can be concluded that even though the CO emissions model in WAVE compensates for both rich and lean combustion events, in this study, simulated CO emissions for lean combustion events are more accurate. Engine operating points were the majority of the combustion events are

rich will suffer in accuracy.

The NO_x emissions model in Ricardo WAVE was calibrated using the same method as described in Section 3.2.3.2. The value of the user-defined values for ARC_1 and AERC_1 in Equation 1.26 and Equation 1.27 were changed to ensure the NO_x emissions sub-model accurately represents the experimental data. The value of ARC_1 was kept at 1.5 and the value of AERC_1 was changed. The values used for AERC_1 in the emission model are shown in Table 5.5.

Table 5.5: User defined values for AERC_1 for the NO_x emissions sub-model for engine tests using B2E9 fuel.

BMEP (MPa)	1500 rpm	2250 rpm	2500 rpm	2750 rpm	3000 rpm	3250 rpm
0.2	1.16667	1.0500	1.00000	1.04000	1.04000	1.01778
0.3	1.16667	1.0500	1.00000	1.04000	1.04000	1.01778
0.4	1.25000	1.0500	1.00000	1.04000	1.04000	1.01778
0.5	1.25000	1.0500	1.09666	1.04000	1.04000	1.01778
0.6	1.25000	1.1125	1.09666	1.10667	1.10667	1.13333

5.3 Results

In this section, the effects of changing different engine operating parameters on different engine responses were considered. These engine operating parameters include exhaust gas recirculation (EGR) percentage, main injection SOI (θ_{minj}), pilot injection SOI (θ_{pinj}) and pilot injection duration ($\Delta\theta_{pinj}$). Engine emissions were investigated over the WLTP drive cycle. Table 5.6 shows the engine emission results for the simulated and experimental DoE. Test 25 and test 26 could not be completed as the combination of the engine parameters prevented the engine from following the drive cycle accurately. Table 5.7 shows the p-values of each engine parameter that was varied in the RSM. The principal model analysis was based on the analysis of variance (ANOVA) which provided statistical information including the p-values of the different model terms. P-values of less than 0.02 are deemed as highly significant, which means that the probability of this phenomena is due to chance, is less than 2% [121, 122]. Engine parameters that have a significant effect on the engine emissions over the WLTP drive cycle will be discussed in detail. The use of graphs illustrating the main effect plots as well as the interaction plots between different engine parameters will also be illustrated. The higher the gradient of the line plots, the more significant effect the engine parameter has on the engine emissions response. Where possible, the simulated and experimental results are compared and discussed.

Table 5.6: The simulated and experimental values for the engine emissions for the RSM.

Run	Parameter settings				Simulated results		Experimental results				
	EGR (%)	θ_{minj} (CAD)	θ_{pinj} (CAD)	$\Delta\theta_{pinj}$ (%)	CO (g/km)	NO _x (g/km)	CO (g/km)	CO ₂ (g/km)	NO _x (g/km)	PN (#/km)	PM (g/km)
1	12.5	3	17	38	0.4380	1.6832	1.9453	138.7	1.9775	1.676E+14	0.0367
2	12.5	3	9	16	0.0371	2.5751	1.2426	170.3	1.3605	2.936E+14	0.0642
3	25.0	0	13	27	0.1267	1.8502	1.7885	178.9	1.0494	3.288E+14	0.0719
4	37.5	-3	9	16	0.0261	2.4727	2.8163	200.1	0.7504	6.243E+14	0.1366
5	25.0	0	13	27	0.1267	1.8502	2.0736	163.1	0.9113	4.492E+14	0.0983
6	12.5	3	9	38	0.3342	1.8922	3.1093	141.4	1.9169	3.800E+14	0.0831
7	12.5	-3	9	38	0.1267	1.8502	2.2036	161.2	1.3641	3.896E+14	0.0852
8	37.5	3	9	16	0.0067	1.5593	1.6643	169.3	1.0377	1.782E+14	0.0390
9	37.5	-3	17	16	0.0219	2.1379	2.2079	194.2	0.8464	3.594E+14	0.0786
10	12.5	-3	17	16	0.0216	2.5399	1.9418	199.8	1.0283	2.841E+14	0.0621
11	12.5	3	17	16	0.0351	2.5292	1.4127	188.6	1.6963	1.512E+14	0.0331
12	37.5	3	9	38	0.3452	1.4700	3.9093	162.8	1.7396	3.283E+14	0.0718
13	12.5	-3	17	38	0.3179	1.7874	2.0617	195.7	1.5207	1.357E+14	0.0297
14	37.5	3	17	38	0.3784	1.4534	2.6105	171.3	1.8798	8.892E+13	0.0195
15	37.5	3	17	16	0.0353	2.1905	1.5471	190.2	1.2556	1.198E+14	0.0262
16	12.5	-3	9	16	0.0259	2.8880	2.0409	214.4	1.0370	1.811E+14	0.0396
17	37.5	-3	9	38	0.2596	1.4921	2.1625	211.1	1.0166	1.768E+14	0.0387
18	25.0	0	13	27	0.1267	1.8502	1.9350	222.7	1.0658	1.250E+14	0.0273
19	25.0	0	13	27	0.1267	1.8502	2.0489	221.5	1.0458	1.119E+14	0.0245
20	37.5	-3	17	38	0.3285	1.3989	2.3646	205.7	1.1140	6.477E+13	0.0142
21	25.0	0	13	27	0.1267	1.8502	1.6210	212.3	1.2511	4.644E+13	0.0102
22	25.0	0	13	5	0.0042	2.2000	1.9477	208.2	0.9864	8.977E+13	0.0196
23	25.0	0	13	27	0.1267	1.8502	1.7582	201.8	1.2017	4.066E+13	0.0089
24	50.0	0	13	27	0.1289	1.6210	1.8820	198.9	1.0034	4.545E+13	0.0099
25	25.0	0	13	49	0.4429	1.6421	—	—	—	—	—
26	25.0	0	5	27	0.0825	2.0864	—	—	—	—	—
27	25.0	-6	13	27	0.0897	2.0868	2.2099	224.0	1.0375	5.844E+13	0.0128
28	25.0	0	21	27	0.1278	1.6998	1.7612	202.0	1.2637	3.515E+13	0.0077
29	25.0	6	13	27	0.1811	1.6374	1.5436	194.2	1.4842	2.351E+13	0.0051
30	0.0	0	13	27	0.1268	2.0220	1.6397	203.5	1.2513	3.799E+13	0.0083

Table 5.7: P-values for the engine response of the simulated and experimental RSM

	Simulated results		Experimental results			
	CO	NO _x	CO	CO ₂	NO _x	PN/PM
Model	< 0.02	< 0.02	< 0.02	0.224	< 0.02	< 0.02
Linear	< 0.02	< 0.02	< 0.02	< 0.02	< 0.02	0.08
EGR	0.63	< 0.02	< 0.02	0.37	< 0.02	0.20
$\theta_{min,j}$	< 0.02	< 0.02	0.23	< 0.02	< 0.02	0.59
$\theta_{pin,j}$	< 0.02	0.28	< 0.02	0.39	0.13	< 0.02
$\Delta\theta_{pin,j}$	< 0.02	< 0.02	< 0.02	0.07	< 0.02	0.83
Square	< 0.02	0.03	< 0.02	0.55	< 0.02	< 0.02
EGR \times EGR	0.86	0.86	0.65	0.71	0.64	0.47
$\theta_{min,j} \times \theta_{min,j}$	0.63	0.86	0.89	0.93	< 0.02	0.47
$\theta_{pin,j} \times \theta_{pin,j}$	0.22	0.77	0.25	0.33	0.43	0.50
$\Delta\theta_{pin,j} \times \Delta\theta_{pin,j}$	< 0.02	< 0.02	< 0.02	0.24	< 0.02	< 0.02
2-Way Interaction	< 0.02	0.12	< 0.02	0.64	0.26	< 0.02
EGR \times $\theta_{min,j}$	0.10	0.44	0.62	0.97	0.21	0.68
EGR \times $\theta_{pin,j}$	0.21	0.17	0.59	0.74	0.37	0.40
EGR \times $\Delta\theta_{pin,j}$	0.31	0.23	0.12	0.10	0.65	0.17
$\theta_{min,j} \times \theta_{pin,j}$	0.65	0.06	0.20	0.58	1.00	0.07
$\theta_{min,j} \times \Delta\theta_{pin,j}$	< 0.02	0.08	< 0.02	0.35	< 0.02	0.08
$\theta_{pin,j} \times \Delta\theta_{pin,j}$	< 0.02	0.78	< 0.02	0.95	0.62	< 0.02
Lack-of-Fit	—	—	0.16	0.75	0.82	0.25

5.3.1 CO emissions

The quadratic model developed for the experimental and simulated CO emissions as fitted based on the RSM design corresponds to:

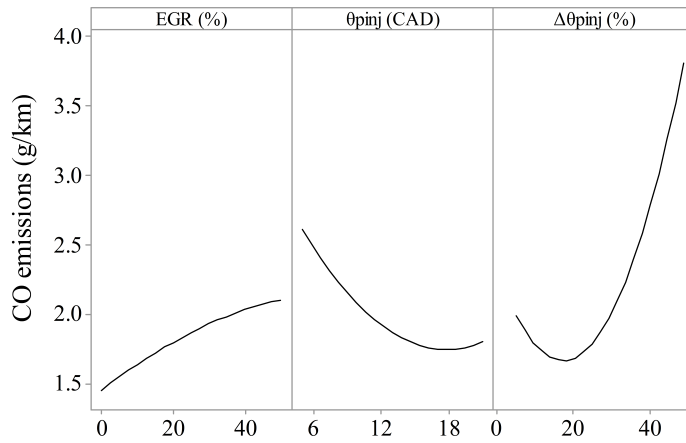
$$\begin{aligned} Z_{CO_{exp}} = & 2.01 - 0.0088 \times EGR - 0.035 \times \theta_{pinj} \\ & - 0.0307 \times \Delta\theta_{pinj} + 0.002126 \times \Delta\theta_{pinj} \times \Delta\theta_{pinj} \\ & + 0.00801 \times \theta_{minj} \times \Delta\theta_{pinj} - 0.00489 \times \theta_{pinj} \times \Delta\theta_{pinj} \end{aligned} \quad (5.17)$$

and

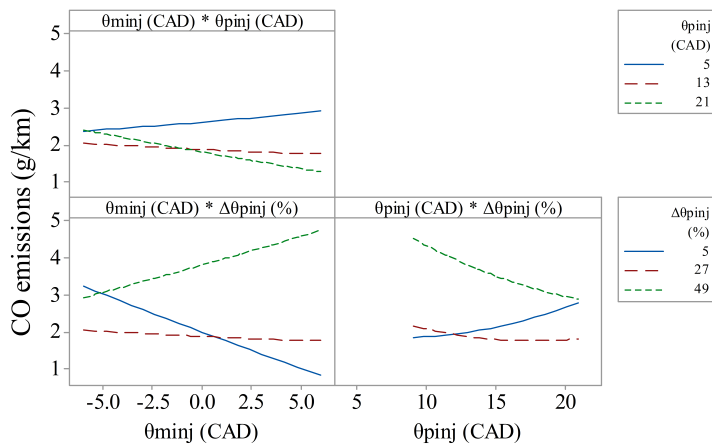
$$\begin{aligned} Z_{CO_{sim}} = & 0.156 + 0.0002 \times \theta_{minj} - 0.0221 \times \theta_{pinj} \\ & - 0.00806 \times \Delta\theta_{pinj} + 0.000206 \times \Delta\theta_{pinj} \times \Delta\theta_{pinj} \\ & + 0.000804 \times \theta_{minj} \times \Delta\theta_{pinj} + 0.000576 \times \theta_{pinj} \times \Delta\theta_{pinj} \end{aligned} \quad (5.18)$$

$Z_{CO_{exp}}$ and $Z_{CO_{sim}}$ are the experimental and simulated CO emissions in the exhaust gas of the engine in grams per kilometer. High values of R^2 (91.31%) and adjusted R^2 (80.24%) for Equation 5.17 and 97.46% and 94.92% for Equation 5.18 indicate a high correlation between the simulated and experimental CO emissions and the RSM predicted values of the CO emissions. Figure 5.10 and Figure 5.11 visually show the main effects and interaction effects of the engine parameters on the engine CO emissions for the experimental emissions and simulated emissions, respectively.

For the experimental CO emissions the linear terms EGR , θ_{pinj} and $\Delta\theta_{pinj}$, the quadratic term for $\Delta\theta_{pinj}$ and the two-way interaction effects between θ_{minj} and $\Delta\theta_{pinj}$ and θ_{pinj} and $\Delta\theta_{pinj}$ are deemed significant with $p < 0.02$. For the simulated CO emissions the linear terms θ_{minj} , θ_{pinj} and $\Delta\theta_{pinj}$, the quadratic term for $\Delta\theta_{pinj}$ and the two-way interaction effects between θ_{minj} and $\Delta\theta_{pinj}$ and θ_{pinj} and $\Delta\theta_{pinj}$ are deemed significant. The increase in EGR percentage from zero to a maximum of 50% has a negative effect on the formation of CO emissions, as seen in Figure 5.10a. When comparing the results between the experimental and simulated CO emissions (Table 5.6), it is evident that the simulated CO emissions are under predicted compared to the experimental CO emissions. This can be as a result of WAVE simulating complete combustion as well as the additional oxygen content in the ethanol and biodiesel. The additional oxygen in the fuel also lessens the effect of EGR on CO emissions formation when compared to CO emissions for engines using conventional petroleum diesel. The difference in values between the simulated and the experimental CO emissions can be attributed to the emissions model used by WAVE which under predicts emissions at lower loads (section 3.2.3.2). The majority of the WLTP drive cycle operates at lower engine loads (Figure 1.4).

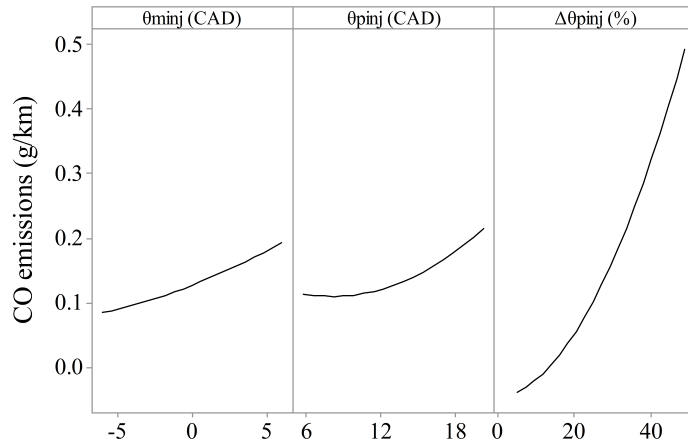


(a) Main effects plot for experimental engine CO emissions.

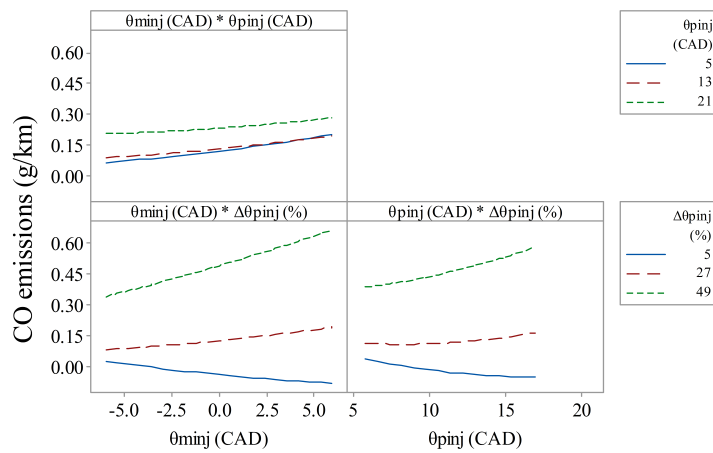


(b) Interaction effects plot for the experimental engine CO emissions.

Figure 5.10: Response plots for the experimental CO emissions when engine operating conditions are varied.



(a) Main effects plot for simulated engine CO emissions.



(b) Interaction effects plot for simulated engine CO emissions.

Figure 5.11: Response plots for simulated CO emissions when engine operating conditions are varied.

Figure 5.10a also shows that CO emissions decrease by increasing the dwell time of the pilot injection fuel (increasing the gap between the SOI of the pilot injection and the main injection SOI). By offsetting the pilot injection SOI by approximately 18 CAD a maximum reduction of CO emissions can be achieved. Beatrice *et al.* [100] similarly reports that by increasing the difference between the pilot injection SOI and main injection SOI from 7 CAD to 10 CAD when running the engine at 1500 rpm and 2 BMEP load, the CO emissions reduced from 800 ppm to 600 ppm. The increased dwell time promotes the stratification of the fuel in the cylinder and as the cylinder piston reaches top dead centre (TDC) it creates an almost homogeneous environment, which enables the increased oxygenation of CO gasses. Figure 5.12 shows a time series plot for CO emissions of test 8 and test 15, which have different pilot injection offsets (θ_{pinj}) with the WLTP drive cycle shown in dashed lines. The

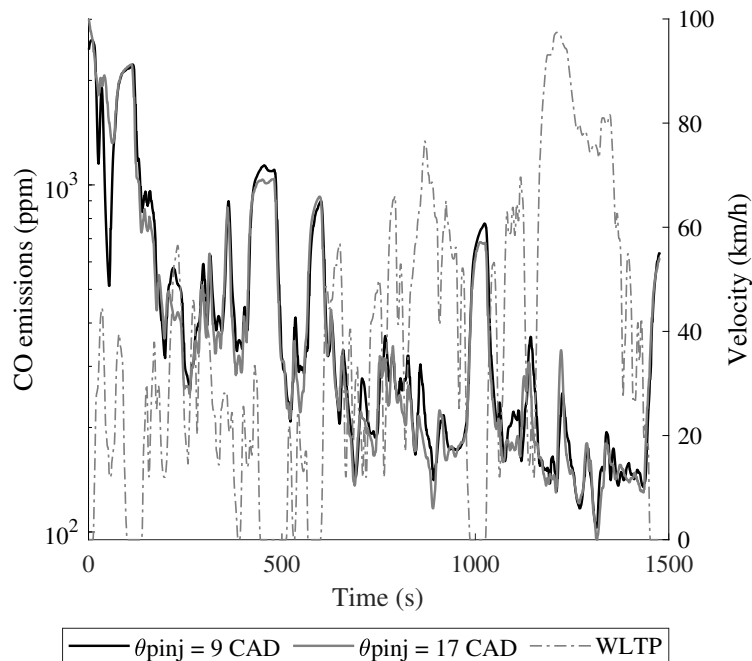


Figure 5.12: CO emissions comparison with θ_{pinj} at 9 CAD and 17 CAD (test 8 & 15).

differences in CO emissions between the two tests considered in Figure 5.12 are minor except at idling scenarios in the WLTP. CO emissions are at its highest during idling, as the fuel and air does not mix properly to ensure improved combustion. By increasing the offset of the pilot injection SOI compared to the main injection SOI, fuel has more time to mix with the air and improve overall combustion. This can be seen in Figure 5.12 where CO emissions are reduced during idling (0 km/h) for a pilot injection offset of $\theta_{pinj} = 17$ CAD.

The percentage fuel delivered through the pilot injection also significantly influences the formation of CO emissions. Engine CO emissions can be kept to a

minimum if approximately 20% of the total fuel is delivered through the pilot injection. The increase in fuel delivered through the pilot injection, increases the amount of fuel available to mix with the intake air, before combustion occurs and thus increases the fraction of fuel burned in the premixed combustion phase. Figure 5.10a also shows that by increasing the amount of fuel delivered by the pilot injection past 20%, increases the CO emissions generated by the engine. Carlucci *et al.* [56] reported a similar phenomena where a certain percentage of the fuel delivered through the pilot injection, promoted the homogeneity of the air fuel mixture prior to combustion. For small percentages of fuel delivered through the pilot injection, the mixture is too lean for autoignition to occur even with the increased pressure and temperature produced by the compression stroke of the engine. When the percentage of fuel increases past a certain point, autoignition of the fuel injected through the pilot injection can occur and this reduces the ignition delay of the main injection, due to increased temperatures and pressures. The reduced ignition delay causes the majority of the fuel delivered through the main injection to burn in the diffusion combustion phase which increases the formation of CO emissions [48]. If more than 40% of the fuel is delivered through the pilot injection, it can also start influencing the performance of the engine with an increase in incomplete combustion which also results in an increase of CO emissions.

The interaction effects between θ_{minj} and $\Delta\theta_{pinj}$ and θ_{pinj} and $\Delta\theta_{pinj}$ are shown in Figure 5.10b. The interaction effects between θ_{minj} and $\Delta\theta_{pinj}$ for the experimental CO emissions show that for a $\Delta\theta_{pinj}$ of 27%, there is minor changes when changing the main injection SOI. When $\Delta\theta_{pinj}$ is 5%, experimental CO emissions decrease when the main injection SOI is advanced. As the majority of the fuel is delivered through the main injection, by advancing the SOI of the main injection results in improved combustion as the combustion temperature is increased. When 49% of the fuel is delivered through the pilot injection, CO emissions increases when the main injection SOI is advanced. As mentioned earlier, autoignition of the fuel delivered through the pilot injection can occur when higher percentages of the total fuel is delivered through the pilot injection. When advancing the main injection SOI, the ignition delay of the fuel delivered through the main injection is decreased and the majority of the fuel is burned in the diffusion combustion phase. When the main injection is retarded, the ignition delay of the main injection is increased and more fuel is burned in the premixed combustion stage, thus decreasing CO emissions. This is also true for the simulated CO emissions.

The interaction effects between θ_{pinj} and $\Delta\theta_{pinj}$ for the experimental CO emissions show that for percentages of fuel 27% and higher, by increasing the dwell time of the pilot injection, CO emissions are decreased. 49% fuel delivered through

the pilot injection has an overall higher CO emissions result as a bigger portion of the fuel cannot mix sufficiently with the air before combustion starts, compared to when only 27% of the fuel is introduced through the pilot injection. As shown in Figure 5.10b for small percentages of fuel injected through the pilot injection, CO emissions increase when the dwell time of the pilot injection increases. As 9% of the fuel is ethanol, the high latent heat of evaporation can cool the combustion chamber down with a longer pilot injection dwell time. A cooler combustion chamber can increase the ignition delay as well as hinder complete combustion, which has a negative effect on CO emissions.

The interaction effects between θ_{pinj} and $\Delta\theta_{pinj}$ for the simulated CO emissions show that by increasing pilot injection dwell time as well as increasing the percentage of fuel delivered through the pilot injection, increases the CO emissions. This is contradicting the experimental CO emissions results. When looking at the combustion equations, the premixed burn fraction calculated with Equation 5.16 is decreased with the increase of pilot injection dwell time and percentage of fuel delivered through the pilot injection. As a result the combustion model is simulated an increased diffusion combustion event, which results in CO emissions increasing. The line graph showing CO emissions when 5% of fuel is delivered through the pilot injection goes negative for high pilot injection dwell times. This is a result of the validation points not including such a small percentage of fuel delivered through the pilot injection (Table 5.6). It is evident that the combustion model has a high residual for $\Delta\theta_{pinj} = 0.05$.

5.3.2 CO₂ emissions

The quadratic model developed for the simulated CO₂ emissions as fitted based on the RSM design corresponds to:

$$Z_{CO_2} = 131.6 - 3.70 \times \theta_{minj} \quad (5.19)$$

Z_{CO_2} is the CO₂ emissions in the exhaust gas of the engine in grams per kilometer. A value of R^2 (62.28%) and adjusted R^2 (21.66%) for Equation 5.19 indicate a poor correlation between the simulated and experimental CO₂ emissions and the RSM predicted values of the CO₂ emissions. The adjusted R^2 is low as it shows that the majority of the tests conducted for CO₂ emissions does not improve the model more than would be expected by chance. By using the power and sample size calculations, it shows that in order to detect a relationship between changing the engine parameters and CO₂ emissions generation and providing a reasonably precise

estimate, the amount of tests needed to be conducted have to a minimum of 91 tests [114]. The tests required is not economical and time efficient for this research and because the other models all exhibit high values of R^2 and adjusted R^2 and $p < 0.02$, the CO₂ emissions model will not be improved. As such CO₂ emissions will also not be considered at the optimistaion stage of this study.

5.3.3 NO_x emissions

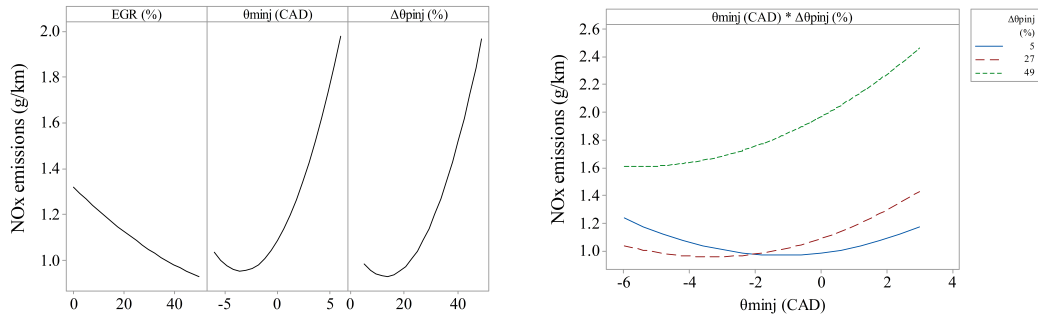
The quadratic model developed for the experimental and simulated NO_x emissions as fitted based on the RSM design corresponds to:

$$\begin{aligned} Z_{\text{NO}_x_{\text{exp}}} = & 1.614 - 0.0152 \times EGR - 0.0088 \times \theta_{\text{minj}} \\ & - 0.0227 \times \Delta\theta_{\text{pinj}} + 0.001162 \times \theta_{\text{minj}} \times \theta_{\text{minj}} \\ & + 0.000801 \times \Delta\theta_{\text{pinj}} \times \Delta\theta_{\text{pinj}} \\ & + 0.002311 \times \theta_{\text{minj}} \times \Delta\theta_{\text{pinj}} \end{aligned} \quad (5.20)$$

and

$$\begin{aligned} Z_{\text{NO}_x_{\text{sim}}} = & 4.475 - 0.0365 \times EGR - 0.1543 \times \theta_{\text{minj}} \\ & - 0.1019 \times \Delta\theta_{\text{pinj}} + 0.001162 \times \Delta\theta_{\text{pinj}} \times \Delta\theta_{\text{pinj}} \end{aligned} \quad (5.21)$$

$Z_{\text{NO}_x_{\text{exp}}}$ and $Z_{\text{NO}_x_{\text{sim}}}$ are the experimental and simulated NO_x emissions in the exhaust gas of the engine in grams per kilometer. High values of R^2 (95.80%) and adjusted R^2 (90.46%) respectively for Equation 5.20 and 92.35% and 84.71% respectively for Equation 5.21 indicate a high correlation between the simulated and experimental NO_x emissions and the RSM predicted values of the NO_x emissions. Figure 5.13 and Figure 5.14 visually show the main effects and interaction effects of the four engine parameters on the engine NO_x emissions for the experimental emissions and simulated emissions, respectively. For the experimental NO_x emissions the linear terms EGR , θ_{minj} and $\Delta\theta_{\text{pinj}}$, the quadratic terms for θ_{minj} and $\Delta\theta_{\text{pinj}}$ and the two-way interaction effects between θ_{minj} and $\Delta\theta_{\text{pinj}}$ are deemed significant with $p < 0.02$. For the simulated NO_x emissions the linear terms EGR , θ_{minj} and $\Delta\theta_{\text{pinj}}$ and the quadratic term for $\Delta\theta_{\text{pinj}}$ are deemed significant. The two-way interaction effects between θ_{minj} and $\Delta\theta_{\text{pinj}}$ for the simulated NO_x emissions are nearing significance with $p = 0.08$. Overall, the simulated NO_x emissions are calculated higher than the experimental NO_x emissions. With good agreement between simulated and experimental NO_x emissions for steady-state engine operation points, the model becomes less accurate when a transient drive cycle is investigated. The emissions of both the simulated and experimental NO_x emissions were plotted in Figure 5.15. Figure 5.15 shows that the simulated NO_x emissions and the experimental NO_x



(a) Main effects plot for the experimental engine NO_x emissions. (b) Interaction effects plot for the experimental engine NO_x emissions.

Figure 5.13: Response plots for experimental NO_x emissions when engine operating conditions are varied.

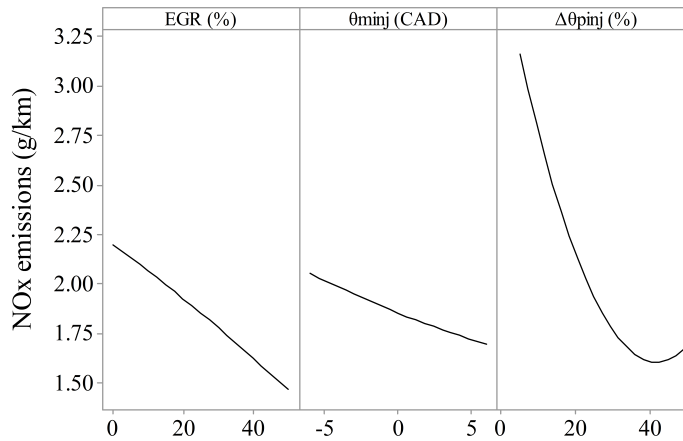


Figure 5.14: Response plots for simulated NO_x emissions when engine operating conditions are varied.

emissions agree for the first 500 seconds of the drive cycle. From there the simulated emissions are under-predicted compared to the experimental emissions. The NOVA gas analyser used for the experimental tests has a T₉₀ of 8 seconds which can cause smoothing of the recorded data which can result in the omission of certain transient behaviour of the NO_x emissions. Smoothing of the data can cause an overall higher measurement of the emissions. Also, the use of the user-defined value $AERC_1$ alone is not sufficient for the accurate calculation of NO_x emissions when a transient study is conducted. The model can be improved by adding additional parameters that take engine load into consideration which will increase the accuracy at higher engine loads in a transient study.

When considering the effects of the changing engine parameters under investiga-

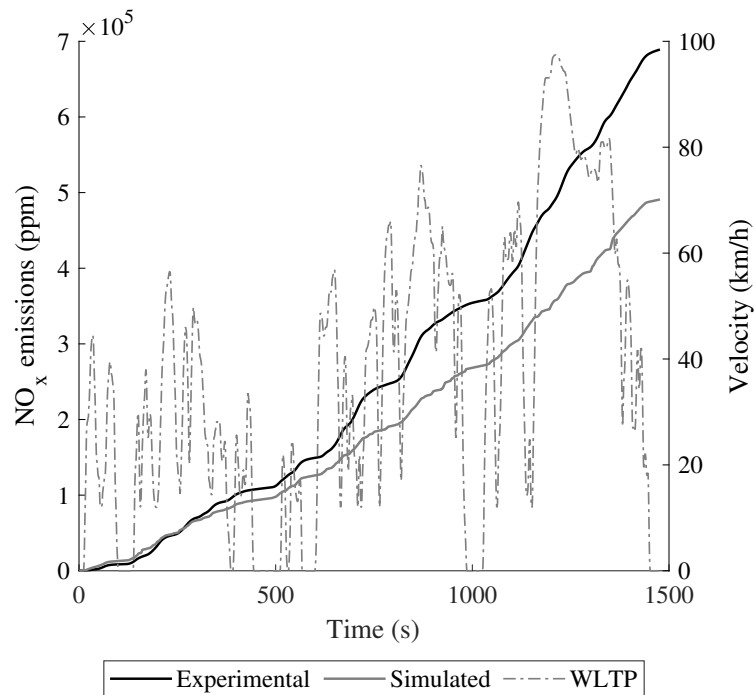


Figure 5.15: Comparison between experimental NO_x emissions and simulated NO_x emissions for run 1.

tion, both the simulated and experimental NO_x emissions show a reduction in NO_x emissions with an increase in EGR percentage. Figure 5.16 shows a time series plot for NO_x emissions of test 2 and test 8, which have different EGR percentages with the WLTP drive cycle shown in dashed lines. Throughout the drive cycle, the NO_x emissions generated by the test with an EGR of 37.5% is lower than the test with an EGR of 12.5%. The difference is more pronounced at lower drive cycle speeds. The effect of EGR percentage on NO_x emissions are also deemed significant by the statistical model which is in line with the majority of research discussed in previous chapters.

The change in main injection SOI results in different outcomes for the simulated and experimental NO_x emissions. The experimental NO_x emissions exhibit an increase when the SOI is advanced and a minimum when retarding the main injection SOI map by approximately 3 CADs. The simulated NO_x emissions decrease when advancing the SOI, but the decrease is not as pronounced. Bohl *et al.* [141] investigated the effect of the main injection SOI on NO_x emissions when using HVO fuel and concluded that the advanced injection causes the peak pressure to be closer to TDC and therefore cylinder temperature is increased. The different behaviour of the simulated NO_x emissions when the main injection SOI is varied, is caused by the combustion calculation of the premixed burn fraction for WAVE's combustion model (Equation 5.16). When all the parameters of the equation are kept constant and

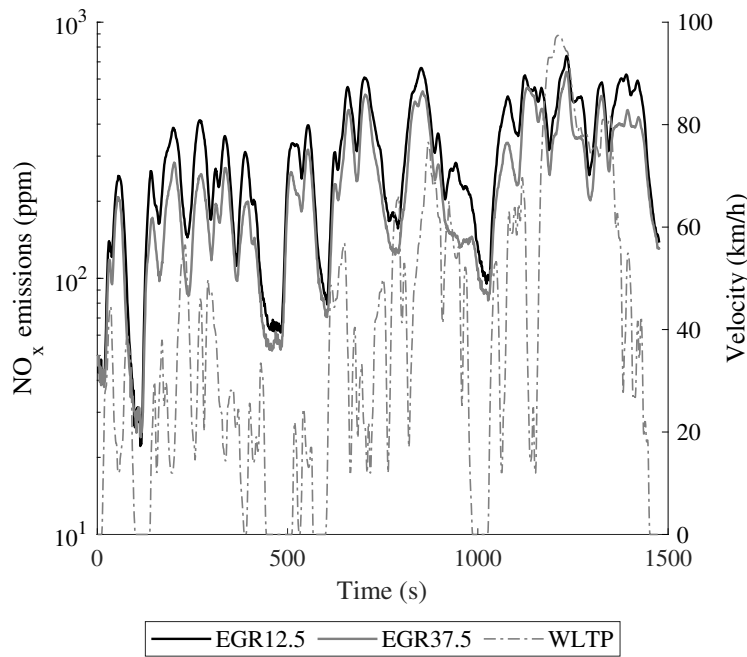


Figure 5.16: NO_x emissions comparison with EGR at 12.5% and 37.5% (test 2 & 8).

only the main injection SOI is varied, the premixed fuel fraction burned decreases when the main injection SOI is advanced. The decrease in premixed combustion, decreases the temperature of the combustion event and as such the NO_x emissions will also decrease. Equation 5.16 has a similar effect on the NO_x emissions when only considering pilot injection duration. If all the parameters of Equation 5.16 are kept constant and the pilot injection duration is varied, the premixed burn fraction decreases. Even though the equation was created by fitting it to experimental data and the regression equation has a good agreement with the experimental data, the results of the transient study shows that Equation 5.16 needs additional validation points to increase its accuracy for the use in drive cycle simulation.

For the experimental results, the increase in pilot injection duration increases the NO_x emissions. As more fuel is introduced through the pilot injection, a bigger proportion of the total fuel will burn in the premixed combustion event, thus increasing the combustion temperature as well as the NO_x emissions.

The interaction effects between θ_{minj} and $\Delta\theta_{pinj}$ can be seen in Figure 5.13b. For the experimental NO_x emissions, by advancing the main injection by approximately 5 CADs and delivering approximately 50% of the fuel through the pilot injection, results in the maximum amount of NO_x emissions generated. This is caused by the increase in fuel that can mix with the air before combustion occurs and with the advancement of the main injection, start of combustion occurs close to TDC, which results in higher combustion temperatures. With a decrease in the percentage of fuel

delivered through the pilot injection, the NO_x emissions are reduced and the effect of changing the main injection SOI on NO_x emissions is not as pronounced.

5.3.4 PN/PM emissions

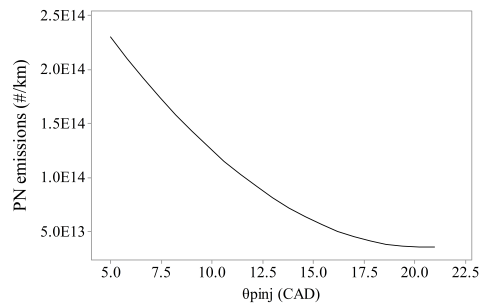
PN emissions and PM emissions are discussed jointly, as the voltage trap signal of the Pegasor M-sensor are converted by separate coefficients for PN and PM emissions (Equation 2.2 and 2.3). The quadratic models developed for the PN emissions and PM emissions as fitted based on the RSM design correspond to:

$$\begin{aligned} Z_{PN} = & 811133287725601 \\ & - 7633497409759 \times \theta_{pinj} \\ & + 1207509358289 \times \Delta\theta_{pinj} \times \Delta\theta_{pinj} \\ & - 1214678643048 \times \Delta\theta_{pinj} \times \theta_{pinj} \end{aligned} \quad (5.22)$$

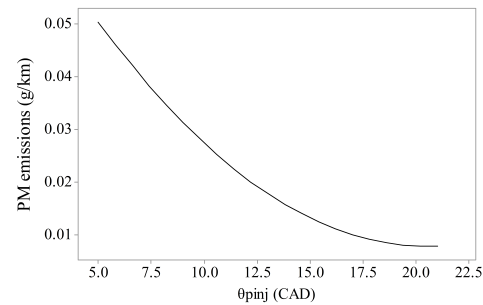
and

$$\begin{aligned} Z_{PM} = & 0.1775 - 0.00167 \times \theta_{pinj} \\ & + 0.000264 \times \Delta\theta_{pinj} \times \Delta\theta_{pinj} \\ & - 0.000264 \times \Delta\theta_{pinj} \times \theta_{pinj} \end{aligned} \quad (5.23)$$

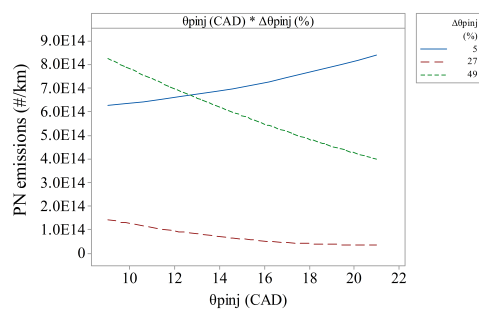
Z_{PN} and Z_{PM} are the PN emissions and PM emissions in the exhaust gas of the engine in number per kilometer and grams per kilometer. High values of R^2 (89.79%) and adjusted R^2 (73.91%) for Equation 5.22 and Equation 5.23 respectively indicate a high correlation between the experimental PN emissions and PM emissions and the RSM predicted values of the PN emissions and PM emissions. For the PN emissions and PM emissions the linear term θ_{pinj} , the quadratic terms for $\Delta\theta_{pinj}$ and the two-way interaction effects between θ_{pinj} and $\Delta\theta_{pinj}$ are deemed significant with $p < 0.02$. Figure 5.17a and Figure 5.17b show that by increasing the dwell time of the pilot injection, PN emissions and PM emissions decrease. By increasing the dwell time from 5 CADs to approximately 18 CADs, PN emissions and PM emissions can be reduced by 80%. This is due to the fact that with an increased dwell time, the fuel and air mixture have longer time to mix together thoroughly. A more homogeneous mixture is formed prior to combustion, leading to a higher in-cylinder pressure and combustion temperature which promote the particle oxidation process. The interaction effects shown in Figure 5.17c and Figure 5.17d also show that with a high pilot injection dwell time and injecting 49% of the fuel through the pilot injection can decrease the PN emissions and PM emissions significantly. Lower percentages ($< 27\%$) result in only a limited amount of the fuel being mixed with the air and thus a bigger fraction of the fuel burns in the diffusion combustion phase.



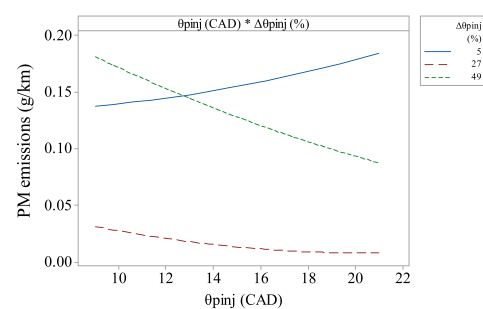
(a) Main effects plot for engine PN emissions.



(b) Main effects plot for engine PM emissions.



(c) Interaction effects plot for engine PN emissions.



(d) Interaction effects plot for engine PM emissions.

Figure 5.17: Main and Interaction plots for PM/PN emissions when engine operating conditions are varied.

Smaller percentages of fuel injected through the pilot injection can ignite during the compression stage and decrease the ignition delay of the main injection. A shorter ignition delay for the main injection results in an increase of fuel burnt in the diffusion combustion phase which increases PN/PM emissions. Figure 5.17 shows that with an increase in pilot injection dwell time with a small percentage of fuel injected through the pilot injection can cause a further increase in PN/PM emissions.

5.3.5 Optimising engine parameters

As there is more than one engine emission response to be optimised, it is necessary to set requirements for each response, that the optimisation tool will optimise towards. The desirability approach was used to minimise all engine out emissions (as discussed in Section 4.3.5). Figure 5.18 shows the desirability plot when minimising all engine emissions. An overall desirability of 89% was achieved by having a maximum EGR percentage of 45%, retarding the main injection SOI map by 2 CADs, setting the offset of the pilot injection to the main injection to 21 CADs and injecting 24% of

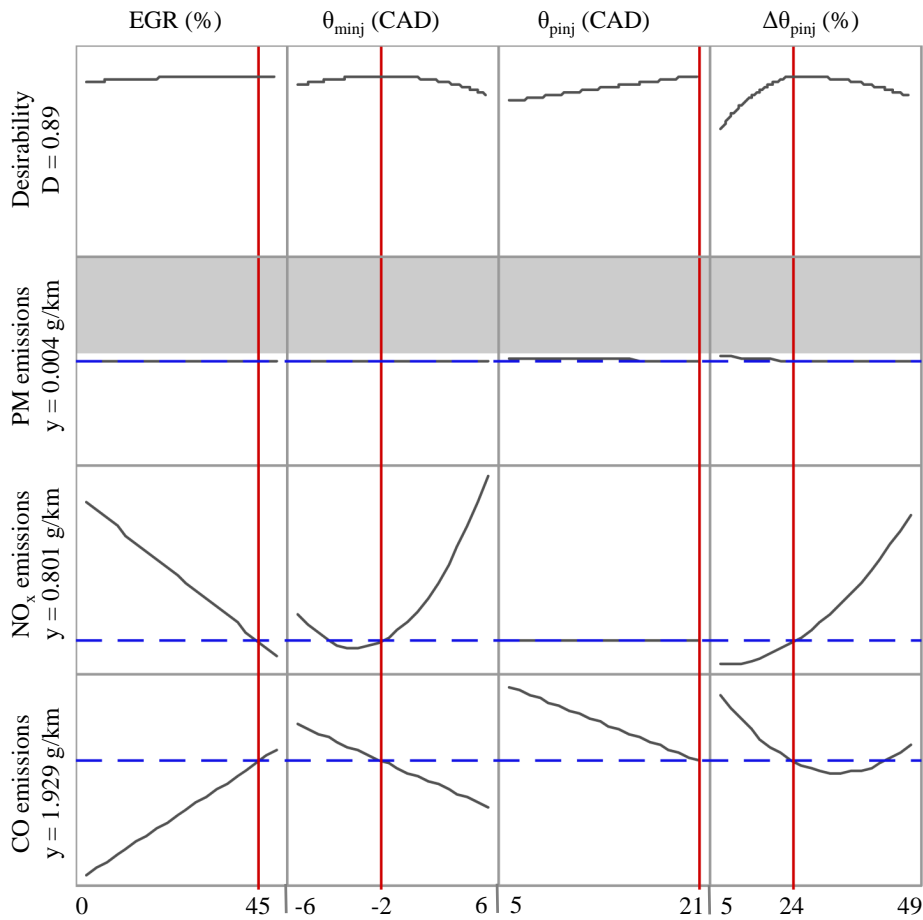


Figure 5.18: Optimisation plot for the engine emissions RSM.

the total fuel through the pilot injection event. This will result in CO emissions of 1.92 g/km, NO_x emissions of 0.80 g/km and PM emissions of 0.004 g/km. NO_x emissions are reduced by 29% and CO emissions increased by 47% compared to pump diesel available at all major pumping stations [41]. The increase of EGR percentage, reduces the NO_x emissions and reduces the combustion temperature. By increasing the dwell time of the pilot injection and injecting approximately 20% of the total fuel with the pilot injection event decreases CO emissions as a result of an increase in the homogeneity of the air fuel mixture and combustion. PM emissions are also below the legislated limit of 0.025 g/km. Table 5.8 shows a summary of the results and the percentage change compared to pump diesel as well as the results obtained in Chapter 4. NO_x emissions are further reduced using LTC techniques with a total reduction of 29% compared to pump diesel. CO emissions increase by 47% compared to pump diesel when LTC techniques are used. The trade-off between NO_x emissions and CO emissions are evident and also seen in other published work where the decrease in NO_x emissions result in an increase in CO emissions [60].

Table 5.8: Summary of results showing the change in emissions compared to pump diesel

	Pump diesel	B2E9	B2E9_LTC
CO emissions (g/km)	1.309	0.796	1.929
NO _x emissions (g/km)	1.136	1.003	0.801
CO emissions	—	-34%	47%
NO _x emissions	—	-10%	-29%

5.4 Closing remarks

This study investigated the effects of engine operating parameters on the emission characteristics of a compression ignition engine fuel with a ternary blend, B2E9. The engine was tested over the World Harmonised Light vehicle Test Procedure (WLTP). Based on a RSM DoE, 30 runs were formulated which included 6 replicates of the center point to evaluate the reproducibility and the lack-of-fit of the derived models. It was shown that:

1. NO_x emissions can be reduced by approximately 29% by using a maximum of 45% EGR, retarding the main injection SOI by 2 CADs, setting the dwell time of the pilot injection to 21 CADs and injecting 24% of the total fuel through the pilot injection.
2. Even though the fuel delivery was optimised to minimise CO emissions, there was still an increase of approximately 47% compared to a vehicle running on pump diesel. This is due to the trade-off between NO_x emissions and CO emissions.
3. EGR can be used to reduce NO_x emissions by approximately 34% when the EGR percentage is increased from 0% to 50%. The opposite occurs for CO emissions, which increases by approximately 32% when EGR is increased to a maximum of 50%.
4. By advancing the main injection SOI, NO_x emissions increase and CO emissions decrease as a result of the start of combustion occurring closer to TDC, thus increasing the combustion temperature and combustion pressure.
5. An increase of the dwell time of the pilot injection to approximately 21 CADs can decrease CO emissions by approximately 17%, as the increased dwell time promotes the mixing of the fuel and air which causes an increase in the premixed combustion phase. A more homogeneous mixture also promotes the particle oxidation process which reduces the total PM/PN emissions.

6. By injecting more fuel through the pilot injection a higher percentage of the fuel mixes with the air before combustion commences. This increases the portion of fuel being burned in the premixed combustion phase and increases combustion temperatures. As a result NO_x emissions increase and CO emissions decrease.
7. This work demonstrated that the RSM DoE is a useful tool to quantify the effect of different engine operating parameters on the engine's emissions response. It is also useful to determine the optimum operating configuration that will meet the researcher's criteria.
8. Ricardo WAVE and Ricardo IGNITE are useful tools to investigate emissions reduction techniques. The simulation can accurately represent steady-state scenarios, but is lacking when transient cycles are considered. It is necessary to improve the combustion model to improve its capabilities for transient studies. The limitation of only two inputs (premixed burn fraction and SOC) causes unrealistic results for certain transient scenarios and ultimately influence the emission model calculations.

Chapter 6

Conclusion and future work

6.1 Conclusions

The following sections discuss how the thesis successfully studied the application of renewable fuels to meet future automotive legislations. The research objectives:

1. Simulate the test engine on a commercially available simulation tool to aid in predicting vehicle emissions of CO and NO_x.
2. Validate the simulation tool using data obtained from the engine test cell.
3. Construct a mixture design of experiment (DoE) to characterise the influence of fuel blends of petroleum diesel, biodiesel and ethanol on the engine emissions of CO, CO₂ and NO_x.
4. Use the results from the mixture DoE to determine an optimum fuel blend that complies with the renewable energy directive (RED) of the UK as well as minimise harmful emissions.
5. Construct a design of experiment (DoE) to characterise the influence of fuel injection timing, fuel injection amount and exhaust gas recirculation percentage on the engine emissions of CO, CO₂, PM/PN and NO_x.
6. Optimise the engine operating parameters which include fuel injection timing, fuel injection amount and exhaust gas recirculation percentage to minimise harmful emissions of CO, CO₂, PM/PN and NO_x.

that were originally presented in Chapter 1 were addressed by the research documented in Chapters 3, 4 and 5.

1. *Simulate the test engine on a commercially available simulation tool to aid in predicting vehicle emissions of CO and NO_x*

- The test engine was successfully simulated using Ricardo WAVE.
- The engine simulation's fidelity was increased by adding measured engine data to the simulation which include valve lift profiles and after market ECU map data.
- Ricardo IGNITE was used to simulate the characteristics of the vehicle that is fitted with the test engine under consideration.
- A co-simulation was set-up between Ricardo WAVE and Ricardo IGNITE to enable the investigation of engine emissions calculated by Ricardo WAVE when the vehicle is tested over a drive cycle in Ricardo IGNITE.

2. *Validate the simulation tool using data obtained from the engine test cell.*

- The engine simulation was validated using experimental steady-state data which included in-cylinder pressure data and engine emissions data when running on petroleum diesel as well as biofuel.
- The vehicle load requirements calculated in Ricardo IGNITE when driving the NEDC drive cycle were validated using a separate mathematical model. The validated model was also successfully used for the simulation of the WLTP.
- The emissions model used to simulate CO emissions is accurate for high load scenarios, but under predicts CO emissions for low engine loads. For transient simulations, the emissions model under predicts the CO emissions. Improvement of the existing model is needed to increase the accuracy of the simulated results during transient tests.
- The emissions model used to simulate NO_x emissions follows the same trend as the experimental data, but under predicts the majority of the emissions generated. Spikes of high emissions are also frequently observed in the simulated emissions which influence the overall results. The use of constant values ($AERC_1$) to calibrate the NO_x emissions model are not sufficient for transient emissions simulation. An improved model that takes engine load into consideration is needed to increase the accuracy of the NO_x emissions model.

3. *Construct a mixture design of experiment (DoE) to characterise the influence of fuel blends of petroleum diesel, biodiesel and ethanol on the engine emissions of CO, CO₂ and NO_x.*

- A mixture design of experiment was successfully constructed to determine an optimum ternary blend that reduces CO emissions, CO₂ emissions and NO_x emissions as well as increase the renewable content of the fuel.
- A flushing procedure was created to ensure that the fuel blend from the previous test does not influence the results generated for the fuel blend of the next test.

4. *Use the results from the mixture DoE to determine an optimum fuel blend that complies with the renewable energy directive (RED) of the UK as well as minimise harmful emissions.*

- An optimum blend of B2E9 was calculated that reduces CO emissions by 34%, NO_x emissions by 9.7% and CO₂ emissions by 21% when compared to pump diesel.
- From a carbon dioxide reduction viewpoint a binary mixture of B10 would be best, due to the low well-to-tank emissions of biodiesel. However, by increasing the biofuel content in the range B5 to B15 maximises the harmful exhaust emissions. From a harmful emissions reduction viewpoint a binary mixture of E10 would be best, due to the minimisation of carbon monoxide and nitrogen oxides in the range of E5 to E15. However, ethanol is immiscible in diesel and for practical reasons biodiesel needs to be added as an emulsifier.
- To achieve the optimum mixture, investment into second and third generation ethanol is required.

5. *Construct a design of experiment (DoE) to characterise the influence of fuel injection timing, fuel injection amount and exhaust gas recirculation percentage on the engine emissions of CO, CO₂, PM, PN and NO_x.*

- A 2⁴ Central Composite Design of Experiment was successfully constructed to characterise the influence of fuel injection timing, fuel injection amount and exhaust gas recirculation percentage on the engine emissions.

6. *Optimise the engine operating parameters which include fuel injection timing, fuel injection amount and exhaust gas recirculation percentage to minimise harmful emissions of CO, CO₂, PM/PN and NO_x.*

- NO_x emissions can be reduced by approximately 29% by using a maximum of 45% EGR, retarding the main injection SOI by 2 CADs, setting the dwell time of the pilot injection to 21 CADs and injecting 24% of the total fuel through the pilot injection.

- Even though the fuel delivery was optimised to minimise CO emissions, there was still an increase of approximately 47% compared to the baseline model vehicle running on pump diesel. This is due to the trade-off that exists between NO_x emissions and CO emissions.
- EGR can be used to reduce NO_x emissions by approximately 34% when the EGR percentage is increased from 0% to 50%. The opposite occurs for CO emissions, which increases by approximately 32% when EGR is increased to a maximum of 50%.
- By advancing the main injection SOI, NO_x emissions increase and CO emissions decrease as a result of the start of combustion occurring closer to TDC, thus increasing the combustion temperature and combustion pressure.
- An increase of the dwell time of the pilot injection to approximately 21 CADs can decrease CO emissions by approximately 17%, as the increased dwell time promotes the mixing of the fuel and air which causes an increase in the premixed combustion phase. A more homogeneous mixture also promotes the particle oxidation process which reduces the total PM/PN emissions.
- By injecting more fuel through the pilot injection a higher percentage of the fuel mixes with the air before combustion commences. This increases the portion of fuel being burned in the premixed combustion phase and increases combustion temperatures. As a result NO_x emissions increase and CO emissions decrease.

6.2 Recommendations for future work

The following recommendations are proposed for future work that can build on the results obtained in this research:

1. **Engine simulation:** The generated experimental data for the mixture DoE as well as the CCD DoE can be used to construct an improved CO emissions model and NO_x emissions model for Ricardo WAVE. Parameters calculated by Ricardo WAVE can be fed into the emission models, increasing the input parameters received, compared to the current built-in models. The models developed in Ricardo WAVE and Ricardo IGNITE can also be modified to be used for hardware in the loop (HiL) applications. The vehicle systems model in Ricardo IGNITE can be used to drive an engine in a test cell over different drive cycles to investigate engine emissions. The engine model in Ricardo WAVE can be coupled with a simulator where a driver drives a route and the engine model calculates all corresponding engine characteristics from torque generated to engine emissions.

2. **Biofuel use:** Further research into the use of biofuel together with battery electric vehicles (BEV) can be pursued. The use of range extenders that exclusively use biofuel can reduce the well-to-wheel CO₂ emissions of BEVs compared to using the grid electricity supply to recharge the vehicle's battery. The scalability of range extenders is also of interest with the possibility of being used in electric airplanes, drones and heavy goods vehicles. The use of second generation and third generation biofuels in vehicles can be investigated following the same methodology as presented in this research. The use of increased ethanol in spark ignition engines is also of interest, as the NO_x emissions is much lower than compression ignition engines and the addition of biofuel to the fuel blend can help mitigate spark ignition engines' higher CO₂ emissions when compared to compression ignition engines.

3. **Low temperature combustion:** The use of LTC for range extender applications is of interest as well as where dual fuel combustion is used in reducing emissions and increasing the efficiency of the internal combustion engine. Other LTC strategies which include dual fuel applications on larger compression ignition engines can also be investigated.

References

- [1] UNFCCC. *Paris Agreement* [online]. OJ L 282, 19.10.2016, p. 4–18. Available from: [http://eur-lex.europa.eu/legal-content/EN/TXT/PDF/?uri=CELEX:22016A1019\(01\)&from=EN](http://eur-lex.europa.eu/legal-content/EN/TXT/PDF/?uri=CELEX:22016A1019(01)&from=EN) [Accessed: 17 July 2017]. 2015.
- [2] Department for Business, Energy & Industrial Strategy. *Energy Trends March 2017*. London: The National Archives. 2017.
- [3] P. Clark. UK generates a day’s electricity without coal. *The Financial Times* [online] 22 April. Available from: <https://www.ft.com/content/8f65f54a-26a7-11e7-8691-d5f7e0cd0a16?mhq5j=e1> [Accessed 28 June 2017]. 2017.
- [4] Department for Transport. *Vehicle Licensing Statistics: Annual 2018*. Office of National Statistics. 2018.
- [5] J. O’Brien. The great diesel witch hunt? *Engine Technology International* [online] 1 September. Available from: http://www.engine-technology-international.com/magazine_archive.php [Accessed 28 June 2017]. 2016.
- [6] Mayor of London. The Mayor’s new £10 ‘Toxicity Charge’ for London’s most polluting cars [online]. Available from: <https://www.london.gov.uk/what-we-do/transport/mayors-new-ps10-toxicity-charge-londons-most-polluting-cars> [Accessed 28 June 2017]. 2017.
- [7] Department for Environment Food & Rural Affairs. *UK Plan for tackling roadside nitrogen dioxide concentrations*. London: The National Archives. 2017.
- [8] UNFCCC. *The Paris Agreement and NDCs* [online]. Available from: <https://unfccc.int/process/the-paris-agreement/nationally-determined-contributions/> [Accessed: 11 October 2018]. 2018.
- [9] European Union. *Directive 2009/28/EC of the European Parliament and of the Council of 23 April 2009 on the promotion of the use of energy from renewable sources and amending and subsequently repealing Directives 2001/77/EC and 2003/30/EC* [online]. OJ L 140, 5.6.2009, p. 16–62. Available from: <http://eur-lex.europa.eu/legal-content/EN/ALL/?uri=CELEX:32009L0028&qid=1498667012776> [Accessed: 28 June 2017]. 2009.
- [10] European Union. *Reducing CO2 emissions from passenger cars*. 2018. URL: https://ec.europa.eu/clima/policies/transport/vehicles/cars_en.
- [11] European Union. *Regulation (EU) No 333/2014 of the European Parliament and of the Council of 11 March 2014 amending Regulation (EC) No 443/2009 to define the modalities for reaching the 2020 target to reduce CO2 emissions from new passenger cars*. [online]. Available from: https://eur-lex.europa.eu/legal-content/EN/TXT/?uri=uriserv:OJ.L_.2014.103.01.0015.01.ENG [Accessed: 8 August 2018]. 2014.

- [12] European Union. *Commission Regulation (EU) No 459/2012 of 29 May 2012 amending Regulation (EC) No 715/2007 of the European Parliament and of the Council and Commission Regulation (EC) No 692/2008 as regards emissions from light passenger and commercial vehicles (Euro 6) Text with EEA relevance*. [online]. Available from: <https://eur-lex.europa.eu/legal-content/EN/TXT/?qid=1533650600700&uri=CELEX:32012R0459> [Accessed: 7 August 2017]. 2012.
- [13] European Union. *Regulation (EC) No 715/2007 of the European Parliament and of the Council of 20 June 2007 on type approval of motor vehicles with respect to emissions from light passenger and commercial vehicles (Euro 5 and Euro 6) and on access to vehicle repair and maintenance information (Text with EEA relevance)*. [online]. Available from: <https://eur-lex.europa.eu/legal-content/EN/ALL/?uri=CELEX%3A32007R0715> [Accessed: 7 August 2018]. 2007.
- [14] Department for Transport. *Vehicle Emissions Testing Programme* [online]. Available from: https://www.gov.uk/government/uploads/system/uploads/attachment_data/file/548148/vehicle-emissions-testing-programme-web.pdf [Accessed 29 June 2017]. 2016.
- [15] Department of Energy & Climate Change. *UK Renewable Energy Roadmap Update 2013*. London: The National Archives. URN: 13D/259. 2013.
- [16] Department for Business, Energy & Industrial Strategy. *Digest of UK Energy Statistics 2018*. Office of National Statistics. 2018.
- [17] The Renewable Transport Fuels and Greenhouse Gas Emissions Regulations 2018. SI 2018/374. 2018.
- [18] Department for Transport. *Renewable Transport Fuel Obligation statistics: period 9 2016/2017, report 6*. Office of National Statistics. 2018.
- [19] S. Behera, R. Singh, R. Arora, N. K. Sharma, M. Shukla, and S. Kumar. Scope of algae as third generation biofuels. *Frontiers in bioengineering and biotechnology*. 2 (2015), p. 90.
- [20] I. Ajjawi, J. Verruto, M. Aquí, L. B. Soriaga, J. Coppersmith, K. Kwok, L. Peach, E. Orchard, R. Kalb, W. Xu, *et al.* Lipid production in *Nannochloropsis gaditana* is doubled by decreasing expression of a single transcriptional regulator. *Nature biotechnology*. 35 (7) (2017), p. 647.
- [21] M. L. Randazzo and J. R. Sodr . Exhaust emissions from a diesel powered vehicle fuelled by soybean biodiesel blends (B3–B20) with ethanol as an additive (B20E2–B20E5). *Fuel*. 90 (1) (2011), pp. 98–103. DOI: 10.1016/j.fuel.2010.09.010.
- [22] M. Tuner. *Review and Benchmarking of Alternative Fuels in Conventional and Advanced Engine Concepts with Emphasis on Efficiency, CO₂, and Regulated Emissions*. Tech. rep. SAE Technical Paper, 2016. DOI: 10.4271/2016-01-0882.
- [23] M. Stow, M. McManus, and C. Bannister. A life cycle assessment comparison of rapeseed biodiesel and conventional diesel (2012). DOI: 10.1533/9780857094575.

- [24] D. Qi, L. Geng, H. Chen, Y. Z. Bian, J. Liu, and X. C. Ren. Combustion and performance evaluation of a diesel engine fueled with biodiesel produced from soybean crude oil. *Renewable Energy*. 34 (12) (2009), pp. 2706–2713. DOI: 10.1016/j.renene.2009.05.004.
- [25] S. Palash, H. Masjuki, M. Kalam, A. Atabani, I. R. Fattah, and A. Sanjid. Biodiesel production, characterization, diesel engine performance, and emission characteristics of methyl esters from *Aphanamixis polystachya* oil of Bangladesh. *Energy Conversion and Management*. 91 (2015), pp. 149–157. DOI: 10.1016/j.enconman.2014.12.009.
- [26] C. Bannister, J. Hawley, H. Ali, C. Chuck, P. Price, S. Chrysafi, A. Brown, and W. Pickford. The impact of biodiesel blend ratio on vehicle performance and emissions. *Proceedings of the Institution of Mechanical Engineers, Part D: Journal of Automobile Engineering*. 224 (3) (2010), pp. 405–421. DOI: 10.1243/09544070JAUTO1270.
- [27] B. Lin, J. Huang, and D. Huang. Experimental study of the effects of vegetable oil methyl ester on DI diesel engine performance characteristics and pollutant emissions. *Fuel*. 88 (9) (2009), pp. 1779–1785. DOI: 10.1016/j.fuel.2009.04.006.
- [28] J. Xue, T. E. Grift, and A. C. Hansen. Effect of biodiesel on engine performances and emissions. *Renewable and sustainable energy reviews*. 15 (2) (2011), pp. 1098–1116. DOI: 10.1016/j.rser.2010.11.016.
- [29] M. Lapuerta, O. Armas, and J. Rodriguez-Fernandez. Effect of biodiesel fuels on diesel engine emissions. *Progress in energy and combustion science*. 34 (2) (2008), pp. 198–223. DOI: 10.1016/j.peccs.2007.07.001.
- [30] E. Bakeas, G. Karavalakis, G. Fontaras, and S. Stournas. An experimental study on the impact of biodiesel origin on the regulated and PAH emissions from a Euro 4 light-duty vehicle. *Fuel*. 90 (11) (2011), pp. 3200–3208.
- [31] L. Zhu, C. Cheung, W. Zhang, and Z. Huang. Combustion, performance and emission characteristics of a DI diesel engine fueled with ethanol–biodiesel blends. *Fuel*. 90 (5) (2011), pp. 1743–1750. DOI: 10.1016/j.fuel.2011.01.024.
- [32] A. Tsolakis. Effects on particle size distribution from the diesel engine operating on RME–biodiesel with EGR. *Energy & Fuels*. 20 (4) (2006), pp. 1418–1424.
- [33] S. Lahane and K. Subramanian. Effect of different percentages of biodiesel–diesel blends on injection, spray, combustion, performance, and emission characteristics of a diesel engine. *Fuel*. 139 (2015), pp. 537–545. DOI: 10.1016/j.fuel.2014.09.036.
- [34] D. B. Hulwan and S. V. Joshi. Performance, emission and combustion characteristic of a multicylinder DI diesel engine running on diesel–ethanol–biodiesel blends of high ethanol content. *Applied Energy*. 88 (12) (2011), pp. 5042–5055. DOI: 10.1016/j.apenergy.2011.07.008.
- [35] J. Huang, Y. Wang, S. Li, A. P. Roskilly, H. Yu, and H. Li. Experimental investigation on the performance and emissions of a diesel engine fuelled with ethanol–diesel blends. *Applied Thermal Engineering*. 29 (11–12) (2009), pp. 2484–2490. DOI: 10.1016/j.applthermaleng.2008.12.016.

- [36] L. Xing-cai, Y. Jian-Guang, Z. Wu-Gao, and H. Zhen. Effect of cetane number improver on heat release rate and emissions of high speed diesel engine fueled with ethanol–diesel blend fuel. *Fuel*. 83 (14–15) (2004), pp. 2013–2020. DOI: 10.1016/j.fuel.2004.05.003.
- [37] D. C. Rakopoulos, C. D. Rakopoulos, E. C. Kakaras, and E. G. Giakoumis. Effects of ethanol–diesel fuel blends on the performance and exhaust emissions of heavy duty DI diesel engine. *Energy Conversion and Management*. 49 (11) (2008), pp. 3155–3162. DOI: 10.1016/j.enconman.2008.05.023.
- [38] S. Shahir, H. Masjuki, M. Kalam, A. Imran, and A. Ashraful. Performance and emission assessment of diesel–biodiesel–ethanol/ bioethanol blend as a fuel in diesel engines: A review. *Renewable and Sustainable Energy Reviews*. 48 (2015), pp. 62–78. DOI: 10.1016/j.rser.2015.03.049.
- [39] P. Kwanchareon, A. Luengnaruemitchai, and S. Jai-In. Solubility of a diesel–biodiesel–ethanol blend, its fuel properties, and its emission characteristics from diesel engine. *Fuel*. 86 (7–8) (2007), pp. 1053–1061. DOI: 10.1016/j.fuel.2006.09.034.
- [40] B. He, S. Shuai, J. Wang, and H. He. The effect of ethanol blended diesel fuels on emissions from a diesel engine. *Atmospheric Environment*. 37 (35) (2003), pp. 4965–4971. DOI: 10.1016/j.atmosenv.2003.08.029.
- [41] A. S. van Niekerk, B. Drew, N. Larsen, and P. J. Kay. Influence of blends of diesel and renewable fuels on compression ignition engine emissions over transient engine conditions. *Applied Energy*. 255 (2019). DOI: 10.1016/j.apenergy.2019.113890.
- [42] S. H. Park, H. K. Suh, and C. S. Lee. Nozzle flow and atomization characteristics of ethanol blended biodiesel fuel. *Renewable energy*. 35 (1) (2010), pp. 144–150.
- [43] M. Mofijur, M. Rasul, J. Hyde, A. Azad, R. Mamat, and M. Bhuiya. Role of biofuel and their binary (diesel–biodiesel) and ternary (ethanol–biodiesel–diesel) blends on internal combustion engines emission reduction. *Renewable and Sustainable Energy Reviews*. 53 (2016), pp. 265–278. DOI: 10.1016/j.rser.2015.08.046.
- [44] G. Khoobakht, G. Najafi, M. Karimi, and A. Akram. Optimization of operating factors and blended levels of diesel, biodiesel and ethanol fuels to minimize exhaust emissions of diesel engine using response surface methodology. *Applied Thermal Engineering*. 99 (2016), pp. 1006–1017. DOI: 10.1016/j.applthermaleng.2015.12.143.
- [45] N. Yilmaz, F. M. Vigil, A. B. Donaldson, and T. Darabseh. Investigation of CI engine emissions in biodiesel–ethanol–diesel blends as a function of ethanol concentration. *Fuel*. 115 (2014), pp. 790–793. DOI: 10.1016/j.fuel.2013.08.012.
- [46] T. Prakash, V. E. Geo, L. J. Martin, and B. Nagalingam. Effect of ternary blends of bio-ethanol, diesel and castor oil on performance, emission and combustion in a CI engine. *Renewable energy*. 122 (2018), pp. 301–309. DOI: 10.1016/j.renene.2018.01.070.

- [47] H. Srikanth, J. Venkatesh, S. Godiganur, B. Manne, S. Bharath Kumar, and S. Spurthy. Combustion, performance, and emission characteristics of dairy-washed milk scum biodiesel in a dual cylinder compression ignition engine. *Energy Sources, Part A: Recovery, Utilization, and Environmental Effects* (2019), pp. 1–18. DOI: 10.1080/15567036.2019.1618996.
- [48] M. Zheng, M. C. Mulenga, G. T. Reader, M. Wang, D. S. Ting, and J. Tjong. Biodiesel engine performance and emissions in low temperature combustion. *Fuel*. 87 (6) (2008), pp. 714–722. DOI: 10.1016/j.fuel.2007.05.039.
- [49] U. Asad and M. Zheng. Efficacy of EGR and boost in single-injection enabled low temperature combustion. *SAE International Journal of Engines*. 2 (2009-01-1126) (2009), pp. 1085–1097. DOI: 10.4271/2009-01-1126.
- [50] N. Ladommatos, S. Abdelhalim, and H. Zhao. The effects of exhaust gas recirculation on diesel combustion and emissions. *International Journal of Engine Research*. 1 (1) (2000), pp. 107–126. DOI: 10.1243/1468087001545290.
- [51] H. Huang, Q. Liu, Q. Wang, C. Zhou, C. Mo, and X. Wang. Experimental investigation of particle emissions under different EGR ratios on a diesel engine fueled by blends of diesel/gasoline/n-butanol. *Energy Conversion and Management*. 121 (2016), pp. 212–223.
- [52] T. He, Z. Chen, L. Zhu, and Q. Zhang. The influence of alcohol additives and EGR on the combustion and emission characteristics of diesel engine under high-load condition. *Applied Thermal Engineering*. 140 (2018), pp. 363–372.
- [53] E. Plamondon and P. Seers. Parametric study of pilot–main injection strategies on the performance of a light-duty diesel engine fueled with diesel or a WCO biodiesel–diesel blend. *Fuel*. 236 (2019), pp. 1273–1281.
- [54] S. d’Ambrosio and A. Ferrari. Potential of double pilot injection strategies optimized with the design of experiments procedure to improve diesel engine emissions and performance. *Applied Energy*. 155 (2015), pp. 918–932. DOI: 10.1016/j.apenergy.2015.06.050.
- [55] S. Biswas, M. Bakshi, G. Shankar, and A. Mukhopadhyay. *Optimization of Multiple Injection Strategies to Improve BSFC Performance of a Common Rail Direct Injection Diesel Engine*. Tech. rep. SAE Technical Paper, 2016. DOI: 10.4271/2016-28-0002.
- [56] P. Carlucci, A. Ficarella, and D. Laforgia. *Effects of pilot injection parameters on combustion for common rail diesel engines*. Tech. rep. SAE Technical Paper, 2003. DOI: 10.4271/2003-01-0700.
- [57] Q. Zhang, R. M. Ogren, and S.-C. Kong. *Trade-Offs Between Emissions and Efficiency for Multiple Injections of Neat Biodiesel in a Turbocharged Diesel Engine Using an Enhanced PSO-GA Optimization Strategy*. Tech. rep. SAE Technical Paper, 2016. DOI: 10.4271/2016-01-0630.
- [58] K. Mathivanan, J. Mallikarjuna, and A. Ramesh. Influence of multiple fuel injection strategies on performance and combustion characteristics of a diesel fuelled HCCI engine—An experimental investigation. *Experimental Thermal and Fluid Science*. 77 (2016), pp. 337–346. DOI: 10.1016/j.expthermflusci.2016.05.010.

- [59] N. Horibe and T. Ishiyama. *Relations among NO_x, pressure rise rate, HC and CO in LTC operation of a diesel engine*. Tech. rep. SAE Technical Paper, 2009.
- [60] A. S. van Niekerk, B. Drew, N. Larsen, and P. J. Kay. Optimisation of Low Temperature Combustion Technology, for Future Drive Cycles, using a Factorial Design of Experiments. *SAE International Journal of Engines*. (2019-01-2171) (2019).
- [61] J. I. Ramos. *Internal combustion engine modeling*. Hemisphere publishing corporation, 1989.
- [62] E. J. López and N. M. Nigro. Validation of a 0D/1D computational code for the design of several kind of internal combustion engines. *Latin American applied research*. 40 (2) (2010), pp. 175–184.
- [63] W. R. da Silva Trindade and R. G. dos Santos. *Combustion Modeling Applied to Engines Using a 1D Simulation Code*. Tech. rep. SAE Technical Paper, 2016.
- [64] G. Woschni. *A universally applicable equation for the instantaneous heat transfer coefficient in the internal combustion engine*. Tech. rep. SAE Technical paper, 1967.
- [65] K. Qi, L. Feng, X. Leng, B. Du, and W. Long. Simulation of quasi-dimensional combustion model for predicting diesel engine performance. *Applied Mathematical Modelling*. 35 (2) (2011), pp. 930–940.
- [66] S. Awad, E. G. Varuvel, K. Loubar, and M. Tazerout. Single zone combustion modeling of biodiesel from wastes in diesel engine. *Fuel*. 106 (2013), pp. 558–568.
- [67] F. Maroteaux, C. Saad, and F. Aubertin. Development and validation of double and single Wiebe function for multi-injection mode Diesel engine combustion modelling for hardware-in-the-loop applications. *Energy Conversion and Management*. 105 (2015), pp. 630–641.
- [68] N. Watson, A. Pilley, and M. Marzouk. *A combustion correlation for diesel engine simulation*. Tech. rep. SAE Technical Paper, 1980. DOI: 10.4271/800029.
- [69] F. Maroteaux and C. Saad. Diesel engine combustion modeling for hardware in the loop applications: Effects of ignition delay time model. *Energy*. 57 (2013), pp. 641–652.
- [70] B. R. Prasath, P. Tamilporai, and M. F. Shabir. Analysis of combustion, performance and emission characteristics of low heat rejection engine using biodiesel. *International Journal of Thermal Sciences*. 49 (12) (2010), pp. 2483–2490.
- [71] A. Piano, F. Millo, G. Boccardo, M. Rafigh, A. Gallone, and M. Rimondi. *Assessment of the Predictive Capabilities of a Combustion Model for a Modern Common Rail Automotive Diesel Engine*. Tech. rep. SAE Technical Paper, 2016.
- [72] C. Olikara and G. L. Borman. *A computer program for calculating properties of equilibrium combustion products with some applications to IC engines*. Tech. rep. SAE Technical Paper, 1975.

- [73] R. Way. Methods for determination of composition and thermodynamic properties of combustion products for internal combustion engine calculations. *Proceedings of the Institution of Mechanical Engineers*. 190 (1) (1976), pp. 687–697.
- [74] H. K. Newhall. Kinetics of engine-generated nitrogen oxides and carbon monoxide. *Symposium (International) on Combustion*. Vol. 12. 1. Elsevier. 1969, pp. 603–613.
- [75] C. K. Westbrook and F. L. Dryer. Simplified reaction mechanisms for the oxidation of hydrocarbon fuels in flames. *Combustion science and technology*. 27 (1-2) (1981), pp. 31–43.
- [76] N. L. Bagal, C. J. Rutland, D. E. Foster, K. Narayanaswamy, and Y. He. CO emission model for an integrated diesel engine, emissions, and exhaust aftertreatment system level model. *SAE International Journal of Engines*. 2 (1) (2009), pp. 1460–1472.
- [77] Z. Petranović, M. Vujanović, and N. Duić. Towards a more sustainable transport sector by numerically simulating fuel spray and pollutant formation in diesel engines. *Journal of cleaner production*. 88 (2015), pp. 272–279.
- [78] Y. Zeldovich, D. Frank-Kamenetskii, and P. Sadovnikov. *Oxidation of nitrogen in combustion*. Publishing House of the Acad of Sciences of USSR, 1947.
- [79] J. B. Heywood. *Internal Combustion Engine Fundamentals*. McGraw-Hill New York, 1988.
- [80] G. Kökkülünk, G. Gonca, V. Ayhan, I. Cesur, and A. Parlak. Theoretical and experimental investigation of diesel engine with steam injection system on performance and emission parameters. *Applied Thermal Engineering*. 54 (1) (2013), pp. 161–170.
- [81] G. Gonca, B. Sahin, A. Parlak, Y. Ust, V. Ayhan, İ. Cesur, and B. Boru. Theoretical and experimental investigation of the Miller cycle diesel engine in terms of performance and emission parameters. *Applied Energy*. 138 (2015), pp. 11–20.
- [82] G. Kosmadakis, D. Rakopoulos, and C. Rakopoulos. Investigation of nitric oxide emission mechanisms in a SI engine fueled with methane/hydrogen blends using a research CFD code. *International Journal of Hydrogen Energy*. 40 (43) (2015), pp. 15088–15104.
- [83] A. Datta and B. K. Mandal. Impact of alcohol addition to diesel on the performance combustion and emissions of a compression ignition engine. *Applied thermal engineering*. 98 (2016), pp. 670–682.
- [84] C. Fenimore. Formation of nitric oxide in premixed hydrocarbon flames. *Symposium (International) on Combustion*. Vol. 13. Elsevier. 1971, pp. 373–380.
- [85] Z. Petranović, T. Bešenić, M. Vujanović, and N. Duić. Modelling pollutant emissions in diesel engines, influence of biofuel on pollutant formation. *Journal of environmental management*. 203 (2017), pp. 1038–1046.

- [86] R. Cheung, M. Letrich, R. Groselak, and M. Brezina. *Exhaust System Structural Vibration and Muffler Shell Noise Prediction due to Gas Pulsations in a 2.0l 4Cyl DI Diesel Engine* [Presentation Ricardo EUC 2015, Prague]. Available from: <https://software.ricardo.com/resources/exhaust-system-structural-vibration-muffler-shel> [Accessed 22 December 2017]. 2015.
- [87] J. Stokes, T. Lake, and R. Osborne. *A gasoline engine concept for improved fuel economy-The lean boost system*. Tech. rep. SAE Technical Paper, 2000. DOI: 10.4271/2000-01-2902.
- [88] K. Kim and D. Kim. Improving the NO_x-BSFC Trade Off of a Turbocharged Large Diesel Engine Using Performance Simulation. *ASME 2002 Internal Combustion Engine Division Fall Technical Conference*. American Society of Mechanical Engineers. 2002, pp. 159–165. DOI: 10.1115/ICEF2002-493.
- [89] A. Boretti. Advantages of converting diesel engines to run as dual fuel ethanol–diesel. *Applied Thermal Engineering*. 47 (5) (2012), pp. 1–9. DOI: 10.1016/j.applthermaleng.2012.04.037.
- [90] A. Mustafa, R. F. Martinez-Botas, A. Pesiridis, M. S. Chiong, and S. Rajoo. Assessment of turbocharger turbine unsteady flow modelling methodology on engine performance. *ASME 2014 12th Biennial Conference on Engineering Systems Design and Analysis*. American Society of Mechanical Engineers. 2014, V001T02A014–V001T02A014.
- [91] C. Avola, P. Dimitriou, R. Burke, and C. Copeland. Preliminary DoE Analysis and Control of Mapping Procedure for a Turbocharger on an Engine Gas-Stand. *ASME Turbo Expo 2016: Turbomachinery Technical Conference and Exposition*. American Society of Mechanical Engineers. 2016, V008T23A008–V008T23A008.
- [92] W. Guan, V. Pedrozo, H. Zhao, Z. Ban, and T. Lin. *Investigation of EGR and Miller Cycle for NO_x Emissions and Exhaust Temperature Control of a Heavy-Duty Diesel Engine*. Tech. rep. SAE Technical Paper, 2017. DOI: 10.4271/2017-01-2227.
- [93] Ricardo. *IGNITE User Manual*. Ricardo Software, 2016.
- [94] Ricardo. *WAVE User Manual*. Ricardo Software, 2016.
- [95] R. Feldman. *Epistemology. Foundations of Philosophy Series*. 2003.
- [96] A. B. Ryan. Post-positivist approaches to research. *Researching and Writing your Thesis: a guide for postgraduate students* (2006), pp. 12–26.
- [97] Department for Transport. *Statistical data set Cars (VEH02)*. [online]. 2018.
- [98] M. Lopes, L. Serrano, I. Ribeiro, P. Cascão, N. Pires, S. Rafael, L. Tarelho, A. Monteiro, T. Nunes, M. Evtyugina, *et al.* Emissions characterization from EURO 5 diesel/biodiesel passenger car operating under the new European driving cycle. *Atmospheric environment*. 84 (2014), pp. 339–348.
- [99] L. Serrano, M. Lopes, N. Pires, I. Ribeiro, P. Cascão, L. Tarelho, A. Monteiro, O. Nielsen, M. G. da Silva, and C. Borrego. Evaluation on effects of using low biodiesel blends in a EURO 5 passenger vehicle equipped with a common-rail diesel engine. *Applied Energy*. 146 (2015), pp. 230–238.
- [100] C. Beatrice, P. Napolitano, and C. Guido. Injection parameter optimization by DoE of a light-duty diesel engine fed by Bio-ethanol/RME/diesel blend. *Applied Energy*. 113 (2014), pp. 373–384.

- [101] R. Suarez-Bertoa, M. Kousoulidou, M. Clairotte, B. Giechaskiel, J. Nuotimäki, T. Sarjovaara, and L. Lonza. Impact of HVO blends on modern diesel passenger cars emissions during real world operation. *Fuel*. 235 (2019), pp. 1427–1435.
- [102] M. Lehtimäki. Modified Aerosol Detector. *Aerosols in Mining and Industrial Work Environment*. 3 (1983), pp. 1135–1143.
- [103] A. Rostedt, A. Arffman, K. Janka, J. Yli-Ojanperä, and J. Keskinen. Characterization and response model of the PPS-M aerosol sensor. *Aerosol Science and Technology*. 48 (10) (2014), pp. 1022–1030.
- [104] R. Burke, E. Chappell, M. Gee, and R. Williams. Understanding the factors that influence testing precision for modern diesel vehicles. In: *Internal Combustion Engines 2017*, Birmingham, UK, 6-7 December 2017. 2017.
- [105] D. R. Lancaster, R. B. Krieger, and J. H. Lienesch. *Measurement and analysis of engine pressure data*. Tech. rep. SAE Technical paper, 1975. DOI: 10.4271/750026.
- [106] R. B. R. da Costa, R. L. Franco, C. A. Gomes, R. d. O. A. Coelho, and R. M. Valle. *Experimental Methodology and Numerical Simulation of Intake Valves Discharge Coefficients for a Single Cylinder Research Engine*. Tech. rep. SAE Technical Paper, 2015.
- [107] G. Mellios, S. Hausberger, M. Keller, Z. Samaras, and L. Ntziachristos. Parameterisation of fuel consumption and CO₂ emissions of passenger cars and light commercial vehicles for modelling purposes. *Publications Office of the European Union*. 2 (2011), pp. 16–18. DOI: 2788/58009.
- [108] D. Kunninger. The development of a vehicle and road load simulation for an engine dynamometer intended for emissions testing and powertrain development. PhD thesis. 2013.
- [109] European Union. *Council Directive 91/441/EEC of 26 June 1991 amending Directive 70/220/EEC on the approximation of the laws of the Member States relating to measures to be taken against air pollution by emissions from motor vehicles* [online]. OJ L 242 , 30.08.1991 p. 1-106. Available from: <http://eur-lex.europa.eu/legal-content/EN/TXT/?qid=1499086220026&uri=CELEX:31991L0441> [Accessed: 28 June 2017]. 2009.
- [110] Workshop Manuals. Ford Workshop Manuals. Available from: http://workshop-manuals.com/ford/transit_2006.5_04.2006 [Accessed 28 June 2017]. 2017.
- [111] A. S. Van Niekerk, P. J. Kay, B. Drew, and N. Larsen. Development of multi-fidelity powertrain simulation for future legislation. In: *Internal Combustion Engines 2017*, Birmingham, UK, 6-7 December 2017. Available from: <http://eprints.uwe.ac.uk/33589>. (2017).
- [112] S. Leonhardt, C. Schmidt, K. Voigt, and R. Isermann. Real-time simulation of drive chains for use in dynamical engine test stands. *1992 American Control Conference*. IEEE. 1992, pp. 521–527.
- [113] D. E. Cole. *Elementary vehicle dynamics*. Department of Mechanical Engineering, the University of Michigan, 1972.
- [114] Minitab. *Minitab 17 Statistical Software [Computer software]*. Available from: www.minitab.com. 2010.

- [115] L. Chen, Z. Zhang, W. Gong, and Z. Liang. Quantifying the effects of fuel compositions on GDI-derived particle emissions using the optimal mixture design of experiments. *Fuel*. 154 (15) (2015), pp. 252–260. DOI: 10.1016/j.fuel.2015.03.081.
- [116] J. A. Cornell. *Experiments with mixtures: designs, models, and the analysis of mixture data*. Vol. 403. John Wiley & Sons, 2011.
- [117] M. Lapuerta, O. Armas, and R. Garcia-Contreras. Stability of diesel–bioethanol blends for use in diesel engines. *Fuel*. 86 (10–11) (2007), pp. 1351–1357. DOI: 10.1016/j.fuel.2006.11.042.
- [118] A. C. Hansen, Q. Zhang, and P. W. Lyne. Ethanol–diesel fuel blends — a review. *Bioresource Technology*. 96 (3) (2005), pp. 277–285. DOI: 10.1016/j.biortech.2004.04.007.
- [119] S. Fernando and M. Hanna. Development of a novel biofuel blend using ethanol- biodiesel- diesel microemulsions: EB-diesel. *Energy & Fuels*. 18 (6) (2004), pp. 1695–1703. DOI: 10.1021/ef049865e.
- [120] H. Kim and B. Choi. Effect of ethanol–diesel blend fuels on emission and particle size distribution in a common-rail direct injection diesel engine with warm-up catalytic converter. *Renewable Energy*. 33 (10) (2008), pp. 2222–2228. DOI: 10.1016/j.renene.2008.01.002.
- [121] K. Ravikumar, S. Krishnan, S. Ramalingam, and K. Balu. Optimization of process variables by the application of response surface methodology for dye removal using a novel adsorbent. *Dyes and Pigments*. 72 (1) (2007), pp. 66–74. DOI: 10.1016/j.dyepig.2005.07.018.
- [122] F. Karimi, S. Rafiee, A. Taheri-Garavand, and M. Karimi. Optimization of an air drying process for Artemisia absinthium leaves using response surface and artificial neural network models. *Journal of the Taiwan Institute of Chemical Engineers*. 43 (1) (2012), pp. 29–39. DOI: 10.1016/j.jtice.2011.04.005.
- [123] O. M. I. Nwafor. Emission characteristics of diesel engine operating on rapeseed methyl ester. *Renewable Energy*. 29 (1) (2004), pp. 119–129. DOI: 10.1016/S0960-1481(03)00133-2.
- [124] A. Abu-Jrai, J. A. Yamin, H. Ala’a, and M. A. Hararah. Combustion characteristics and engine emissions of a diesel engine fueled with diesel and treated waste cooking oil blends. *Chemical Engineering Journal*. 172 (1) (2011), pp. 129–136. DOI: 10.1016/j.cej.2011.05.078.
- [125] H. An, W. M. Yang, A. Maghbouli, J. Li, S. K. Chou, and K. . Chua. Performance, combustion and emission characteristics of biodiesel derived from waste cooking oils. *Applied Energy*. 112 (2013), pp. 493–499. DOI: 10.1016/j.apenergy.2012.12.044.
- [126] I. Barabas, A. Todoruț, and D. Băldean. Performance and emission characteristics of an CI engine fueled with diesel–biodiesel–bioethanol blends. *Fuel*. 89 (12) (2010), pp. 3827–3832. DOI: 10.1016/j.fuel.2010.07.011.
- [127] S. Godiganur, C. S. Murthy, and R. P. Reddy. Performance and emission characteristics of a Kirloskar HA394 diesel engine operated on fish oil methyl esters. *Renewable Energy*. 35 (2) (2010), pp. 355–359. DOI: 10.1016/j.renene.2009.07.007.

- [128] S. Dev, H. B. Chaudhari, S. Gothekar, S. Juttu, N. H. Walke, and N. V. Marathe. *Review on advanced low temperature combustion approach for BS VI*. Tech. rep. SAE paper 2017-26-0042, 2017.
- [129] The Renewable Transport Fuel Obligations Order. SI 2007/3072. 2007.
- [130] Department of Business, Energy & Industrial Strategy. *Greenhouse gas reporting: conversion factors 2018*. [online]. 2018.
- [131] NIST/SEMATECH. *e-Handbook of Statistical Methods*. Available from: <http://www.itl.nist.gov/div898/handbook/> [Accessed 1 December 2017]. 2013.
- [132] M. P. Musculus, P. C. Miles, and L. M. Pickett. Conceptual models for partially premixed low-temperature diesel combustion. *Progress in Energy and Combustion Science*. 39 (2-3) (2013), pp. 246–283.
- [133] D. C. Montgomery. *Design and Analysis of Experiments*. John Wiley & Sons, 2017.
- [134] M. Pandian, S. Sivapirakasam, and M. Udayakumar. Investigation on the effect of injection system parameters on performance and emission characteristics of a twin cylinder compression ignition direct injection engine fuelled with pongamia biodiesel – diesel blend using response surface methodology. *Applied Energy*. 88 (8) (2011), pp. 2663–2676.
- [135] Z. Win, R. Gakkhar, S. Jain, and M. Bhattacharya. Investigation of diesel engine operating and injection system parameters for low noise, emissions, and fuel consumption using Taguchi methods. *Proceedings of the Institution of Mechanical Engineers, Part D: Journal of Automobile Engineering*. 219 (10) (2005), pp. 1237–1251.
- [136] T. Ganapathy, K. Murugesan, and R. Gakkhar. Performance optimization of Jatropa biodiesel engine model using Taguchi approach. *Applied Energy*. 86 (11) (2009), pp. 2476–2486.
- [137] U. Asad, P. Divekar, M. Zheng, and J. Tjong. *Low temperature combustion strategies for compression ignition engines: operability limits and challenges*. Tech. rep. SAE Technical Paper, 2013.
- [138] K. Gill, C. Marriner, K. Sison, and H. Zhao. *In-cylinder studies of multiple diesel fuel injection in a single cylinder optical engine*. Tech. rep. SAE Technical Paper, 2005.
- [139] R. Ehleskog, R. L. Ochoterena, and S. Andersson. *Effects of multiple injections on engine-out emission levels including particulate mass from an HSDI diesel engine*. Tech. rep. SAE Technical Paper, 2007.
- [140] European Union. *COMMISSION REGULATION (EU) 2017/1151 of 1 June 2017 supplementing Regulation (EC) No 715/2007 of the European Parliament and of the Council on type-approval of motor vehicles with respect to emissions from light passenger and commercial vehicles (Euro 5 and Euro 6) and on access to vehicle repair and maintenance information, amending Directive 2007/46/EC of the European Parliament and of the Council, Commission Regulation (EC) No 692/2008 and Commission Regulation (EU) No 1230/2012 and repealing Commission Regulation (EC) No 692/2008* [online]. OJ L 175, 7.7.2017, p. 1–643. Available from: <https://eur-lex.europa.eu/legal->

- content/EN/TXT/PDF/?uri=CELEX:32017R1151&qid=1531213237207&from=EN [Accessed: 10 July 2018]. 2017.
- [141] T. Bohl, A. Smallbone, G. Tian, and A. P. Roskilly. Particulate number and NO_x trade-off comparisons between HVO and mineral diesel in HD applications. *Fuel*. 215 (2018), pp. 90–101.

Appendix A

Supplementary information

Table A.1: Description of the elements used in Ricardo WAVE.

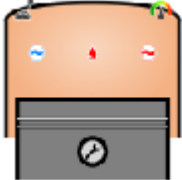
Image	Element name	Description
	Actuator	An actuator is used to return values from the control system as an input to the flow system. Can be used to model real hardware.
	Ambient	The ambient element represents an infinite reservoir of air at a given pressure and temperature.
	Compressor	The compressor is a turbo junction element used to change the condition of the flow across a planar boundary.
	Cylinder	Used to model the cylinders of a standard IC engine. It is a zero-dimensional element that represent a volume changing with time. Cylinder geometry values are required as input.

Table A.1 continued from previous page

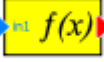
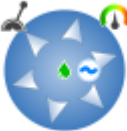
Image	Element name	Description
	Duct	Ducts are used to represent the sections of pipe networks where the flow can be treated as one-dimensional.
	Engine block	Used to define basic engine geometry and properties.
	Function	A signal processing element used to evaluate a mathematical or logical expression which uses input signals to generate an output signal.
	Gain	A signal processing element used to multiply one or more inputs with a fixed gain factor.
	Injectors	The injector element can be attached to a cylinder, duct or junction. Input values can include, air fuel ratio, start of injection, injection rate or injection duration.
	Interpolation map	A signal processing element used to process one or more input signals into an output signal by linearly interpolating between defined points in a map.
	Y-junction	The element represents a spherical volume which may be the junction of multiple ducts.

Table A.1 continued from previous page

Image	Element name	Description
	Orifice	The element is used to connect two adjacent ducts, which can have different diameters.
	PID controller	A signal processing element used to drive a model to its target point and hold it there while the flow model converges.
	Receive signal	A source in the control system used to receive signals from a send element elsewhere in the model.
	Send signal	A sink in the control system used to send signals to one or more receive elements elsewhere in the model.
	Sensor	An element used to take measurements of variables in the flow system. can be used as input to controllers or an external program.
	Source	An element in the control system used to generate a signal which feeds into a control system. Can create a signal from a fixed value or a quantity from WAVE's summary file.
	Subgroup	A function used to group elements together under one element icon.

Table A.1 continued from previous page

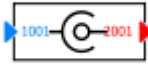
Image	Element name	Description
	Turbine	A turbo junction element used to represent a turbine. Changes the condition of the flow across a planar boundary.
	Turbo shaft	The turbo shaft is used to connect and drive turbo junctions. It is a rigid body with a rotational speed and inertia.
	Valves	The valve element is a variable diameter orifice. Valve behaviour is controlled by the valve sub-models.
	Wiring connector	An element used to link control network elements to external processes such as Ricardo IGNITE and Matlab.

Table A.2: Description of the elements used in Ricardo IGNITE.

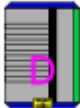
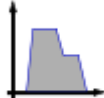
Image	Element name	Description
	Clutch	An element used to model the friction interface used to transfer torque between two rotating flanges.
	Cycle driver	A specialised controller that provides acceleration and brake signals to a vehicle simulation following a drive cycle profile.
	Discrete controller	Coordinates control between multiple components to ensure the correct signals are available.
	Drive cycle	The element is used to output the vehicle speed required at the current simulation time to follow a prescribed drive cycle.
	Gear selector	Provides a target gear number signal to the controller as a function of time.
	Discrete gearbox	The element is used to model a manual gearbox with gear ratios as one of the inputs required.
	Shaft	Represents a flexible shaft with linear stiffness and damping without any inertia.

Table A.2 continued from previous page

Image	Element name	Description
	Vehicle	Represents a one-dimensional mass with drag forces from rolling resistance and aerodynamic resistance.
	WAVE block	Used to represent co-simulation with a WAVE engine simulation.

Table A.3: Target fuel pressure

TPS/RPM	500	750	1000	1250	1500	1750	2000	2250	2500	2750	3000	3250	3500	3750	4000	4250	4500
0.00	300	300	300	300	300	270	250	250	250	250	250	250	250	250	250	250	250
0.78	300	300	300	300	300	270	250	250	250	250	250	250	250	250	250	250	250
2.73	400	400	350	350	350	340	310	310	310	310	310	310	310	310	310	310	310
4.29	400	400	370	370	370	370	370	370	370	370	370	370	370	370	370	370	370
7.02	450	450	400	400	400	400	410	410	410	410	410	410	410	410	410	410	410
9.75	450	450	400	400	400	410	430	430	430	430	430	430	430	430	430	430	430
14.82	450	450	400	400	440	460	490	500	500	500	500	500	500	500	500	500	500
30.03	450	450	410	430	480	530	560	580	580	580	580	600	600	600	600	600	600
39.78	470	470	460	490	540	580	620	640	660	660	680	700	700	720	730	730	730
54.60	540	540	540	570	620	650	700	740	770	790	820	840	850	870	900	900	900
69.42	600	600	600	700	750	810	870	900	930	950	1000	1090	1120	1150	1190	1200	1220
84.63	600	600	600	740	850	920	980	1050	1090	1130	1200	1300	1380	1430	1480	1520	1550
99.45	600	600	600	780	890	980	1030	1110	1150	1200	1310	1460	1560	1640	1750	1800	1800

Table A.4: Main fuel pulse width.

uS	500	750	1000	1250	1500	1750	2000	2250	2500	2750	3000	3250	3500	3750	4000	4250	4500
0.00	855	760	665	589	513	475	475	456	456	456	437	418	399	380	342	304	247
0.39	855	760	665	608	532	494	494	475	475	475	456	437	418	380	361	323	266
1.56	893	836	779	703	646	608	570	551	551	532	513	494	475	456	437	399	304
3.12	950	893	817	760	703	665	608	608	589	570	570	551	532	513	494	456	399
5.46	1007	950	874	817	760	722	684	665	665	646	646	627	608	589	570	551	475
7.80	1045	988	912	855	817	779	741	722	722	722	703	684	665	646	627	589	551
11.31	1064	1007	950	912	874	855	836	817	798	779	779	760	741	722	703	665	627
15.60	1083	1026	988	969	969	969	950	931	912	893	874	855	836	798	779	741	703
21.45	1102	1045	1045	1045	1064	1064	1064	1064	1045	1007	950	931	893	855	836	817	779
28.47	1121	1064	1083	1102	1121	1140	1140	1121	1102	1064	1007	950	912	893	855	817	779
36.66	1121	1064	1083	1121	1159	1178	1197	1197	1178	1121	1064	988	950	912	874	817	798
47.19	1121	1064	1102	1197	1216	1235	1254	1254	1235	1197	1102	1007	950	912	874	836	817
58.50	1121	1064	1102	1197	1254	1273	1311	1311	1254	1197	1121	1045	988	931	893	855	817
71.37	1121	1064	1102	1197	1273	1311	1349	1330	1273	1216	1140	1064	1007	931	893	855	836
85.02	1121	1064	1102	1197	1292	1330	1349	1349	1311	1235	1140	1083	1026	950	912	855	836
99.45	1121	1064	1102	1197	1292	1349	1349	1349	1330	1254	1159	1121	1045	950	912	855	836

Table A.5: Main injection start of injection.

bTDC	500	750	1000	1250	1500	1750	2000	2250	2500	2750	3000	3250	3500	3750	4000	4250	4500
0.00	4.0	4.0	4.0	5.0	6.5	8.5	18.0	20.0	20.0	22.0	24.0	24.0	24.0	24.0	24.0	24.0	24.0
0.39	4.0	4.0	4.0	5.0	6.5	8.5	18.0	20.0	20.0	22.0	24.0	24.0	24.0	24.0	24.0	24.0	24.0
1.56	4.0	4.0	4.0	5.0	6.5	8.5	18.0	20.0	20.0	22.0	24.0	24.0	24.0	24.0	24.0	24.0	24.0
3.12	4.0	4.0	4.0	5.0	6.5	8.5	18.0	20.0	20.0	22.0	24.0	24.0	24.0	24.0	24.0	24.0	24.0
5.46	4.0	4.0	4.0	5.0	6.5	8.5	18.0	20.0	20.0	22.0	24.0	24.0	24.0	24.0	24.0	24.0	24.0
7.80	4.0	4.0	4.0	5.0	6.5	8.5	18.0	20.0	20.0	24.0	24.0	24.0	24.0	24.0	24.0	24.0	24.0
11.31	4.0	4.0	4.0	5.0	6.5	8.5	18.0	20.0	20.0	24.0	24.0	24.0	26.0	26.0	26.0	26.0	26.0
15.60	4.0	4.0	4.0	5.0	6.5	8.5	18.0	20.0	20.0	24.0	24.0	26.0	28.0	28.0	28.0	28.0	28.0
21.45	4.0	4.0	4.0	5.0	6.5	8.5	18.0	20.0	20.0	24.0	24.0	26.0	28.0	28.0	28.0	28.0	28.0
28.47	4.0	4.0	4.0	5.0	6.5	8.5	18.0	20.0	20.0	24.0	24.0	26.0	28.0	28.0	28.0	28.0	28.0
36.66	4.0	4.0	4.0	5.0	6.5	8.5	18.0	20.0	20.0	24.0	24.0	26.0	28.0	28.0	28.0	28.0	28.0
47.19	4.0	4.0	4.0	5.0	6.5	8.5	18.0	20.0	20.0	24.0	24.0	26.0	28.0	28.0	28.0	28.0	28.0
58.50	4.0	4.0	4.0	5.0	6.5	8.5	18.0	20.0	20.0	24.0	24.0	26.0	28.0	28.0	28.0	28.0	28.0
71.37	4.0	4.0	4.0	5.0	6.5	8.5	18.0	20.0	20.0	24.0	24.0	26.0	28.0	28.0	28.0	28.0	28.0
85.02	4.0	4.0	4.0	5.0	6.5	8.5	18.0	20.0	20.0	24.0	24.0	26.0	28.0	28.0	28.0	28.0	28.0
99.45	4.0	4.0	4.0	5.0	6.5	8.5	18.0	20.0	20.0	24.0	24.0	26.0	28.0	28.0	28.0	28.0	28.0

Table A.6: Pilot fuel pulse width.

TPS/RPM	500	750	1000	1250	1500	1750	2000	2250	2500	2750	3000	3250	3500	3750	4000	4250	4500
0.00	456	418	399	380	323	266	190	152	114	0	0	0	0	0	0	0	0
0.39	456	418	399	380	323	266	190	152	114	0	0	0	0	0	0	0	0
1.56	475	456	437	399	342	285	228	190	152	76	19	0	0	0	0	0	0
3.12	570	551	551	494	437	380	323	266	209	190	114	0	0	0	0	0	0
5.46	589	570	570	532	475	418	380	323	323	304	190	0	0	0	0	0	0
7.80	608	589	589	551	494	399	361	342	323	304	209	0	0	0	0	0	0
11.31	608	589	589	551	494	437	399	342	323	304	266	0	0	0	0	0	0
15.60	608	589	589	551	494	437	399	342	323	304	266	0	0	0	0	0	0
21.45	608	589	589	551	494	437	399	342	323	304	266	0	0	0	0	0	0
28.47	608	589	589	551	494	437	399	342	323	304	266	0	0	0	0	0	0
36.66	608	589	589	551	494	437	399	342	323	304	266	0	0	0	0	0	0
47.19	608	589	589	551	494	437	399	342	323	304	266	0	0	0	0	0	0
58.50	608	589	589	551	494	437	399	342	323	304	266	0	0	0	0	0	0
71.37	608	589	589	551	494	437	399	342	323	304	266	0	0	0	0	0	0
85.02	608	589	589	551	494	437	399	342	323	304	266	0	0	0	0	0	0
99.45	608	589	589	551	494	437	399	342	323	304	266	0	0	0	0	0	0

Table A.7: Pilot injection start of injection.

bTDC	500	750	1000	1250	1500	1750	2000	2250	2500	2750	3000	3250	3500	3750	4000	4250	4500
0.00	22.0	22.0	25.0	25.0	28.0	30.0	32.0	32.0	32.0	32.0	38.0	40.0	40.0	40.0	48.0	48.0	48.0
0.39	22.0	22.0	25.0	25.0	28.0	30.0	32.0	32.0	32.0	32.0	38.0	40.0	40.0	40.0	48.0	48.0	48.0
1.56	22.0	22.0	25.0	25.0	28.0	30.0	32.0	32.0	32.0	32.0	38.0	40.0	40.0	40.0	48.0	48.0	48.0
3.12	22.0	22.0	25.0	25.0	28.0	30.0	32.0	32.0	32.0	32.0	38.0	40.0	40.0	40.0	48.0	48.0	48.0
5.46	22.0	22.0	25.0	25.0	28.0	30.0	32.0	32.0	32.0	32.0	38.0	40.0	40.0	40.0	48.0	48.0	48.0
7.80	22.0	22.0	25.0	25.0	28.0	30.0	32.0	32.0	32.0	32.0	38.0	40.0	40.0	40.0	48.0	48.0	48.0
11.31	22.0	22.0	25.0	25.0	28.0	30.0	32.0	32.0	32.0	32.0	38.0	40.0	40.0	40.0	48.0	48.0	48.0
15.60	22.0	22.0	25.0	25.0	28.0	30.0	32.0	32.0	32.0	32.0	38.0	40.0	40.0	40.0	48.0	48.0	48.0
21.45	22.0	22.0	25.0	25.0	28.0	30.0	32.0	32.0	32.0	32.0	38.0	40.0	40.0	40.0	48.0	48.0	48.0
28.47	22.0	22.0	25.0	25.0	28.0	30.0	32.0	32.0	32.0	32.0	38.0	40.0	40.0	40.0	48.0	48.0	48.0
36.66	22.0	22.0	25.0	25.0	28.0	30.0	32.0	32.0	32.0	32.0	38.0	40.0	40.0	40.0	48.0	48.0	48.0
47.19	22.0	22.0	25.0	25.0	28.0	30.0	32.0	32.0	32.0	32.0	38.0	40.0	40.0	40.0	48.0	48.0	48.0
58.50	22.0	22.0	25.0	25.0	28.0	30.0	32.0	32.0	32.0	32.0	38.0	40.0	40.0	40.0	48.0	48.0	48.0
71.37	22.0	22.0	25.0	25.0	28.0	30.0	32.0	32.0	32.0	32.0	38.0	40.0	40.0	40.0	48.0	48.0	48.0
85.02	22.0	22.0	25.0	25.0	28.0	30.0	32.0	32.0	32.0	32.0	38.0	40.0	40.0	40.0	48.0	48.0	48.0
99.45	22.0	22.0	25.0	25.0	28.0	30.0	32.0	32.0	32.0	32.0	38.0	40.0	40.0	40.0	48.0	48.0	48.0

Table A.9: Statistical analysis of the maximum measured in-cylinder pressure.

Engine load (%)	n	Mean (bar)	StDev (bar)
230 rpm			
Motored	19	34.1	± 0.2
2000 rpm			
25	16	65.5	± 3.3
50	28	80.0	± 0.9
75	15	133.7	± 6.4
2500 rpm			
25	48	65.8	± 1.9
50	40	84.1	± 1.6
75	48	132.6	± 1.6
3000 rpm			
25	40	58.9	± 1.3
50	38	81.6	± 0.9
75	41	109.3	± 2.2

Table A.10: Statistical analysis for the maximum in-cylinder pressure for steady state tests using B2E9.

Engine load (MPa BMEP)	n	Mean (bar)	StDev (bar)
1500rpm			
0.2	100	48.3	±1.7
0.3	100	51.7	±2.8
0.4	100	54.2	±2.9
0.5	100	50.4	±2.2
1750rpm			
0.2	100	49.5	±0.5
0.3	100	51.3	±1.1
2000rpm			
0.2	100	47.6	±0.1
0.3	100	48.8	±0.1
0.4	100	51.7	±2.4
2250rpm			
0.2	100	47.0	±0.1
0.3	100	49.8	±0.1
0.4	100	62.5	±1.9
0.5	100	59.8	±2.6
0.6	100	60.9	±1.9
2500rpm			
0.3	100	56.8	±1.5
0.4	100	54.8	±1.6
0.5	100	53.3	±0.3
0.6	100	58.2	±0.3
2750rpm			
0.3	100	49.5	±0.2
0.4	100	51.1	±0.2
0.5	100	51.5	±0.3
0.6	100	64.7	±2.3
3000rpm			
0.4	100	50.0	±0.2
0.5	100	50.9	±1.6
0.6	100	66.8	±2.7
3250rpm			
0.4	100	51.0	±1.0
0.5	100	57.3	±1.7
0.6	100	76.0	±4.3

Table A.11: Statistical analysis of recorded points using the gas analyser.

Parameter	Mean	StDev	Mean	StDev	Mean	StDev	Mean	StDev	Mean	StDev
	Point 1		Point 2		Point 3		Point 4		Point 5	
CO ₂ (V)	0.96307	±0.00385	1.1074	±0.0058	1.1017	±0.0044	1.5555	±0.0041	1.5291	±0.0037
NO (V)	0.26356	±0.01602	0.14966	±0.00611	0.13226	±0.00517	0.30621	±0.00729	0.29436	±0.00582
NO ₂ (V)	-0.19609	±0.00333	-0.13887	±0.00391	-0.15004	±0.00371	-0.098748	±0.003390	-0.10661	±0.00348
Speed (rpm)	2001	±20	2500	±20	2501	±13	2497	±55	2507	±29
Torque (Nm)	70.1	±1.5	70.1	±1.1	70.0	±1.1	100.0	±2.4	100.0	±2.8
Oil (°C)	101.2	±0.1	105.1	±0.2	106.7	±0.2	107.2	±0.1	106.5	±0.1
Coolant (°C)	85.6	±0.1	86.2	±0.1	86.1	±0.1	86.5	±0.1	86.6	±0.1
	Point 6		Point 7		Point 8		Point 9		Point 10	
CO ₂ (V)	1.2436	±0.0064	1.7072	±0.0044	1.6964	±0.0050	1.3113	±0.0068	1.3049	±0.0044
NO (V)	0.39730	±0.00561	0.54947	±0.00727	0.58291	±0.00908	1.1598	±0.0094	1.1705	±0.0090
NO ₂ (V)	-0.12656	±0.00388	-0.074036	±0.003247	-0.081479	±0.003029	-0.16735	±0.00310	-0.16118	±0.00285
Speed (rpm)	3001	±20	3000	±20	3002	±19	3499	±37	3503	±30
Torque (Nm)	70.0	±0.6	100.0	±1.9	88.8	±14.8	100.0	±3.4	100.0	±3.1
Oil (°C)	108.7	±0.1	107.0	±0.3	115.2	±0.2	116.5	±0.4	117.4	±0.3
Coolant (°C)	87.0	±0.1	87.2	±0.1	87.2	±0.1	88.0	±0.2	88.0	±0.1